Doctoral Dissertation

Development of Conductive Composite Hydrogels Containing Chitosan for Flexible Sensors

フレキシブルセンサーにおけるキトサン含有導電性
複合ハイドロゲルの開発

DU PENG

July 2024

Graduate School of Engineering,

Osaka University

Contents

Page

General Introduction **1**
References 13

Chapter 1
Self-Adhesive and Strain-Sensitive Chitosan/Poly(acrylamide) Hydrogels Fabricated by Salt-Soaking Strategy **18**
1-1. Introduction 18
1-2. Experimental section 20
1-3. Results and Discussion 24
1-4. Conclusions 34
1-5. References 35

Chapter 2
Hydrophobic Association Hydrogel Containing Chitosan for Amphibious Applications **40**
2-1. Introduction 40
2-2. Experimental Section 43
2-3. Results and discussion 46
2-4. Conclusions 59
2-5. References 60

Chapter 3
Organohydrogel Incorporated with Quaternized Chitosan (QCS) and Ionic Liquid (IL)-Graphene Nanosheets for Flexible Sensing **66**
3-1. Introduction 66
3-2. Experimental Section 68
3-3. Results and discussion 74
3-4. Conclusions 83
3-5. References 83

Concluding remarks **88**

List of Publications **91**

Acknowledgments **92**

General Introduction

Advancements in hydrogel-based flexible sensors

Hydrogels are primarily composed of natural or synthetic polymer chains that are cross-linked through physical or chemical means, forming a three-dimensional (3D) network.[1, 2] This structure contains a large number of water molecules and is typically soft and elastic, making them suitable for wide-ranging applications across various fields.[3-6] Their liquid properties ensure the capability to dissolve drugs and disperse conductive media, while their solid-like properties enable the hydrogel to bear external forces and maintain integrity during practical applications.[7, 8] Through rational design of their polymer networks, multi-functional hydrogels can be constructed for drug delivery systems,[9] implantable devices,[10] soft actuators[11] and flexible electronics.[12]

Although the development of synthetic polymer-based hydrogels has been mature, the synthetic polymers are mostly petrochemical products, facing major development problems such as resource depletion and environmental pollution.[13] Most importantly, some synthetic polymer hydrogels lack biocompatibility and biodegradability.[14] Natural polymers may be well suited to address these issues, because they are low-cost, renewability, and have excellent biological properties.[15] In addition, the structural characteristics of natural polymers make them ideal materials for constructing high-performance hydrogels. The abundant hydrophilic functional group in the molecular chains is a prerequisite for building hydrogels.[16] Additionally, natural polymers are easily modified chemically due to the high reactivity of their functional groups, allowing the preparation of hydrogels with special functions.[17, 18] Overall, synthetic and natural polymer hydrogels have their own advantages. The current research trend is to comprehensively select both types of polymers to prepare hydrogel materials with versatile functions for various research purposes.[19]

By leveraging the mechanical strength and tunability of synthetic polymers alongside the biocompatibility and biodegradability of natural polymers, it is promising to develop advanced hydrogels tailored to specific flexible sensors[20]. By incorporating ions, conductive polymers, or nanomaterials into hydrogels, the hydrogel-based wearable devices can possess outstanding

electrical and mechanical properties.[21-24] As a result, these sensors can sensitively capture various physical signals, such as pressure, strain stretching, and temperature changes (**Figure 1**), thereby enabling the real-time monitoring of human motion and physiological parameters.[25-28]

Conductive composite hydrogel for flexible sensors

Conventional flexible sensors based on metals and semiconductors are brittle, rigid, and less ductile and cannot be seamlessly adhered to the skin surface.[29] Conductive composite hydrogels with appropriate adhesion properties and reliable mechanical performance can be fabricated as sustainable wearable sensors due to their high ductility and strain sensitivity.[30] As mentioned above, it is necessary to further construct a conductive molecular skeleton based on the polymer network to fabricate conductive composite hydrogels. According to the different compositions of the conductive networks in the gels, conductive hydrogels are currently divided into three main types: conductive polymer hydrogels,[31] ionic hydrogels,[32, 33] and carbon-based composite hydrogels.[34]

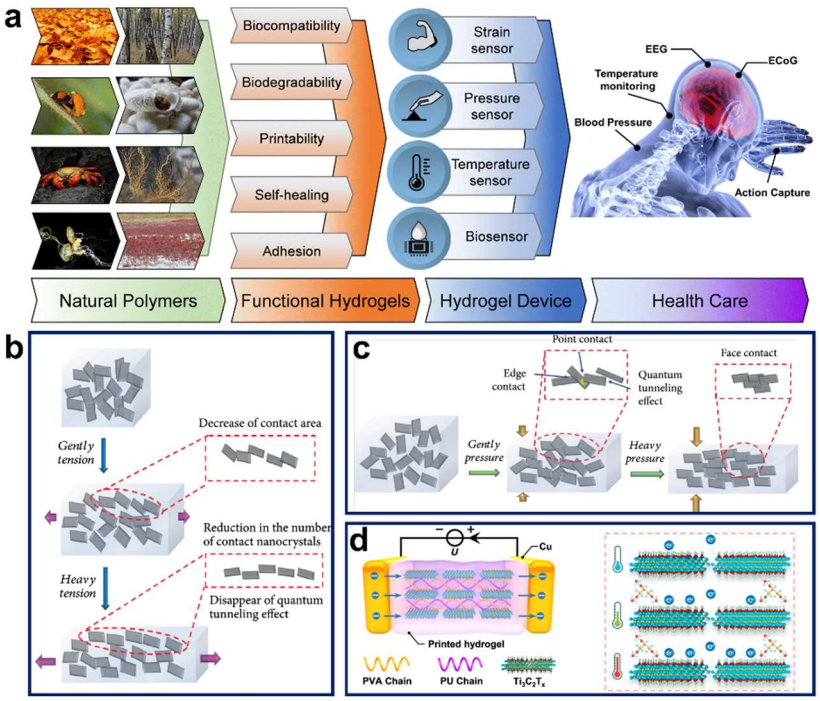

Figure 1. (a) Illustrated cue for emerging healthcare sensing systems from various natural polymers to functionalities, hydrogel devices, and healthcare applications.[26] (b, c) Schematic illustration of the electromechanical response mechanism of the hydrogel strain and pressure sensors.[27] (d) Schematic illustration of temperature sensing and its mechanism.[28]

Conductive polymer hydrogels

The synthesis and customization of conductive polymer hydrogels can be achieved through various methods, including in situ polymerization, blending, and chemical cross-linking.[35] These methods allow the electrical and mechanical properties of hydrogels to be fine-tuned to meet specific application requirements.

Conductive polymer hydrogels are typically formed by integrating conductive polymers such as polyaniline (PANI), polypyrrole (PPy), or poly(3,4-ethylenedioxythiophene) (PEDOT) into an insulating hydrogel matrix.[36] The conductive polymer network within these hydrogels allows for the efficient transport of electrical charges, making them suitable for a variety of applications including flexible electronics, biosensors, and biomedical devices.[37] For instance, Wang *et al*. used copolymer network of acrylamide and hydroxyethyl methacrylate (P(AAm-co-HEMA)) as a first flexible network, while the polyaniline (PANI) network as a second rigid conductive network through in-situ oxidative polymerization (**Figure 2**).[38] The mechanical properties and electrical sensing capabilities of the hydrogels were studied by regulating the polyaniline content in the gel. The optimal conductive hydrogel showed high strength, with a conductivity of 6.84 S m^{-1}, thus achieving timely recovery, high sensitivity and cyclic stability. Han *et al.* reported a transparent, conductive, stretchable, and self-adhesive hydrogel by in situ formation of polydopamine (PDA)-doped PPy nanofibers in polymer networks (**Figure 3**).[39] The catechol groups in PDA-PPy nanofibers not only give the hydrogels self-adhesiveness, but also make them tough and stretchable. Furthermore, the simple and smart strategy proposed to form conductive nanofibers in site opens new avenues for incorporating hydrophobic and insoluble conductive polymers into hydrogels. Despite their promising potential of these hydrogels, issues such as long-term stability and improved uniformity remain active research.

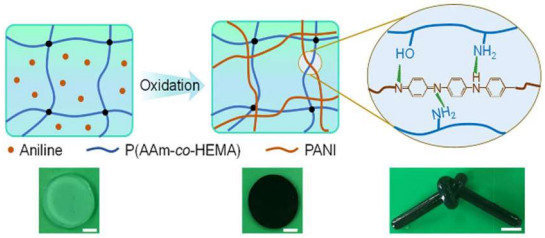

Figure 2. Schematic illustration of the synthesis of interpenetrating PANI/P(AAm-co-HEMA) hydrogels.[38]

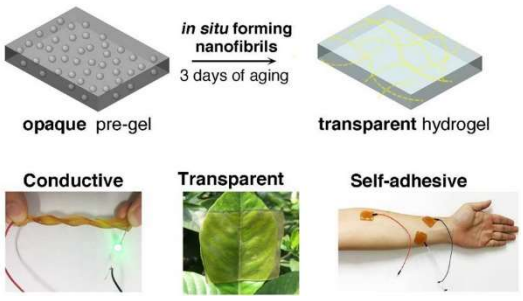

Figure 3. Scheme illustration of the hydrogel by in situ formation of PDA–PPy nanofibrils and its multifunctionalities.[39]

Preparing conductive hydrogels without insulating polymer networks is a direction. Pan *et al*. reported a scalable and versatile synthesis of a multifunctional polyaniline hydrogel with excellent electronic conductivity and electrochemical properties (**Figure 4**)[40]. Specifically, phytic acid was used as both a gelator and dopant to directly form the conductive networks without insulating polymers. Lu *et al*. proposed pure poly(3,4-ethylenedioxythiophene): polystyrene sulfonate (PEDOT:PSS) hydrogels with interconnected networks of PEDOT:PSS nanofibrils show extraordinary electrical, mechanical, and swelling properties without blending other compositions (**Figure 5**).[41] After controlled dry-annealing and rehydration, the resultant hydrogels exhibit extraordinary electrical (~20 S cm^{-1} in phosphate buffered saline (PBS), ~40 S cm^{-1} in deionized water), mechanical robustness, and tunable isotropic/anisotropic swelling properties without blending other compositions. Since these conductive polymers are often conjugated polymer chains, the resulting hydrogels may be brittle and lack the inherent flexibility of conventional hydrogels.

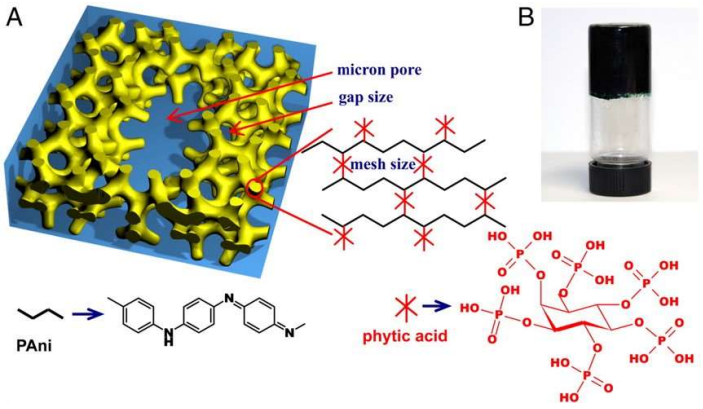

Figure 4. Schematic diagram of the cross-linking network of phytic acid cross-linked polyaniline hydrogel.[40]

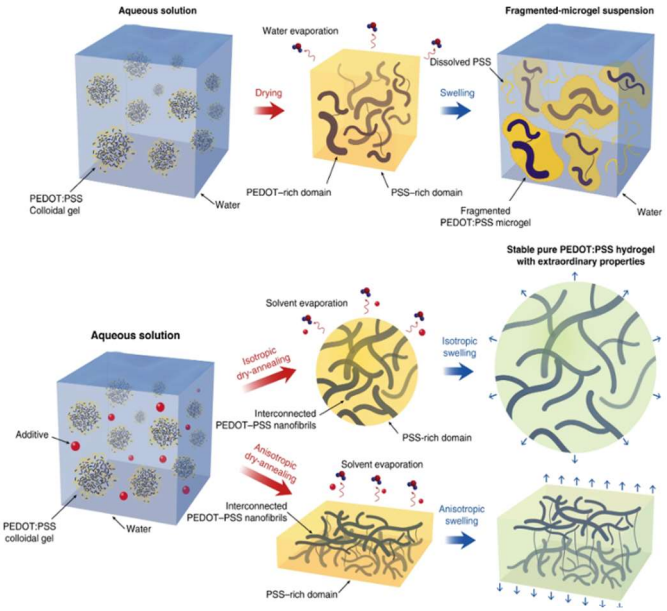

Figure 5. Schematic illustration of the preparation of pure PEDOT: PSS hydrogel.[41]

Ionic conductive hydrogels

Ion-conductive hydrogels have high water content and a nano- or micro-sized pore structure that allow mobile ions to freely transport charges within the network, thereby exhibiting ionic conductivity similar to that of electrical signals *in vivo*.[42] Moreover, the formation of transparent

hydrogels is possible with electrolytes (LiCl, NaCl, $CaCl_2$, *etc.*) dissolved in ion-conductive hydrogels without consideration of ion diffusion, showing a great potential in the field of visible and non-invasive bioelectronics.[43] Recently, Zhang *et al*. fabricated a wearable ionic temperature sensor based on ionically cross-linked polyacrylamide-sodium alginate hydrogel. By laminating the sensing hydrogel layer in which ions migrate in response to temperature with gold interdigitated electrodes, the wearable device can detect temperature differences in various parts of the body through the ion conduction mechanism.[44] Besides, ionic liquids (ILs) are ionic compounds composed entirely of anions and cations, which have the advantages of non-flammable and low toxicity, as well as show a wide electrochemical window and good thermal stability.[45] Therefore, they are not only used as dispersants for preparing ionogels, but also serve as conductive substances for obtaining ion-conductive hydrogels. For example, Yao *et al*. designed a multifunctional phenylboronic acid ionic liquid monomer and prepared an ion-conductive hydrogel with a semi-interpenetrating network structure through a one-step polymerization of PBA-IL/acrylamide in the presence of nanocellulose (CNF). As shown in **Figure 6**, the incorporation of imidazolium salt enhanced the ionic conductivity of the hydrogel, while CNFs improved its mechanical properties as a strain-enhancing phase, resulting in an ion-conductive hydrogel sensor with excellent comprehensive performance[46].

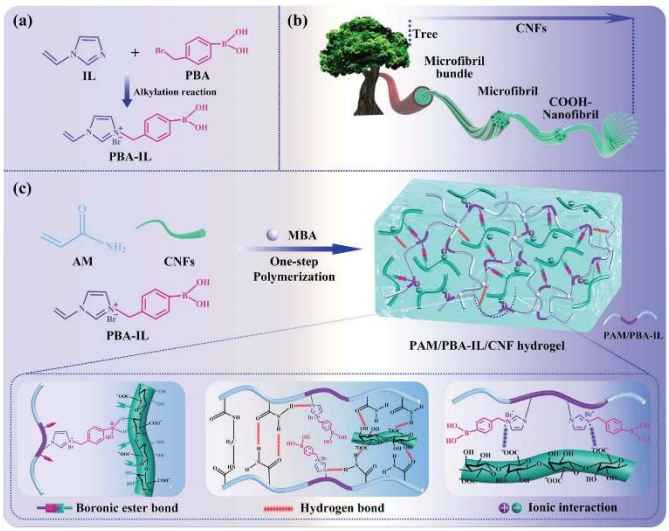

Figure 6. Synthetic route of the ionic liquid, fabrication and dynamic network interactions in the hydrogel.[46]

Carbon-based composite hydrogels

Carbon-based composite hydrogels are functional materials that incorporate carbon nanomaterials, such as graphene, graphene oxide (GO), carbon nanotubes (CNTs), MXene ($Ti_3C_2T_x$) or carbon nanofibers (CNFs), into a hydrogel matrix[47-50]. While traditional polymer hydrogels are flexible, they often lack sufficient stiffness, strength, and functionality. In contrast, carbon nanomaterials are strong and possess excellent electrical conductivity.[51] These

composite hydrogels combine the unique properties of carbon nanomaterials with the advantageous features of hydrogels, resulting in materials with enhanced electrical conductivity, mechanical strength, and multifunctionality. A simple method for preparing carbon-materials composite hydrogels is that uniformly dispersing carbon material nanoparticles or nanosheets in the gel precursors and then polymerizing to obtain a composite gel. However, the mechanical and electrical properties of the composite gel are related to the aspect ratio, specific surface area and dispersion of the carbon material in the polymer matrix. Therefore, Liu and co-authors synthesized a novel polyacrylamide (PAM) nanocomposite hydrogel with excellent ductility and repairability by an in-situ synthesis method without adding any chemical crosslinker.[52] They focused on the role of GO in the hydrogel and found that the uniformly dispersed GO nanosheets acted as a crosslinker and could effectively improve the mechanical properties of the nanocomposite hydrogel through hydrogen bonding, ionic bonding and physical adsorption in the organic/inorganic network structure (**Figure 7**). Besides, Liu *et al*. prepared a solvent-resistant graphene-assisted hydrogel through the combination of copolymerization of 2-methoxyethyl acrylate (MEA) and acrylic acid (AA) and solvent exchange.[53] The hydrogel was equipped with a multipurpose adhesion and nonswelling property in diverse solvents due to the nature of the synergistic hydrophobic and hydrophilic network structure. Moreover, the high contents of graphene effectively endowed the conductor with an excellent electromechanical response, but prominently contributed to robust mechanical performances.

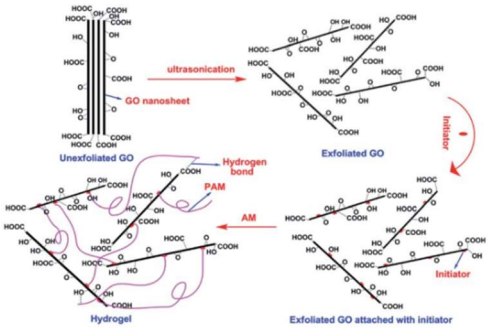

Figure 7. Synthesis method of the PAM/GO hydrogels.[52]

Another strategy for preparing carbon-materials composite hydrogels is that pre-synthesizing a carbon material scaffold such as aerogel and then infiltrating the gel prepolymer solution into the scaffold for further synthesis. However, the low compatibility between carbon materials and polymer networks can easily lead to phase separation and even weaken the mechanical properties of hydrogels. For example, Yan *et al*. described a facile approach for fabricating conductive and ultralight graphene aerogels using the natural drying technique and further fabricated conductive nanocomposites by introducing the copolymerization of 2-

methoxyethyl acrylate and *N*-isopropylacrylamide into the graphene aerogels networks (**Figure 8**) .[54] The resulting nanocomposite exhibited rapid self-healing properties at room temperature and high conductivity up to 70 S m^{-1}, which was promising for applications on flexible sensors and soft robotics.

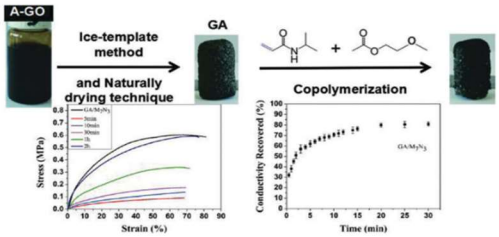

Figure 8. Fabrication process, mechanical performance and conductivity recovery of the conductive nanocomposite based on graphene aerogel.[54]

Chitosan-based conductive hydrogels

As an important research direction, natural polymer conductive hydrogels offer broad application prospects for flexible sensors by ensuring favorable biocompatibility, appropriate mechanical strength, and other comprehensive properties.[55, 56] As mentioned in the previous sections, achieving conductive properties in hydrogels are a critical challenge for extending their lifespan and increasing the variety of possible applications. Three strategies for preparing conductive hydrogels have been established. It is evident that the conductive polymer introduced to the hydrogel has certain hydrophilicity, which allows it to have good compatibility and reaction sites with nature polymer networks[57]. As reported by Marcasuzaa *et al*., chitosan-*graft*-PANI (chi-*g*-PANI) copolymers can be synthesized by simple oxidative method, and the products combined the good processability of the chitosan matrix and electrical conductivity of PANI, which showed better solvent solubility, processibility and mechanical properties.[58] Besides, the free ions introduced into the hydrogel not only enhance its conductivity but also provide other important functions. For instance, Zhang *et al*. prepared a double-network hydrogel by physical cross-linking and chemical cross-linking (**Figure 9**) .[59] The chemically created cross-linking network formed by polyacrylamide ensures the mechanical strength of the hydrogel, while the complexation of divalent calcium ions with the carboxyl groups in sodium alginate (SA) acts as a physical cross-linking network, ensuring the excellent recovery and high sensitivity of the

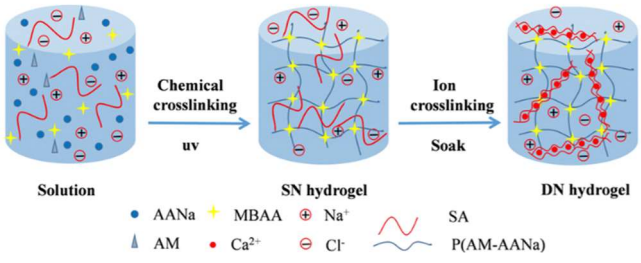

Figure 9. The preparation process of the double network (DN) hydrogel.[59]

hydrogel. Additionally, conductive nanomaterials have the characteristics of high rigidity, large specific surface area, and rich surface functional groups, thus they have the potential to interact with the natural polymers.[60] It has been reported that a high-content of CNTs can be efficiently and stably dispersed in cellulose nanofibers (CNFs) aqueous system.[61] Consequently, conductive composites for multifunctional sensors and wearable electronics can be directly constructed without additional structural materials.

Chitosan, the most representative biopolymer, has been widely studied in the field of natural polymer hydrogels. Chitosan is a random copolymer of D-glucosamine and N-acetylglucosamine, a natural polysaccharide derived from deacetylation of chitin. In addition, chitin is the second most abundant natural polymer after cellulose, and is widely found in the exoskeletons of crustaceans (such as shrimp and crabs), the shells of insects, and the cell walls of certain fungi[62-64]. Chitosan is biocompatible, biodegradable, and has excellent film-forming abilities, making it have unique advantages in the preparation and functionalization of hydrogels.[65] Therefore, chitosan-based conductive hydrogels can effectively combine chitosan with conductive components to enhance the electrical and mechanical properties of strain sensors based on relative resistance changes. Generally, the high conductivity and reliable mechanical properties are the two most important basic parameters, which are mainly affected by conductive mechanisms and designation of the polymer network.[66] Furthermore, chitosan exhibits good solubility in acidic solvents, which is extremely beneficial for its chemical or physical modification by other materials.[67] To enhance the conductive performance, chitosan can be used to control the formation of conductive polymer pathways in hydrogels. Gan *et al*. reported an interpenetrating network hydrogel with conductive, stretchable, and biocompatible properties, where chitosan was used as a template to induce the adsorption and in-situ oxidative polymerization of conductive polymer monomers in the hydrogel.[68] Besides, thanks to its rigid molecular chain properties and highly active protonated amino groups, chitosan is an ideal material for improving the strength of hydrogels by building a rigid

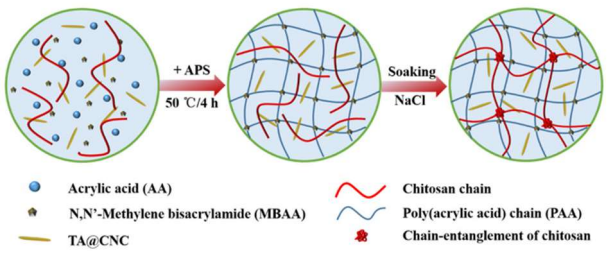

Figure 10. Preparation of the DN nanocomposite hydrogels by free radical polymerization and salt soaking induced chain entanglement.[69]

network. Cui *et al*. constructed chitosan/polyacrylic acid (PAA) double network nanocomposite hydrogel by salt solution immersion method (**Figure 10**).[69] The PAA chemical cross-linking network was first fabricated by free radical polymerization reaction, and then the electrostatic repulsion between chitosan molecular chains was shielded by immersion in saturated NaCl solution, resulting in chain entanglement and forming rigid physical cross-linking network. Furthermore, Jiang and co-authors proposed a multi-physical cross-linking strategy to prepare a hydrogel strain sensor based on chitosan quaternary ammonium salt modified AM-co-AA copolymer hydrogel (**Figure 11**).[70] The double network hydrogel was ionically cross-linked by immersion method, with Fe^{3+} as a cross-linking point, cross-linking with the amino group (–NH_2) on chitosan quaternary ammonium salt and the carboxyl group on P(AM-co-AA), so that the hydrogel-based strain sensor can effectively dissipate energy, thus obtaining excellent tensile stress (3 MPa), elongation (1390%), elastic modulus (0.42 MPa) and toughness (25 MJ m^{-3}). These reports indicate that chitosan, as the only polysaccharide with unique advantages in nature, has high research value for improving the mechanical strength and multifunctionalities of conductive hydrogels.

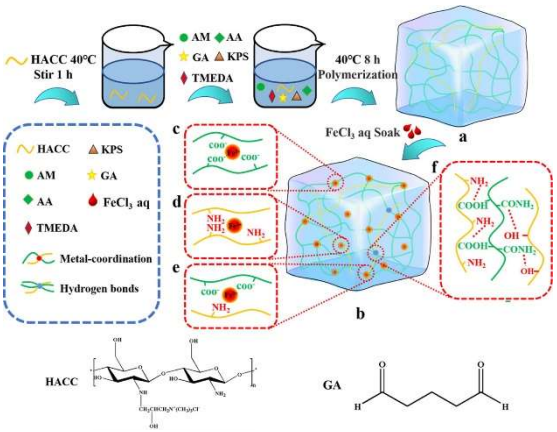

Figure 11. Schematic illustration of the preparation process and internal structural diagrams of the nanocomposite hydrogels.[70]

Overall, to construct conductive composite hydrogels containing chitosan for flexible sensors, clarifying the conductive mechanism, improving the mechanical performance, and expanding the application fields are highly required.

Network design of the hydrogels in this thesis

Hydrogels as functional materials have shown great potential in important application areas such as electrical sensors and tissue engineering.[71] However, under the premise of integrating the biocompatibility, degradability, and non-toxicity of chitosan, it remains a great challenge to simultaneously realize multiple functions in a single conductive hydrogel:[72-75] (i) high stretchability is not enough, and the hydrogels still need to exhibit excellent elasticity and self-recovery properties to ensure their long-term usability, (ii) it is essential that the hydrogel

maintains sufficiently low elastic modulus and self-adhesiveness to ensure compliance, (iii) outputting stable and accurate electromechanical signals from hydrogels sensors under complex scenarios is highly required.

In this thesis, a series of chitosan-containing conductive hydrogels based on different conductive skeletons, with favorable mechanical strength and electromechanical sensitivity, were fabricated through the elaborate regulation of the polymer network (**Figure 12**). In Chapter 1, the author proposed a hydrogel composed of a rigid matrices and flexible networks. In the first network, the hydrophobic and aggregated polyaniline was grafted into chitosan chain, while in the second network, quaternate-functionalized nucleobase moieties endowed the conductive hydrogels with self-adhesion. The resulting hydrogel with chi-*g*-PANI copolymers exhibited a promising conductivity and high elongation strength because of the conductivity of PANI and chain entanglement of chitosan after soaking process, respectively, showing potential applications in sign language transmission. In Chapter 2, a multiple dynamic-bond-driven hydrophobic association hydrogel with reliable water resistance, mechanical robustness, and stable electrical properties was proposed via a "two-step" method including micellar copolymerization and post-soaking strategy. Benefiting from the electrostatic interacted hydrophobic segments and chitosan chain entanglements, the transparent hydrogel exhibits desirable anti-swelling features, excellent stretchability, and toughness. Moreover, the as-prepared hydrogel for amphibious sensing possesses significant conductivity and storage durability owing to the electrostatic interactions, and strong hydrogen bonding established by sodium phytate (PANa). In Chapter 3, the author prepared a conductive organohydrogel based on carbon materials in the presence of dimethyl sulfoxide (DMSO)/H_2O binary solvent. The critically dispersed graphene nanosheets, which was attached by the ionic

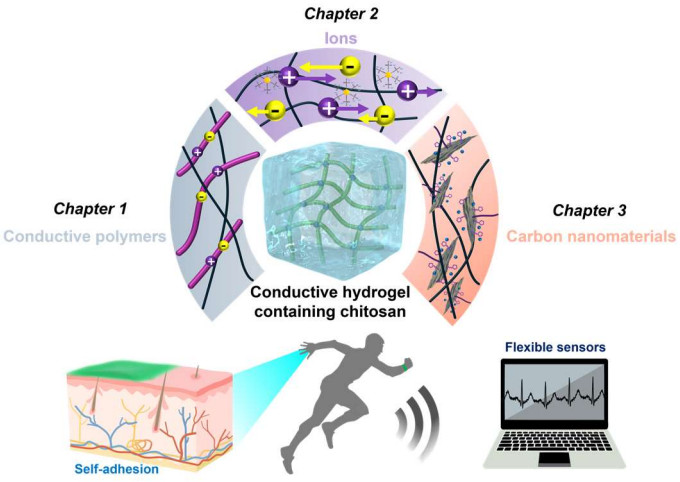

Figure 12. Overview of the network designation within the hydrogels in this thesis.

liquid (IL), can chemically integrate into swelling-resistant gel networks through ultrasonic-induced gelation. Owing to its high mechanical stretchability, reliable environmental tolerance, and satisfactory sensitivity, the fast prepared organohydrogel is fabricated into an all-climate wearable sensor for daily activity detection and temperature sensing.

Outlines of this thesis

In this doctoral thesis, the author provided new ideas for the design and manufacture of flexible electronic devices based on chitosan containing conductive hydrogels. These hydrogels with different conductive mechanisms were focused on and further explored, and the corresponding mechanical properties, electrical conductivity, self-adhesion, environment tolerance and strain sensing capability were systemically investigated. This thesis is expected to contribute to the development of a platform for designing hydrogels for smart soft materials and versatile bioelectronic devices.

Chapter 1

In Chapter 1, a homogeneous conductive hydrogel composed of functionalized adenine molecules and chi-*g*-PANI copolymers for sign language transmission was developed (**Figure 13**). The quaternate adenine not only acted as an adhesive factor for stable adhesion but also promoted the dispersion of the rigid polymer network. Additionally, the post-cross-linking rigid networks providing significant electrical and mechanical properties were homogeneously embedded in the matrix. Therefore, the as-assembled conductivity hydrogel sensor demonstrated a high toughness, skin-like modulus, high stretchability, significant sensitivity, and rapid response. Based on these, it was applied as a flexible sensor for human motion detection and sign language identification.

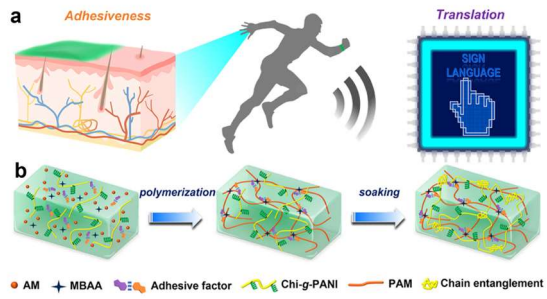

Figure 13. (a) Schematics illustrating the hydrogel sensor for self-adhesive interface and sign language transmission and (b) The two-step preparation process for the hydrogel.[76]

Chapter 2

In Chapter 2, an electrostatically interacting hydrophobic association (HA) hydrogel with

amphibious adhesion was successfully developed by a facile "two-step" method (**Figure 14**). In this strategy, random polymerization between hydrophilic monomers and hydrophobic monomers was cross-linked in the presence of cationic surfactant micelles, followed by the chain entanglement of chitosan in sodium phytate (PANa) solution soaking. Based on the synergistic effect of dynamic chain entanglement and strong hydrogen bonding, the homogeneous network hydrophobic hydrogel exhibited excellent anti-swelling, and desirable mechanical properties, demonstrating promising prospects for strain sensing in both air and aquatic conditions.

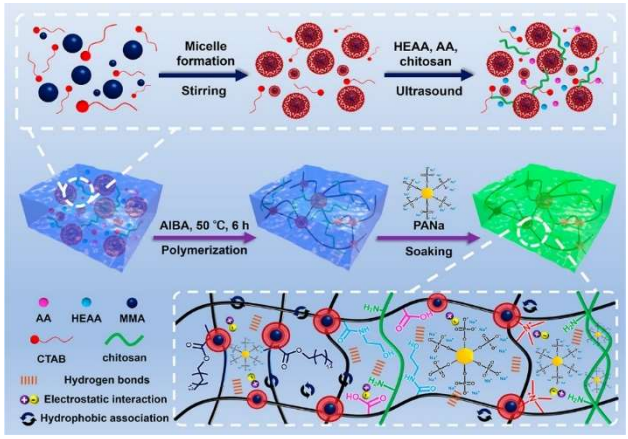

Figure 14. Mechanism illustration of constructing multiple physically interacted hydrophobic association hydrogels based on a "two-step" strategy.[77]

Chapter 3

In Chapter 3, the author designed an alkylation ionic liquid (IL), which was used to achieve polydisperse covalent-converted graphene through nucleophilic ring-opening reaction. The polymerizable ionic liquid-graphene oxide (IL-GO) was integrated into the ultrasonic-induced organohydrogel network rather than incorporated separately (**Figure 15**). Moreover, the rapidly

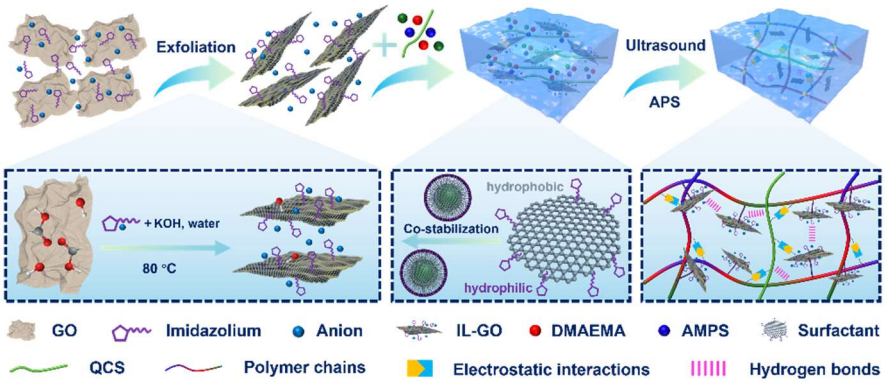

Figure 15. Schematic illustration of the preparation process and the corresponding interactions of the IL-GO and the organohydrogel.[78]

prepared organohydrogel exhibited favorable mechanical properties, self-adhesion, moisture retention, environmental tolerance and electrical conductivity, which enabled it applied as multimodal all-weather sensor for strain and temperature sensing in different extreme conditions.

References

1. Y. S. Zhang and A. Khademhosseini, *Science*, 2017, **356**, eaaf3627.
2. X. Li and J. P. Gong, *Nat. Rev. Mater.*, 2024, **9**, 380-398.
3. E. M. Ahmed, *J. Adv. Res.*, 2015, **6**, 105-121.
4. X. Du, J. Zhou, J. Shi and B. Xu, *Chem. Rev.*, 2015, **115**, 13165-13307.
5. S. Correa, A. K. Grosskopf, H. Lopez Hernandez, D. Chan, A. C. Yu, L. M. Stapleton and E. A. Appel, *Chem. Rev.*, 2021, **121**, 11385-11457.
6. G. Kougkolos, M. Golzio, L. Laudebat, Z. Valdez-Nava and E. Flahaut, *J. Mater. Chem. B*, 2023, **11**, 2036-2062.
7. Z. Li, J. Lu, T. Ji, Y. Xue, L. Zhao, K. Zhao, B. Jia, B. Wang, J. Wang, S. Zhang and Z. Jiang, *Adv. Mater.*, 2024, **36**, 2306350.
8. J. Chen, Q. Peng, X. Peng, H. Zhang and H. Zeng, *Chem. Rev.*, 2022, **122**, 14594-14678.
9. S. J. Buwalda, T. Vermonden and W. E. Hennink, *Biomacromolecules*, 2017, **18**, 316-330.
10. V. R. Feig, H. Tran, M. Lee and Z. Bao, *Nat. Commun.*, 2018, **9**, 2740.
11. Y. Lee, W. J. Song and J. Y. Sun, *Mater. Today Phys.*, 2020, **15**, 100258.
12. Y. Zhang, Y. Tan, J. Lao, H. Gao and J. Yu, *ACS Nano*, 2023, **17**, 9681-9693.
13. G. Hayes, M. Laurel, D. MacKinnon, T. Zhao, H. A. Houck and C. R. Becer, *Chem. Rev.*, 2023, **123**, 2609-2734.
14. D. Xia, J. Chen, Z. Zhang and M. Dong, *Aggregate*, 2022, **3**, e176.
15. Z. Bao, C. Xian, Q. Yuan, G. Liu and J. Wu, *Adv. Healthcare Mater.*, 2019, **8**, 1900670.
16. W. Feng and Z. Wang, *Adv. Sci.*, 2023, **10**, 2303326.
17. J. Yang, H. Wang, W. Huang, K. Peng, R. Shi, W. Tian, L. Lin, J. Yuan, W. Yao, X. Ma and Y. Chen, *Mater. Horiz.*, 2023, **10**, 3797-3806.
18. X. Sun, Y. Liang, L. Ye and H. Liang, *J. Mater. Chem. B*, 2021, **9**, 7751-7759.
19. K. Sahu and S. Chakma, *Polym. Bull.*, 2024, **81**, 7687-7711.
20. L. Lan, J. Ping, J. Xiong and Y. Ying, *Adv. Sci.*, 2022, **9**, 2200560.
21. S. J. Peñas-Núñez, D. Mecerreyes and M. Criado-Gonzalez, *ACS Appl. Bio Mater.*, 2024, DOI: 10.1021/acsabm.3c01224.

22. J. Song, Y. Zhang, S. Y. Chan, Z. Du, Y. Yan, T. Wang, P. Li and W. Huang, *npj Flexible Electron.*, 2021, **5**, 26.

23. Z. Chen, J. W. F. To, C. Wang, Z. Lu, N. Liu, A. Chortos, L. Pan, F. Wei, Y. Cui and Z. Bao, *Adv. Energy Mater.*, 2014, **4**, 1400207.

24. X. Li, Y. Guo, T. Gao, P. Li, Z. Jin and D. Xiao, *ACS Appl. Mater. Interfaces*, 2021, **13**, 57411-57421.

25. H. Souri, H. Banerjee, A. Jusufi, N. Radacsi, A. A. Stokes, I. Park, M. Sitti and M. Amjadi, *Adv. Intell. Syst.*, 2020, **2**, 2000039.

26. Z. Wang, H. Wei, Y. Huang, Y. Wei and J. Chen, *Chem. Soc. Rev.*, 2023, **52**, 2992-3034.

27. Y. Lu, X. Qu, W. Zhao, Y. Ren, W. Si, W. Wang, Q. Wang, W. Huang and X. Dong, *Research*, 2020, **2020**, 2038560.

28. H. Liu, C. Du, L. Liao, H. Zhang, H. Zhou, W. Zhou, T. Ren, Z. Sun, Y. Lu, Z. Nie, F. Xu, J. Zhu and W. Huang, *Nat. Commun.*, 2022, **13**, 3420.

29. W. Gao, J. Huang, J. He, R. Zhou, Z. Li, Z. Chen, Y. Zhang and C. Pan, *InfoMat*, 2023, **5**, e12426.

30. D. Liu, C. Huyan, Z. Wang, Z. Guo, X. Zhang, H. Torun, D. Mulvihill, B. B. Xu and F. Chen, *Mater. Horiz.*, 2023, **10**, 2800-2823.

31. T. Zhou, H. Yuk, F. Hu, J. Wu, F. Tian, H. Roh, Z. Shen, G. Gu, J. Xu, B. Lu and X. Zhao, *Nat. Mater.*, 2023, **22**, 895-902.

32. C. Wang, J. Zhang, C. Niu, Q. Fu and L. Lu, *Chem. Mater.*, 2023, **35**, 1991-2005.

33. R. Li, J. Ren, M. Zhang, M. Li, Y. Li and W. Yang, *Biomacromolecules*, 2024, **25**, 614-625.

34. T. Zhu, Y. Ni, G. M. Biesold, Y. Cheng, M. Ge, H. Li, J. Huang, Z. Lin and Y. Lai, *Chem. Soc. Rev.*, 2023, **52**, 473-509.

35. U. S. K. Madduma-Bandarage and S. V. Madihally, *J. Appl. Polym. Sci.*, 2021, **138**, 50376.

36. F. Fu, J. Wang, H. Zeng and J. Yu, *ACS Mater. Lett.*, 2020, **2**, 1287-1301.

37. J. Ma, J. Zhong, F. Sun, B. Liu, Z. Peng, J. Lian, X. Wu, L. Li, M. Hao and T. Zhang, *Chem. Eng. J.*, 2024, **481**, 148317.

38. Z. Wang, J. Chen, Y. Cong, H. Zhang, T. Xu, L. Nie and J. Fu, *Chem. Mater.*, 2018, **30**, 8062-8069.

39. L. Han, L. Yan, M. Wang, K. Wang, L. Fang, J. Zhou, J. Fang, F. Ren and X. Lu, *Chem. Mater.*, 2018, **30**, 5561-5572.

40. L. Pan, G. Yu, D. Zhai, H. R. Lee, W. Zhao, N. Liu, H. Wang, B. C. K. Tee, Y. Shi, Y. Cui and Z. Bao, *Proc. Natl. Acad. Sci. U.S.A.*, 2012, **109**, 9287-9292.

41. B. Lu, H. Yuk, S. Lin, N. Jian, K. Qu, J. Xu and X. Zhao, *Nat. Commun.*, 2019, **10**, 1043.

42. X. Yao, S. Zhang, N. Wei, L. Qian and S. Coseri, *Adv. Fiber Mater.*, 2024, DOI:10.1007/s42765-024-00418-4.

43. Z. Luo, W. Li, J. Yan and J. Sun, *Adv. Funct. Mater.*, 2022, **32**, 2203988.

44. J. Zhang, K. Yan, J. Huang, X. Sun, J. Li, Y. Cheng, Y. Sun, Y. Shi and L. Pan, *Adv. Funct. Mater.*, 2024, **34**, 2314433.

45. K. S. Egorova, E. G. Gordeev and V. P. Ananikov, *Chem. Rev.*, 2017, **117**, 7132-7189.

46. X. Yao, S. Zhang, L. Qian, N. Wei, V. Nica, S. Coseri and F. Han, *Adv. Funct. Mater.*, 2022, **32**, 2204565.

47. Q. Li, B. Tian, J. Liang and W. Wu, *Mater. Chem. Front.*, 2023, **7**, 2925-2957.

48. J. Anjali, V. K. Jose and J.-M. Lee, *J. Mater. Chem. A*, 2019, **7**, 15491-15518.

49. X. Zhao, X. Chen, H. Yuk, S. Lin, X. Liu and G. Parada, *Chem. Rev.*, 2021, **121**, 4309-4372.

50. Y.-Z. Zhang, J. K. El-Demellawi, Q. Jiang, G. Ge, H. Liang, K. Lee, X. Dong and H. N. Alshareef, *Chem. Soc. Rev.*, 2020, **49**, 7229-7251.

51. G. Hong, S. Diao, A. L. Antaris and H. Dai, *Chem. Rev.*, 2015, **115**, 10816-10906.

52. R. Liu, S. Liang, X.-Z. Tang, D. Yan, X. Li and Z.-Z. Yu, *J. Mater. Chem.*, 2012, **22**, 14160-14167.

53. X. Liu, Q. Zhang and G. Gao, *ACS Nano*, 2020, **14**, 13709-13717.

54. S. Yan, G. Zhang, X. Jin, H. Jiang, F. Li, L. Zhang, Z. Wang, L. Fan and H. Li, *J. Mater. Chem. C*, 2018, **6**, 10184-10191.

55. Z. Shi, X. Gao, M. W. Ullah, S. Li, Q. Wang and G. Yang, *Biomaterials*, 2016, **111**, 40-54.

56. C. Cui, Q. Fu, L. Meng, S. Hao, R. Dai and J. Yang, *ACS Appl. Bio Mater.*, 2021, **4**, 85-121.

57. J. Chong, C. Sung, K. S. Nam, T. Kang, H. Kim, H. Lee, H. Park, S. Park and J. Kang, *Nat. Commun.*, 2023, **14**, 2206.

58. P. Marcasuzaa, S. Reynaud, F. Ehrenfeld, A. Khoukh and J. Desbrieres, *Biomacromolecules*, 2010, **11**, 1684-1691.

59. X. Zhang, J. Zhang, W. Liao, D. Zhang, Y. Dai, C. Wu, J. Wen and W. Zeng, *J. Mater. Chem. C*, 2023, **11**, 15873-15880.

60. H. Yoon and J. Jang, *Adv. Funct. Mater.*, 2009, **19**, 1567-1576.

61. Y. Liu, S. Zhang, L. Li and N. Li, *Adv. Fiber Mater.*, 2024, **6**, 758-771.

62. M. N. V. R. Kumar, R. A. A. Muzzarelli, C. Muzzarelli, H. Sashiwa and A. J. Domb, *Chem. Rev.*, 2004, **104**, 6017-6084.

63. Z. Shariatinia and A. M. Jalali, *Int. J. Biol. Macromol.*, 2018, **115**, 194-220.

64. I. Postnova, V. Silant'ev, S. Sarin and Y. Shchipunov, *Chem. Rec.*, 2018, **18**, 1247-1260.

65. A. Rasool, M. Rizwan, A. Islam, H. Abdullah, S. S. Shafqat, M. K. Azeem, T. Rasheed and M. Bilal, *Starch - Stärke*, 2024, **76**, 2100150.

66. T. R. Ray, J. Choi, A. J. Bandodkar, S. Krishnan, P. Gutruf, L. Tian, R. Ghaffari and J. A. Rogers, *Chem. Rev.*, 2019, **119**, 5461-5533.

67. H. El Knidri, R. Belaabed, A. Addaou, A. Laajeb and A. Lahsini, *Int. J. Biol. Macromol.*, 2018, **120**, 1181-1189.

68. D. Gan, L. Han, M. Wang, W. Xing, T. Xu, H. Zhang, K. Wang, L. Fang and X. Lu, *ACS Appl. Mater. Interfaces*, 2018, **10**, 36218-36228.

69. C. Cui, C. Shao, L. Meng and J. Yang, *ACS Appl. Mater. Interfaces*, 2019, **11**, 39228-39237.

70. L. a. Jiang, S. Tian, Y. Xie, X. Lv and S. Sun, *Langmuir*, 2023, **39**, 8698-8709.

71. H. Cao, L. Duan, Y. Zhang, J. Cao and K. Zhang, *Signal Transduct. Target. Ther.*, 2021, **6**, 426.

72. H. Yao, M. Wu, L. Lin, Z. Wu, M. Bae, S. Park, S. Wang, W. Zhang, J. Gao, D. Wang and Y. Piao, *Mater. Today Bio*, 2022, **16**, 100429.

73. Y. Xu, M. Patino Gaillez, R. Rothe, S. Hauser, D. Voigt, J. Pietzsch and Y. Zhang, *Adv. Healthcare Mater.*, 2021, **10**, 2100012.

74. Q. Shi, H. Liu, D. Tang, Y. Li, X. Li and F. Xu, *NPG Asia Mater.*, 2019, **11**, 64.

75. X. Sun, S. Agate, K. S. Salem, L. Lucia and L. Pal, *ACS Appl. Bio Mater.*, 2021, **4**, 140-162.

76. P. Du, J. Wang, Y.-I. Hsu and H. Uyama, *ACS Appl. Mater. Interfaces*, 2023, **15**, 23711-23724.

77. P. Du, J. Wang, Y.-I. Hsu and H. Uyama, *Chem. Mater.*, 2024, **36**, 1318-1332.

78. P. Du, J. Wang, Y.-I. Hsu and H. Uyama, *ACS Mater. Lett.*, 2024, **6**, 2974-2984.

Chapter 1

Self-Adhesive and Strain-Sensitive Chitosan/Poly(acrylamide) Hydrogels Fabricated by Salt-Soaking Strategy

1-1. Introduction

Sign language as an effective form of communication that conveys information through visual-manual modality is extensively employed by people with auditory or speech impairments.[1, 2] However, nonprofessional signers with little prior knowledge of sign language may find it difficult to recognize and understand the messages conveyed by signers.[3, 4] Conductive hydrogel sensors developed as wearable translation devices can provide technical solutions owing to the unique physicochemical features that accurately perceive human physiological activities.[2, 5-7] Although the conductive hydrogels with metal particles,[8] carbon nanomaterials[9] and liquid metal[10] exhibit high sensitivity, they are subject to mismatches in the flexibility and compatibility of biosystems. To meet the stringent requirements of complicated mechanical and electrochemical properties, methods for developing hydrogels with conductive polymers are generally proposed.[11] As a widely used conducting polymer, polyaniline (PANI) with the advantages of wide conductivity range, good environmental characteristics, and chemical stability is attracting great attention.[12, 13] Moreover, thanks to its inexpensive raw materials and easy doping process, composite hydrogels with PANI become the ideal option for flexible sensing systems undoubtedly.[14] However, hydrogels that are directly mixed with PANI lack compatibility and stability because of the poor solubility in common solvents and hydrophobicity-hydrophilicity mismatch in hydrogel matrix.[12, 15] Despite the significant advances in research on PANI hydrogels, it is still a challenge to upgrade the processing simplicity and mechanical performance when combined with stiff conducting polymers.

Integrating the mechanical strength and processability of a second network polymer with the electrical conductivity of brittle PANI is therefore considered as an effective approach.[16] Chitosan, the product of *N*-deacetylated chitin, has amino group at the C_2 position that makes the polysaccharide have excellent biological functions and easily be chemical modified.[17, 18] Consequently, this natural macromolecule has been widely used in the development of hydrogel

sensors.[19] And the introduction of PANI into chitosan is expected to endow the material with mechanical properties and electrical conductivity.[16] The PANI can be grafted onto the chitosan backbone before hydrogel elaboration, so that the hydrogen bonding in chitosan/PANI enhanced the conducting properties and avoided the migration of the PANI outside of the gel.

Despite ongoing efforts, these composite hydrogel are still limited by their insufficient adhesion which hinder their practical applications as strain sensors.[20] The absence of self-adhesion leads to inaccurate detection of subtle deformations since the devices are inaccessible to dynamic and curved interfaces.[21] In the case of a sign language transmission system, these shortcomings can decrease sensitivity, distort translation, and even reduce user comfort. Therefore, the development of adhesive hydrogels based on molecular structure biomimetics is a key approach to addressing current limitations.[22] Recently, the research on self-adhesive hydrogels is mainly focusing on catechol and its derivatives.[23-25] Although the mussel-inspired adhesive hydrogels have been explored in convenient preparation methods with reference to simple principles, the catechol groups and analogs in the structure are easily oxidized into 1,2-benzoquinone with irreversible chemical bonds, causing weakened adhesion and limited reusability.[26, 27] Therefore, it is greatly valuable to pursue bio-inspired adhesive components originated from nature to realize reproducible adhesion for conductive hydrogels. Considering that purines are products in metabolic process and many purine derivatives such as adenine is the important nucleobase in deoxyribonucleic acid (DNA) and ribonucleic acid (RNA) composition. The heteromonocyclic structure of adenine forms multiple hydrogen bonding interactions which provides facile molecular recognition of groups on tissue surfaces. Currently, the reproducible adhesion ability inspired by adenine for gel materials are gaining great interest.[27-29] The hydrogels based on the principle of complementary base pairing were copolymerized with acrylated nucleobases and showed remarkable adhesive properties in different conditions. Although promising, the balance of mechanical properties and conductivity is affected due to the weak cohesion provided by hydrogen bonding in current report system. Therefore, it is highly expected to design conformal adhesive hydrogels with sustaining electrochemical and mechanical properties through modifying the adenine molecular.[30-33]

In this chapter, a bio-inspired strategy to prepare adhesive hydrogels driven by quaternized adenine was proposed. The hydrogel provided a Young's modulus and toughness[34] similar to that of skin, thus assuring no tightness while the self-adhesive hydrogel adhered to the human. Moreover, the co-polymerized adenine moieties in the polyacrylamide (PAM) matrix can also break the intra- and intermolecular hydrogen bonds of the chitosan-*graft*-PANI (chi-*g*-PANI) to enhance their dissolution. Meanwhile, the hydrogen bonding occurring between chitosan and PANI acquires good affinity between mechanically brittle network and the stretchable matrix. On the one hand, the dynamically crosslinked chitosan ingredients were used as second network to enhance biocompatibility and mechanical properties.[35] On the other hand, the homogeneously grafted PANI were exploited to endow the hydrogel with expected electrical conductivity. By fabricating the gel into a flexible strain sensor, it can monitor facial expressions and identify human motions stably. Thus, the author believe that the well-designed hydrogel is certainly of great importance to the field including: (i) sign language identification devices; (ii) signal transducer for information encryption and decryption according to Morse code.[36] Overall, the present work shows a high potential for use in biosensors, health monitoring, and athlete training analysis, paving the way for the development of next-generation strain sensors with an excellent processability and sensing properties.

1-2. Experimental section

Materials

Chitosan 100, adenine, aniline (ANI), potassium carbonate (K_2CO_3), acrylamide (AM), 2,2'-azobis(2-methylpropionamide) dihydrochloride (AIBA), trisodium citrate (Na_3Cit), *N*-methylpyrrolidone (NMP), dimethylformamide (DMF) and hydrochloric acid (HCl, 0.1M) were purchased from Fujifilm Wako Pure Chemical Corporation (Osaka, Japan). Solvent of deuterium dimethyl sulfoxide (DMSO-d_6) for nuclear magnetic resonance (NMR) spectroscopy was offered by Fujifilm Wako Pure Chemical Corporation (Osaka, Japan). *N*-[3-(dimethylamino)propyl] acrylamide was supplied by Tokyo Chemical Industry Co., Ltd. (Tokyo, Japan). Methanol, methylene-bis-acrylamide (MBAA) and ammonium persulfate (APS) was purchased from Nacalai Tesque, Inc. (Kyoto, Japan) and Sigma-Aldrich (St. Louis, USA), respectively. And all chemicals were used as received without further purification.

Preparation of chi-*g*-PANI

The procedure was based on previous works (**Figure 1-1**).[16] Specifically, a mixture of 0.22 g chitosan and 0.1 g ANI were introduced in 200 mL of 0.1 M HCl solution. The in-situ polymerization of ANI was initiated by 244.6 mg of APS. Later, NaOH was used to neutralize the copolymer that reacted for 4 h at room temperature. The resulting precipitate should be washed with excess of ethanol and NMP to remove free PANI. After doped with HCl, the grafted copolymer was dried at 30 ℃.

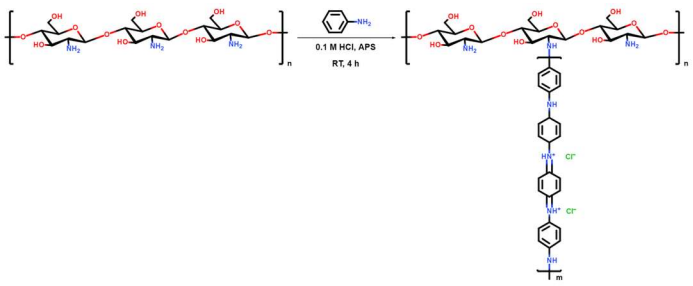

Figure 1-1. Preparation of the chi-*g*-PANI copolymer.

Preparation of adhesive groups

Firstly, the synthesis of 9-(2-bromoethyl) adenine (A-Br) from adenine and 1,2-dibromoethane was conducted according to the modified method[37] as shown in **Figure 1-2a**. Specially, 2.7 g of adenine, 16.35 g 1,2-dibromoethane, 100 mL of DMF, and 6.63 g of K_2CO_3 was mixed, and the reaction was then carried out at room temperature under N_2 protection for 48 h. The yellow solid A-Br was obtained by filtration and rotary evaporation. In **Figure 1-2b**, the procedure for synthesizing adhesive group (A-DMAPAM) was based on a previous reported work.[33] The DMF mixture containing A-Br (1.5 g) and *N,N*-dimethylpropylacrylamide (1.45 g) was stirred at 80 °C under N_2 atmosphere for 10 h. The crude products were dissolved in methanol after rotary evaporation. Subsequently, the A-DMAPAM was extracted by dissolution-precipitation and dried under vacuum.

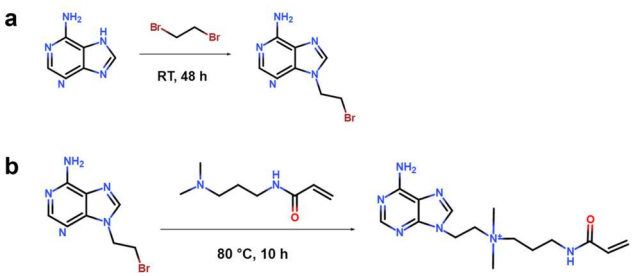

Figure 1-2. (a) Synthesis of A-Br and (b) Synthetic route of A-DMAPAM.

Synthesis of composite hydrogels

Prior to hydrogel preparation, 1, 3 and 5 g of chi-*g*-PANI was initially dissolved in 97 g of HCl solution to prepare suspensions (1, 3, and 5 wt%). Then, the composite hydrogels were

fabricated via two steps as shown in **Figure 1-3**.[38, 39] Typically, 5 g of chi-*g*-PANI suspension (3 wt%), 1.5 g of AM, 0.201 g of A-DMAPAM (3 mol% to AM), 5 mg of MBAA, and 6 mg of AIBA were mixed and homogeneously stirred, followed by degassing with ultrasonic cleaning for 10 min and storing in refrigerator for 30 min. After that, the mixture was poured into PTFE molds with depth of 1 cm at 50 °C for 12 h to achieve adhesive hydrogels with chi-*g*-PANI network. Next, the prepared gels were immersed into saturated Na_3Cit solution for 30 min to prepare the composite hydrogels with entanglement of chitosan (denoted as H-A-CP-3.0). The collected composite hydrogels were flushed by deionized water. To obtain the optimal concentration of rigid network in composite hydrogels without adhesion group, a similar method was utilized for control. As a representative example, composite hydrogels with 3 wt% of chi-*g*-PANI network (denoted as H-CP-3.0) were fabricated, where the free radical polymerization of AM monomer with certain amount of chi-*g*-PANI suspension, MBAA and AIBA were carried out at 50 °C for 12 h, followed by a soaking process.[40]

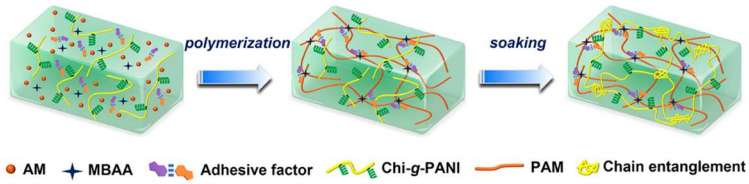

Figure 1-3. Schematic illustration of the two-step preparation process of the composite hydrogel.

Characterization

Attenuated total reflection Fourier transform infrared (ATR-FTIR) spectra over the wavenumber ranging from 4000 to 500 cm^{-1} was recorded at room temperature with a Nicolet iS5 spectrometer (Thermo Fisher Scientific). Products of synthesis were determined by ^1H NMR spectra with an equipment of JNM-ECS400 (400 MHz, JEOL). The powder X-ray diffraction (XRD) patterns were acquired using SmartLab (Rigaku Corporation) scanning speed of 5° min^{-1} at a 2θ range of 5–80°. The cross section of fractured freeze-dried hydrogels was captured by scanning electron microscopy (SEM, Hitachi SU3500) with an accelerating voltage of 15 kV.

Mechanical tests

The tensile properties of the hydrogel samples were tested using a universal material testing machine (Shimadzu EZ-Graph, Shimadzu Corporation) with a 100 N load cell. The samples

were cut into dumbbell-shaped samples with 1 mm thickness, 2 mm inner width and 10 mm gauge length and the stretching rate of was set 100 mm min^{-1}. The tensile strain (ε) was defined as the change in the length (l) relative to the gauge length(l_0) of the specimen. The tensile stress σ was determined by the ratio between load force (F) and the cross-sectional area (S). The elastic modulus (E) was calculated from the slope at the initial linear region in the range 5–15% of the stress.[41, 42]

The hydrogels were placed at the bottom of the parallel plates to investigate their viscoelastic behaviors of by the HAAKE RheoStress 6000 (Thermo Fisher Scientific). The oscillation frequency sweep in the linear viscoelastic region was conducted from 0.1 to 10 Hz at 0.1% strain under 25 °C.[43]

Adhesion test

The Shimadzu EZ-Graph universal testing machine equipped with 10 N load cell and 30 mm/min stretching rate was carried out to measure the adhesion performance on various substrates including polypropylene (PP), glass, silicone rubber, aluminum, wood and porcine skin. The specimen with a bonded area of 10 mm × 10 mm was sandwiched between two same materials surfaces attached to the plates. And the maximum load divided by the initial adhesion area was the adhesion strength.[44, 45]

Conductivity measurement

The electrical conductivity of the composite hydrogel (size: 20 mm × 10 mm × 2 mm) was obtained by recording the resistance signals in the frequency range of 0.1–10^6 Hz and voltage of 1V using an inductance, capacitance and resistance (LCR) meter (TH2830, Changzhou Tonghui Electronic Co. Ltd.). The conductivity calculation formula is as followed:

$$\sigma = \frac{L}{RS} \tag{1-1}$$

where L is the length between adjacent electrodes, R and S stands for the resistance and cross section area of the hydrogels, respectively.[46]

Electrical assessment

The relative resistance under different strain of the hydrogel was measured by the LCR meter combined with a servo motor (CL-01A, HaiJie-Tech) in real time. Moreover, the hydrogel sensor was controlled at a size of 20 mm × 10 mm × 2 mm, and the relative resistance change was computed as follows:

$$\frac{\Delta R}{R_0} = \frac{R - R_0}{R_0} \times 100\% \tag{1-2}$$

where R_0 and R represent the initial resistance and the resistance after deformation, respectively. The gauge factor (GF) is defined by the following equation:

$$\mathrm{GF} = \frac{|R - R_0|}{R_0 \varepsilon} \tag{1-3}$$

where ε denotes the corresponding strain change. In addition, the composite hydrogel was attached to human body to realize sign language transmission and information encryption via recording the resistance change at each physiological site[47].

1-3. Results and Discussion

Design and preparation of the composite hydrogels

The author developed a DNA-inspired adhesive factor to accomplish the balance of homogeneity and adhesion in hydrogels. To ensure the bonding groups, chemical structure of A-DMAPAM was characterized by ATR-FTIR spectrometry (**Figure 1-4a**). The carbonyl stretching in CH_2=CH–COOH showed up at about 1650 cm^{-1}. It means that the C=O absorption is shifted to the lower wavenumber due to the formation of hydrogen bonds and conjugation with aromatic rings.[29] Moreover, the structure formula and

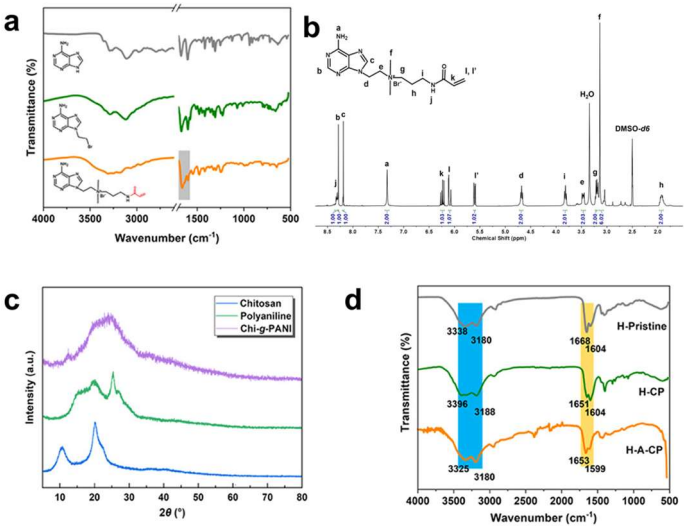

Figure 1-4. (a) FTIR spectra of adenine, A-Br and A-DMAPAM monomers. (b) ^{1}H NMR (400 MHz) spectrum of A-DMAPAM. (c) XRD patterns of the chitosan, polyaniline and chi-*g*-PANI. (d) FTIR spectra of the pristine hydrogel and composite hydrogels without (H-CP) and with adhesive factor (H-A-CP).

corresponding ^{1}H NMR spectra were shown in **Figure 1-4b**. The characteristic signals appearing at 5.55–6.27 and 8.15–8.20 ppm for A-DMAPAM were attributed to the acryl group and the aromatic ring, respectively.[33] This result was consistent with the structure in ATR-FTIR, indicating the successful reaction for adhesive factor. On the other hand, the XRD pattern was utilized to determine the composition and crystalline structure of chi-*g*-PANI. As shown in **Figure 1-4c**, chitosan has two different crystal forms, both of which belong to the monoclinic crystal system. The diffraction peaks appeared near 10° and 20°, which indicated that the amino group in chitosan was partially acetylated.[48] PANI showed significant and sharp diffraction peaks at 20° and 26°, indicating that the acid-doped polyaniline was oriented orderly and had a greater increase in crystallinity.[49] For the chi-*g*-PANI, there were broad diffraction peaks presented in 20°–30°, which was attributed to the scattering of molecular chains. The quaternary ammonium-like structure formed owing to the anion from protonation of a portion of N atom and cation from HCl, which strengthened the intermolecular chain forces.[50] Compared with pristine chitosan, the intensity of the peak at about 2θ=10° decreased and the peak position shifted, which demonstrated the decline in acetylation degree. Obviously, the solubility of chi-*g*-PANI was increased. Furthermore, in the ATR-FTIR spectroscopy (**Figure 1-4d**) of H-CP hydrogel, the non-hydrogen bonded N–H stretching and hydrogen bonded N–H stretch shifted at about 3396 cm^{-1} and 3188 cm^{-1}, and the peak ratios between the two N–H groups increased. It confirmed there existed hydrogen bonds between chi-*g*-PANI and the internal network of hydrogel.[51] For the H-A-CP hydrogel, the peaks shifted back slightly due to N–H vibration belonged to the functionalized adenine. However, more hydrogen bonding was discovered via observation on continuous improvement of the peak ratios. Similar changes were shown by non-hydrogen bonded (1653 cm^{-1}) and hydrogen bonded (1599 cm^{-1}) C=O vibration in hydrogels with A-DMAPAM. Notably, the peak ratios and presenting wavelength both changed, which might be attributed to the conjugation of aromatic ring and hydrogen bonds. These effects implied that the quaternized adenine enhanced the homogeneous dispersion of chi-*g*-PANI in hydrophilic network.

Mechanical properties of the H-CP hydrogels

The presence of chi-*g*-PANI is crucial to improving conductivity and mechanical performance of the hydrogels due to introduction of dual-functional components.[52] In **Figure 1-5a**, the typical stress-strain curves of H-CP hydrogels soaking in Na_3Cit solution were measured. With the increase of chi-*g*-PANI concentration, the fracture stress of the composite hydrogels increased while the tensile strain decreased. Notably, the H-CP hydrogel exhibited the optimal tensile properties when the chi-*g*-PANI content was 3.0 wt%, with a break strain of 1190% and strength of 1.12 MPa, and both values were close to the maximum compared to other concentration. Additionally, as shown in Figure **1-5b**, the elastic modulus of the H-CP-3.0 hydrogel was about 0.16 MPa, which was comparable as that of human skin (25–220 kPa). This specimen achieved the toughness of 7.59 MJ m^{-3}, and the value was as high as that of H-CP-5.0. This significant mechanical performance was possibly attributed to the fact that the massive amino groups hydrogen bonded with the amide groups on PAM chains. It was speculated that the chi-*g*-PANI and PAM network comprised interpenetration after immersion to enhance the elasticity and the entanglements of chi-*g*-PANI chains improved the toughness.[53] **Figure 1-5c** and **1-5d** displayed the significant toughness and ductility, the H-CP-3.0 was able to withstand 1 kg weight and could be stretched into film and recovered immediately.

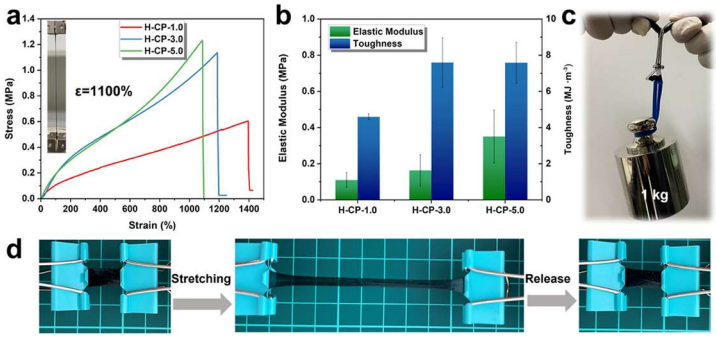

Figure 1-5. (a) Tensile stress−strain curves of hydrogels with different addition of chi-g-PANI. (b) Corresponding elastic modulus and toughness of the hydrogels in (a). (c) Images demonstrating that the H-CP-3.0 hydrogel could withstand 1 kg weight. (d) Photographs showing the stretching and recovering process of the H-CP-3.0 hydrogel.

Microstructure of the H-CP hydrogels

In terms of the microstructure, the freeze-fractured cross-section of the H-CP hydrogels with different addition amount of chi-g-PANI all exhibited porous morphologies (**Figure 1-6**). However, the degree of looseness and the dispersion condition were distinct. It

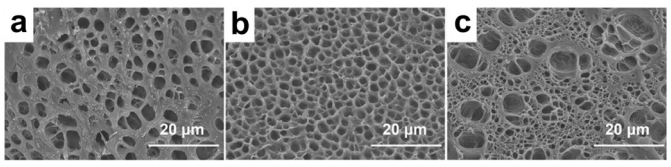

Figure 1-6. The SEM images of freeze-fractured cross-section of the (a) 1 wt%, (b) 3 wt% and (c) 5 wt% of chi-g-PANI in H-CP hydrogels.

was prone to suffer mechanical damage when stretched for H-CP-1.0 due to its huge pore size. Although the network containing excessive chi-*g*-PANI possessed considerable dense structure, the rigid network had an inhomogeneous distribution. The H-CP-3.0 formed a continuous network with small pore size which was potentially beneficial for the mechanical properties and conductivity of the hydrogel.[40]

Electrical conductivity of the H-CP hydrogels

The conductivity behavior is of vital important for electronic devices. **Figure 1-7** showed the one of the highest conductivities (4.8 $S \cdot m^{-1}$) of H-CP-3.0, which was significantly improved due to the appropriate amount of conductive polymer. The hydrogel with chitosan (H-CS) still lacked electrical conductivity even though soaked with free ions. Polyaniline was added based on it (same content as H-CP-3.0), yet probably the poor dispersion of polyaniline, the conductivity (H-CS/PANI) was only 3.8 $S \cdot m^{-1}$. From these results, the hydrogel with 3% addition of chi-*g*-PANI was utilized to further explore the adhesion performance.

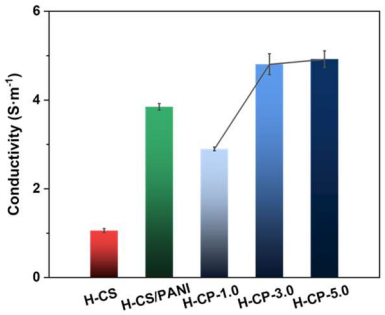

Figure 1-7. The conductivity of chitosan hydrogel, PANI blending hydrogel and composite hydrogels with addition of chi-*g*-PANI.

Mechanical properties and elasticity of the H-A-CP hydrogels

In general, extraordinary softness and ductility are key factors for hydrogel sensors to mimic the sensory performance of human skin. Therefore, it was necessary to specifically analyze the mechanical properties of the adhesive hydrogel. Related tensile tests were performed on the hydrogels with different addition of A-DMAPAM in **Figure 1-8a**. It was obvious that the increasing adhesive factor content weakened the tensile strength but raised the elongation at break of the hydrogels. The main reason was that functionalized adenine interacted with the polymer networks through weak hydrogen bonds. The A-DMAPAM acted as lubricant in the hydrogel network, increasing the movement space for interpenetrating networks during the stretching process. However, excessive adhesion factors in gels (H-A-CP-4 and H-A-CP-5) would inhibit the cohesion of network, resulting in poor elasticity and strength like liquid. The Young's modulus of the H-A-CP-3 hydrogels decreased to 184 kPa (**Figure 1-8b**), which was

equivalent to that of the human skin (25–220 kPa).[54] Moreover, the author discussed the oscillatory rheological behavior of hydrogels as an indicator of their viscoelastic properties. **Figure 1-8c** exhibited that the *G′* (storage moduli) of all the hydrogels was greater than the *G″* (loss moduli) in 0.1 Hz–10 Hz frequency sweeping range,

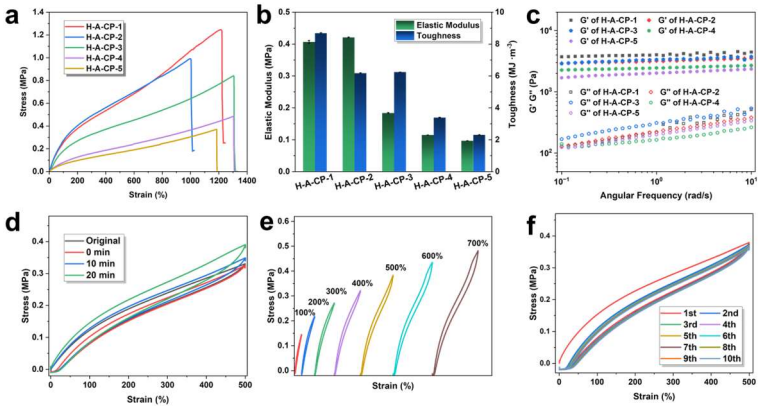

Figure 1-8. (a) Stress-strain curve of the adhesive hydrogels with different amounts of adhesive factors. (b) The corresponding toughness and elastic moduli. (c) Frequency-dependent storage modulus *G′* and loss modulus *G″* at a strain of 0.1%. (d) Loading-unloading curves at 500% strain after different resting times. (e) Successive cyclic tensile curves under the strain from 100 to 700%. (f) Successive loading-unloading stress-strain curves under 500% strain for 10 cycles.

indicating solid-like viscoelasticity behavior of the composite hydrogels.[53] Influenced by the π–π stacking of excess adenine groups, *G′* of the hydrogels declined dramatically as the content of A-DMAPAM exceeded 3 mol%. However, *G″* of H-A-CP-3 remained the highest, which reflected the viscous property in solid materials.[33]

Besides, cyclic tensile experiment was applied to investigate the self-recovery and antifatigue performance of H-A-CP-3 samples. In **Figure 1-8d**, the hysteresis loop at the initial loading-unloading cycle under the strain of 500% indicated the breakage of hydrogen bonds in the networks. But the tensile strength of the hydrogel was slight increasing after 10 min and 20 min of rest compared to the stable value in immediate test. It can be assumed that the entanglement of assisted by Na_3Cit was enhanced in the periodic deformation process.[55] Moreover, the electrostatic interactions and recombination of hydrogen bonds after resting implied the promising self-recovery ability of the gel at room temperature. Apart from the recoverability, the hydrogel showed robust elasticity during a cyclic stretching test at 100–700% strains in **Figure 1-8e**. The low hysteresis of each cycle can be attributed to the reconstruction of hydrogen bonds network. In addition, to further evaluate the fatigue resistance behavior, a loading-unloading test at 500% strain for 10 consecutive cycles was determined. As demonstrated in **Figure 1-8f**, the hysteresis loops except for the first stretching became narrow and kept almost steady. Therefore, the resultant H-A-CP-3 hydrogel was an ideal choice for

skin-like sensor in the following studies owing to its high stretchability, mechanical stability, low hysteresis and antifatigue properties.

Adhesion performance of the H-A-CP hydrogels

The adhesion capacity of H-A-CP-3 was evaluated after ensured the hydrogel with best ratio. It could be seen from **Figure 1-9a**, the hydrogel presented excellent adhesive properties for a variety of materials, including plastic, PTFE, glass, rubber, silicone, metal, wood, paper and biomaterials *etc.* Importantly, the hydrogel could bend and self-adhere, inferring its excellent mucoadhesive characteristics. Moreover, the hydrogel was freely adhered to the fingers without limiting the muscle deformation and could hold the recoverable strain, as shown in **Figure 1-9b**. The adhesion strength was quantitatively measured by lap shear test (**Figure 1-9c**). The correlation curves of adhesion strength versus displacement for hydrogel towards the glass, aluminum, plastic, silicone rubber, wood and porcine skin were shown in **Figure 1-9d**. The results illustrated that the maximum adhesion strengths in the interface of glass, aluminum, plastic, silicone rubber, wood and porcine skin reached 11.6, 17.4, 9.1, 10.8, 17.8 and 15.1 kPa, respectively. The hydrophilic surface of the wood was easily wetted by the hydrogel and bound by hydrogen bonding tightly; at the same time, the rough surface created a large frictional force, which gave it the highest adhesion strength compared to plastic and glass etc. The adhesive force on aluminum surface was as relatively high because of the metal complexion effect and hydrogen bond. In addition, the ability to repeat the adhesion in practice was very important since a brief peeling between the hydrogel and the substrate was inevitable. So that we could verify this by using porcine skin to simulate human skin. As depicted in **Figure**

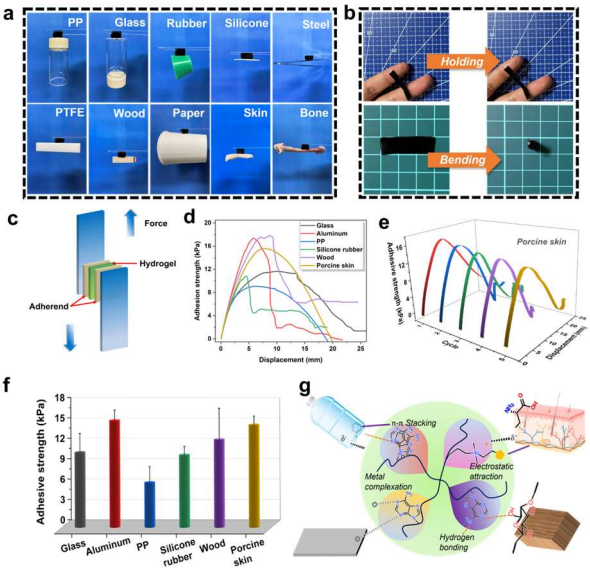

Figure 1-9. (a) Optical images of the adhesion ability to different substrates. (b) Photographs demonstrating the adhesiveness of the hydrogel under free stretching and bending. (c) Schematic diagram of the lap shear tests. (d) Adhesion strength-displacement curves for hydrogel on different substrates. (e) Successive adherence and separation cycles on porcine skin. (f) Adhesion strength of composite hydrogels on different substances. (g) Schematic adhesion mechanism of the hydrogel.

1-9e, the adhesion strength of the hydrogel to porcine skin decreased slightly from 16.2 to 13.7 kPa after 5 times of consecutive peeling-adhesion, which indicated that the hydrogel had good repeatable adhesive properties and can be used repetitively. Then, the adhesion strength on each substrate showed a similar trend and remained same basically (**Figure 1-9f**), that greatly improved the utilization of the hydrogel in application field. In principle, the adhesion behavior to different substrates might originate from the interaction between hydrogel and substrate, as shown in **Figure 1-9g**. Except for the high-density hydrogen bonds between adenine and hydrophilic substrates, the metal complexion and π–π stacking also contributed universal adhesion. Hydrophobic substrates with electrostatic charge interacted with the zwitterionic monomer through ion-dipole and dipole-dipole interactions, and the effect also presented on other substrates with polar groups, such as carboxyl groups on skin, amino groups on peptide chains, and hydroxyl groups on woods.[56, 57]

Application of the H-A-CP hydrogels as strain sensor

Excellent electrical conductivity was the requisite for sign language encryption and transmission device. The variable resistance was caused by changing length of electron transport channels, thus this phenomena implied the excellent strain sensitivity of hydrogel.[58] Next, in order to measure the changing rate of resistance versus strain of H-A-CP-3 hydrogel accurately, a tensile test with maximum strain set to 500% on the hydrogel was performed through combined usage of LCR meter. As depicted in **Figure 1-10a**, the hydrogel was used as a strain sensor material, and it showed a suitable sensitivity factor. In the tensile strain range of 0%–90%, the changing rate of the resistance ($\Delta R/R_0$) showed a linear increase, and the strain sensitivity calculated from its linear fitting function was GF=1.47. Moreover, as the strain increased from 40% to 500%, the GF value was also

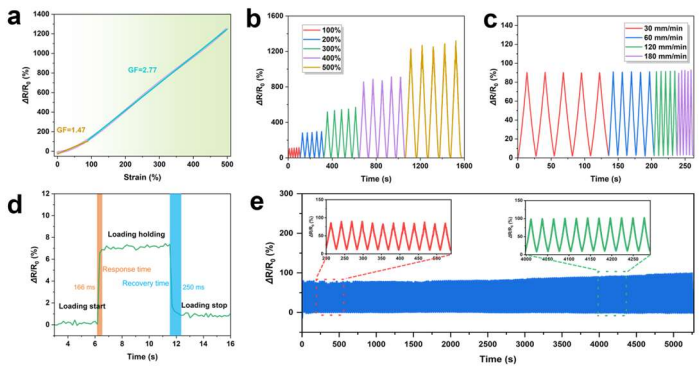

Figure 1-10. (a) Sensitivity of H-A-CP-3 hydrogel. (b) Periodic resistance response for 5 cycles under tensile strain from 100% to 500%. (c) The resistive change of the hydrogel sensor along with the stretching frequency for 5 cycles. (d) Response and recovery time of the hydrogel sensor. (e) Durability test of resistance change for the hydrogel sensor under 50% strain within 200 cycles.

measured up to 2.77 with a fitting goodness of 0.998. In summary, the hydrogel exhibited excellent sensitivity throughout the whole stretching process, indicating that the hydrogel could be used as a flexible strain sensor for both fine amplitude motion and macroscopic deformation sensing.

The sensing merit of the hydrogel under different strain was verified via resistance-strain variation curves. The author also recorded the resistance changes applying consecutive stretching−releasing cycles with fixed strains of 100%, 200%, 300%, 400% and 500% (**Figure 1-10b**). The signals of relative resistance exhibited smoothness, that indicated the excellent sensitivity of the hydrogel over a wide detection range. Based on the results, the strain sensor reflected strain dependency, which shown potential reliability in sign language transmission and health monitoring applications. To further confirm the repetitive, relative resistance variations at 50% strain using different frequencies were investigated. When the stretching speed of the hydrogel was increased from 30 mm min^{-1} to 180 mm min^{-1}, the peak variations of the relative resistance were almost the same. It demonstrated that the resistance changes of the hydrogel strain sensor remained stable and was not affected by the stretching rate, further indicated significant signal stability. Fast response capability for hydrogel sensors also played an important role in sign language recognition and conversion.[59] The author found that the H-A-CP-3 hydrogel sensor showed negligible electrical hysteresis during the tensile cycle (**Figure 1-10c**). The response speed for signals was able to satisfy the demands for real-time monitoring, with a response time of 166 ms and a recovery time of 250 ms (**Figure 1-10d**). Besides, 200 cycles of continuous stretching at 50% strain were conducted to evaluate the long-term stability in **Figure 1-10e**. The relative resistance was almost a constant, implying that the hydrogel possessed prominent fatigue resistance. Notably, slight drifting occurred in the relative resistance changes curve, especially after 120 times continuous stretching. It could be possibly attributed to the water loss from the hydrogel during a long duration of tensile stretching. Plus, during the long-time tensile process, polymer chains were so fatigued that network did not have enough time to recover, hence prevented the electrons moving rapidly and caused a high resistance.[60, 61] The stability, repeatability, sensitivity and broad sensing scale motivated the hydrogel sensor to display enormous potential for sign-to-speech flexible devices.

Human motion detection using the hydrogel sensor

Facial expression, body language, and visual-spatial position are all important components of sign language[62], so it is rewarding to detect human motion and emotion. In **Figure 1-11a**, the bending movements of head, face, neck, finger, wrist and knee were observed by connecting LCR meter to the hydrogel sensor. Amazingly, the hydrogel sensors were able to detect subtle movements of the body promptly and accurately, such as the tiny muscle movements from **Figure 1-11b–d**. The relative resistance curve showed a similar overall trend with slight difference when volunteer had different frown amplitudes, demonstrating the high sensing assessment according to gentle muscle action. The electrical signal changed by 6%, 28% and 9% for smiling, bulging and gaping when the volunteer repeated every movement five times. There were similar characteristic peaks for each action while noticeable differences from each other. When it was connected to volunteer's larynx, the result also confirmed the repeated deformations could be distinguished and monitored. It is well known that the sign language uses facial expressions and main-joint movements to convey meaning. To evaluate the feasibility under strenuous exercise, the electrical response of nodding was recorded in **Figure 1-11e**. The relative resistance change of the hydrogel sensor was almost constant (55%) and had good repeatability, indicating that it had high strain sensitivity and stability, and could monitor easy emotions in real time. Since it was a sign language interpretation device, we focused on monitoring the electrical response of the hand gestures. As revealed in **Figure 1-11f**, the volunteer's finger was bent, the relative resistance changes of the hydrogel sensor increased rapidly to the corresponding value, but the value varied with the bending angles. Further, the

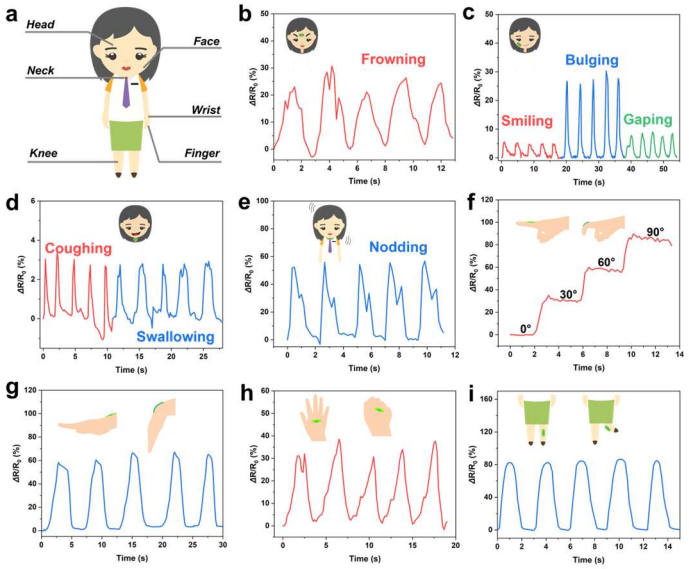

Figure 1-11. Relevant human motion monitoring by the flexible strain sensor. (a) Diagram of the detection parts of human body. The sensing of subtle actions: (b) frown, (c) smile, bulging and gaping, and (d) coughing and swallowing. Sensing performance in monitoring human joint movements: (e) nodding (e), (f) finger bending at 30°, 60°, 90°, (g) wrist bending, (h) electrical response of hand back by fisting, and (i) knee straight and bending.

sensor could detect the amplitude of the other hand joints movement and the speed of actions in a simple way (**Figure 1-11g** and **h**). The accurate description for hands movements implied that the hydrogel sensor could satisfy the demand for sign-to-speech transmission.[63] Similarly, the relative resistance changed at the same way when it was attached to volunteer's knee (**Figure 1-11i**), where the characteristics indicated that the hydrogel sensor also monitored various large limb movements in real time.

Information encryption and sign language interpretation

Encouraged by the high sensitivity, long-term stability and large working range of hydrogel sensors, the potential application could be expanded to the fields of information encryption and interpreting sign language (**Figure 1-12a**). Morse code is an "on and off" signal code that expresses different letters, numbers and punctuation characters by arranging them in different order.[64] Specifically, the output resistance of the composite hydrogel sensor under small and large bending deformation were set as dot and dash, respectively as indicated in **Figure 1-12b**. The English letters and Arabic numbers were recoded and transmitted to electrochemical signals based on finger movement magnitude. Applied in **Figure 1-12c**, every symbol such as representative letters and numbers of O, S and 0, 5 had its peak characteristic based on bending amplitude and exhibited repeatability in twice motions. As an attempt,

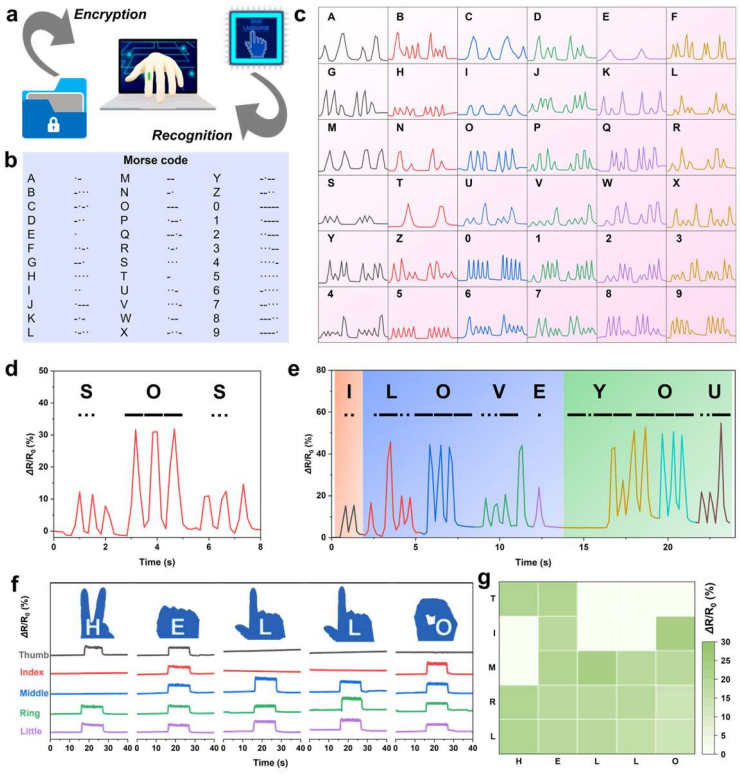

Figure 1-12. Information encryption and decryption according to Morse code and sign language interpretation and transmission application of the hydrogel sensor. (a) Conception of the potential application. (b) The corresponding symbols of the Morse code in the alphabet and numbers. (c) Attaching on fingers to record points and lines in Morse code with relative resistance profile. Practical applications of recoding the signal (d) and long sentence. (e) Sign language transmission by finger gestures: (f) Resistance changes as a function of time to characterize "HELLO" (g) Color intensity mapping of the sign language alphabets.

selected representative messages, such as “SOS” in urgent condition and “I LOVE YOU” were output. Specific and identifiable pattern of the relative resistance were displayed in **Figure 1-12d** and **e**, proving that either a distress message or a phrase could be captured via information encryption and transmission. Additionally, the hydrogels sensor could be employed to translate sign language by monitoring different hand gestures. This convenient method enabled the non-signers to understand the conveyed information in a non-conversational style.[65] For instance, we selected 4 sign language hand gestures (H, E, L, L, O) from American Sign Language (ASL) to represent the unique elements of words. As revealed in **Figure 1-12f**, the subtle motion near finger joints could be monitored by five sensors and matched to the ASL letters. No relative resistance change involved when the fingers were fully straightened, whilst resistance increase on the corresponding sensors if the fingers were curled up. **Figure 1-12g** depicted the differentiated changes of resistance in color matrixes, demonstrating the visual performance of sign-to-language transmission system for recognizing and translating word group. Overall, it is worthy expecting this composite hydrogel sensor to expand new opportunities for health monitoring, information encryption and sign language transmission.

1-4. Conclusions

In summary, the author successfully developed a self-adhesive sign-to-speech transmission system using homogeneous conductive hydrogel composed of functionalized adenine molecules and chi-*g*-PANI copolymers. The quaternate adenine not only acted as adhesive factor for stable adhesion during long-term usage but also promoted the dispersion of rigid polymer network thereby avoided deterioration of mechanical and electrochemical performance. Additionally, the post-crosslinking rigid network providing significant electrical and mechanical properties were homogeneously embedded in the N-glucosamine-Cit^{3-} tridentate coordination assisted matrix. Therefore, the as-assembled conductivity hydrogel sensor demonstrated a high toughness (6.1 MJ m^{-3}), skin-like modulus (184 kPa), high stretchability (1303%), significant sensitivity (GF=2.77, ε=40%–500%), rapid response (166 ms) and superior anti-fatigue-fracture ability (stretched for up to 200 cycles). Based on these, it was applied as a flexible device for human motion detection and expression monitoring due to compatibility with human skin. Based on this, the author fabricated it into a wearable sign

language translation and information encryption system to realize communication between signers and non-signers. The system accurately recognized 26 letters and 10 numbers according to Morse Code and transmitted subtle motion of hand gestures matching to the ASL letters. Consequently, excellent strength, high inspection accuracy, and adhesive properties were integrated together by this DNA-inspired design. Despite the system needs to be improved in achieving outplay function, accelerating translating rates and using in extreme environments, this chapter provides insight into the future use of flexible sensors in artificial intelligence technologies.

1-5. References

1. H. Poizner, *Science*, 1981, **212**, 691-693.
2. Z. Zhou, K. Chen, X. Li, S. Zhang, Y. Wu, Y. Zhou, K. Meng, C. Sun, Q. He, W. Fan, E. Fan, Z. Lin, X. Tan, W. Deng, J. Yang and J. Chen, *Nat. Electron.*, 2020, **3**, 571-578.
3. T. Haug and W. Mann, *J. Deaf Stud. Deaf Educ.*, 2007, **13**, 138-147.
4. G. Morgan, R. Herman and B. Woll, *Int. J. Lang. & Commun. Disord.*, 2007, **42**, 97-105.
5. P. Maharjan, T. Bhatta, M. Salauddin, M. S. Rasel, M. T. Rahman, S. M. S. Rana and J. Y. Park, *Nano Energy*, 2020, **76**, 10507
6. J. Zhao, S. Han, Y. Yang, R. Fu, Y. Ming, C. Lu, H. Liu, H. Gu and W. Chen, *ACS Nano*, 2017, **11**, 8590-8599.
7. W. Xu, S. Hu, Y. Zhao, W. Zhai, Y. Chen, G. Zheng, K. Dai, C. Liu and C. Shen, *Nano Energy*, 2021, **90**, 106606.
8. R. Fuhrer, E. K. Athanassiou, N. A. Luechinger and W. J. Stark, *Small*, 2009, **5**, 383-388.
9. E. P. Gilshteyn, S. Lin, V. A. Kondrashov, D. S. Kopylova, A. P. Tsapenko, A. S. Anisimov, A. J. Hart, X. Zhao and A. G. Nasibulin, *ACS Appl. Mater. Interfaces*, 2018, **10**, 28069-28075.
10. Z. Zhou, C. Qian and W. Yuan, *Compos. Sci. Technol.*, 2021, **203**, 108608.
11. J. Park, J. Jeon, B. Kim, M. S. Lee, S. Park, J. Lim, J. Yi, H. Lee, H. S. Yang and J. Y. Lee, *Adv. Funct. Mater.*, 2020, **30**, 2003759.
12. L. Zhao, H. Zhang, Z. Guo, X. Yu, X. Jiao, M.-H. Li and J. Hu, *ACS Appl. Mater. Interfaces*, 2022, **14**, 51394-51403.

13. J. Bao, Y. Otsuka, H. Ohoyama and T. Matsumoto, *J. Phys. Chem. C*, 2022, **126**, 8029-8036.

14. L. Pan, G. Yu, D. Zhai, H. R. Lee, W. Zhao, N. Liu, H. Wang, B. C.-K. Tee, Y. Shi, Y. Cui and Z. Bao, *Proc. Natl. Acad. Sci. U.S.A.*, 2012, **109**, 9287-9292.

15. M. A. Molina, C. R. Rivarola and C. A. Barbero, *Eur. Polym. J.*, 2011, **47**, 1977-1984.

16. P. Marcasuzaa, S. Reynaud, F. Ehrenfeld, A. Khoukh and J. Desbrieres, *Biomacromolecules*, 2010, **11**, 1684-1691.

17. M. Morimoto, H. Saimoto, H. Usui, Y. Okamoto, S. Minami and Y. Shigemasa, *Biomacromolecules*, 2001, **2**, 1133-1136.

18. K. Okuyama, K. Noguchi, T. Miyazawa, T. Yui and K. Ogawa, *Macromolecules*, 1997, **30**, 5849-5855.

19. H. Liu, Y. Wang, Z. Shi, D. Tan, X. Yang, L. Xiong, G. Li, Y. Lei and L. Xue, *Small Methods*, 2022, **6**, 2200461.

20. S. Li, Y. Cong and J. Fu, *J. Mater. Chem. B*, 2021, **9**, 4423-4443.

21. Y. Gao, F. Jia and G. Gao, *Chem. Eng. J.*, 2019, **375**, 121915.

22. X. Di, J. Hou, M. Yang, G. Wu and P. Sun, *Mater. Horiz.*, 2022, **9**, 3057-3069.

23. H. Zhou, J. Lai, B. Zheng, X. Jin, G. Zhao, H. Liu, W. Chen, A. Ma, X. Li and Y. Wu, *Adv. Funct. Mater.*, 2022, **32**, 2108423.

24. C. Xie, X. Wang, H. He, Y. Ding and X. Lu, *Adv. Funct. Mater.*, 2020, **30**, 1909954.

25. M. Liao, P. Wan, J. Wen, M. Gong, X. Wu, Y. Wang, R. Shi and L. Zhang, *Adv. Funct. Mater.*, 2017, **27**, 1703852.

26. J. Yan, Y. Ji, M. Huang, T. Li, Y. Liu, S. Lü and M. Liu, *ACS Mater. Lett.*, 2020, **2**, 1375-1380.

27. X. Liu, Q. Zhang and G. Gao, *Adv. Funct. Mater.*, 2017, **27**, 1703132.

28. X. Liu, Q. Zhang, L. Duan and G. Gao, *ACS Appl. Mater. Interfaces*, 2019, **11**, 6644-6651.

29. X. Liu, Q. Zhang, Z. Gao, R. Hou and G. Gao, *ACS Appl. Mater. Interfaces*, 2017, **9**, 17645-17652.

30. K. Murakami, R. Tochinai, D. Tachibana, Y. Isano, R. Matsuda, F. Nakamura, Y.

Kurotaki, Y. Isoda, M. Yamane, Y. Sugita, J. Fukuda, K. Ueno, N. Miki, O. Fuchiwaki and H. Ota, *ACS Appl. Mater. Interfaces*, 2022, **14**, 7241-7251.

31. M. T. I. Mredha, Y. Z. Guo, T. Nonoyama, T. Nakajima, T. Kurokawa and J. P. Gong, *Adv. Mater.*, 2018, **30**, 1704937.

32. R. Naraprawatphong, A. Kawamura and T. Miyata, *Polym. J.*, 2018, **50**, 261-269.

33. C. Wang, J. Zhang, H. Chen, Z. Wang, C. Huang and Y. Tan, *J. Mater. Chem. C*, 2022, **10**, 8077-8088.

34. H. Kim, S. Choi, B. Lee, J. Seo, S. Lee, J. Yoon and Y. Hong, *ACS Appl. Mater. Interfaces*, 2022, **14**, 55088-55097.

35. W. Lu, X. Le, J. Zhang, Y. Huang and T. Chen, *Chem. Soc. Rev.*, 2017, **46**, 1284-1294.

36. B. Dudem, R. D. I. G. Dharmasena, R. Riaz, V. Vivekananthan, K. G. U. Wijayantha, P. Lugli, L. Petti and S. R. P. Silva, *ACS Appl. Mater. Interfaces*, 2022, **14**, 5328-5337.

37. A. Fkyerat, M. Demeunynck, J. F. Constant, P. Michon and J. Lhomme, *J. Am. Chem. Soc.*, 1993, **115**, 9952-9959.

38. C. Cui, C. Shao, L. Meng and J. Yang, *ACS Appl. Mater. Interfaces*, 2019, **11**, 39228-39237.

39. Y. Yang, X. Wang, F. Yang, L. Wang and D. Wu, *Adv. Mater.*, 2018, **30**, 1707071.

40. J. Cong, Z. Fan, S. Pan, J. Tian, W. Lian, S. Li, S. Wang, D. Zheng, C. Miao, W. Ding, T. Sun and T. Luo, *ACS Appl. Mater. Interfaces*, 2021, **13**, 34942-34953.

41. Y. Wei, L. Xiang, P. Zhu, Y. Qian, B. Zhao and G. Chen, *Chem. Mater.*, 2021, **33**, 8623-8634.

42. M. Liu, Y. Ishida, Y. Ebina, T. Sasaki, T. Hikima, M. Takata and T. Aida, *Nature*, 2015, **517**, 68-72.

43. X. Shi, Z. Lei and P. Wu, *Sci. China Mater.*, 2022, **65**, 2281-2288.

44. X. Fan, L. Zhao, Q. Ling and H. Gu, *Ind. Eng. Chem. Res.*, 2022, **61**, 3620-3635.

45. S. Tian, Y. Xing, Y. Long, H. Guo, S. Xu, Y. Ma, C. Wen, Q. Li, X. Liu, L. Zhang and J. Yang, *ACS Appl. Mater. Interfaces*, 2022, **14**, 5122-5133.

46. L. Dong, M. Wang, J. Wu, C. Zhu, J. Shi and H. Morikawa, *ACS Appl. Mater. Interfaces*, 2022, **14**, 9126-9137.

47. Y.-Z. Zhang, K. H. Lee, D. H. Anjum, R. Sougrat, Q. Jiang, H. Kim and H. N. Alshareef, *Sci. Adv.*, 2018, **4**, eaat0098.

48. H. Nagahama, H. Maeda, T. Kashiki, R. Jayakumar, T. Furuike and H. Tamura, *Carbohydr. Polym.*, 2009, **76**, 255-260.

49. E. A. Sanches, J. C. Soares, A. C. Mafud, E. G. R. Fernandes, F. L. Leite and Y. P. Mascarenhas, *J. Mol. Struct.*, 2013, **1036**, 121-126.

50. C.-H. Chen, H.-T. Wu, C.-F. Mao and W.-T. Liao, *Polym. Bull.*, 2022, **79**, 6259-6273.

51. W. B. Stockton and M. F. Rubner, *Macromolecules*, 1997, **30**, 2717-2725.

52. K. K. Rajeev, E. Kim, J. Nam, S. Lee, J. Mun and T.-H. Kim, *Electrochim. Acta*, 2020, **333**, 135532.

53. C. Norioka, Y. Inamoto, C. Hajime, A. Kawamura and T. Miyata, *NPG Asia Mater.*, 2021, **13**, 34.

54. Q. Wang, X. Pan, H. Zhang, S. Cao, X. Ma, L. Huang, L. Chen and Y. Ni, *J. Mater. Chem. A*, 2021, **9**, 3968-3975.

55. J. Yu, K. Xu, X. Chen, X. Zhao, Y. Yang, D. Chu, Y. Xu, Q. Zhang, Y. Zhang and Y. Cheng, *Biomacromolecules*, 2021, **22**, 1297-1304.

56. T. Shui, M. Pan, A. Li, H. Fan, J. Wu, Q. Liu and H. Zeng, *Chem. Mater.*, 2022, **34**, 8613-8628.

57. B. J. Kim, D. X. Oh, S. Kim, J. H. Seo, D. S. Hwang, A. Masic, D. K. Han and H. J. Cha, *Biomacromolecules*, 2014, **15**, 1579-1585.

58. Z. He, Z. Zhou and W. Yuan, *ACS Appl. Mater. Interfaces*, 2022, **14**, 38205-38215.

59. X. Di, Q. Ma, Y. Xu, M. Yang, G. Wu and P. Sun, *Mater. Chem. Front.*, 2021, **5**, 315-323.

60. S. D. Sahoo, T. K. Vasudha, V. Muthuvijayan and E. Prasad, *ACS Appl. Polym. Mater.*, 2022, **4**, 9176-9185.

61. Y. Gao, Z. Zhang, X. Ren, F. Jia and G. Gao, *J. Mater. Chem. B*, 2022, **10**, 5743-5752.

62. X. Zou, Y. Chai, H. Ma, Q. Jiang, W. Zhang, X. Ma, X. Wang, H. Lian, X. Huang, J. Ji and M. Xue, *Adv. Mater. Technol.*, 2021, **6**, 2001188.

63. Y. J. Fan, X. Li, S. Y. Kuang, L. Zhang, Y. H. Chen, L. Liu, K. Zhang, S. W. Ma, F.

Liang, T. Wu, Z. L. Wang and G. Zhu, *ACS Nano*, 2018, **12**, 9326-9332.

64. Z. Wang, J. Chen, Y. Cong, H. Zhang, T. Xu, L. Nie and J. Fu, *Chem. Mater.*, 2018, **30**, 8062-8069.

65. J. Wei, Y. Zheng and T. Chen, *Mater. Horiz.*, 2021, **8**, 2761-2770.

Chapter 2
Hydrophobic Association Hydrogel Containing Chitosan for Amphibious Applications

2-1. Introduction

Flexible wearable electronic devices have received growing attention across various fields, including human motion detection, healthcare monitoring, implantable bioelectronics, soft robotics, and energy harvesting.[1-5] Constructing multifunctional and dependable flexible substrates plays a crucial role in fabricating smart stretchable electronic devices. So far, a variety of chemistry substrates materials such as flexible plastic, fabrics, liquid metal and conductive elastomers, have gained considerable interest by researchers.[6-8] Among them, conductive hydrogels have become the most promising candidates for developing flexible electronics due to their biocompatibility, tunable mechanical strength, and customizable electronic performance.[9-11] Although tremendous progress has been made in conventional hydrogel sensors for terrestrial sensing, it remains challenging to avoid hydrogel swelling, maintain mechanical stability, and accurately detect electrophysiological signals by skin-worn sensors within dangerous and rigorous aquatic environments.[12-14] Therefore, multifunctional hydrophobic hydrogel electronics that can not only ensure the application in land environment but also sustain complicated water condition are highly desired.[15-17]

So far, a great deal of effort has been devoted to designing anti-swelling hydrogel materials, including increment of chemical cross-linking density, introduction of hydrophobic associations (HA), solvent exchange, and ionic complex.[18-22] As a facile and time-saving strategy to prepare water-resistance hydrogels, HA which can be achieved by micellar copolymerization between hydrophilic and hydrophobic monomers, can assist the hydrophobic molecules or groups aggregate with each other in water.[23, 24] Then, the hydrophobic segments are connected around the micelles formed by the surfactants and become physical cross-linking points.[25] Meanwhile, the entangled network of hydrophobic chain segments significantly dissipates energy through disentanglement or sliding, thus upgrading the toughness of hydrogels.[26] Qi *et al*. have demonstrated tough, robust wet-adhesive and anti-swelling supramolecular hydrogels by exploiting the multiple interactions between the cationic surfactant cetyltrimethylammonium

bromide (CTAB) and the copolymer of a hydrophilic monomer and hydrophobic lauryl methacrylate.[27] Tuncaboylu *et al*. obtained tough and self-healing hydrogels via copolymerizing hydrophilic acrylamide with hydrophobic monomer stearyl methacrylate or dococyl acrylate in sodium dodecyl sulfate and sodium chloride electrolyte.[28, 29] Nevertheless, the complicated adhesion generating processes, limited mechanical tensile and weak electrical conductivity, are still existing problems in HA alone hydrogels. Therefore, developing high performance and multifunctional HA hydrogels using eco-friendly materials in convenient and universal method has become a trend of research.[30]

As an effective attempt, introducing synergistic electrostatic interactions into hydrophobic hydrogels can not only realize the adhesion characteristics but also improve the mechanical properties.[31, 32] For instance, Huang *et al*. reported the hybrid hydrogels with ionically and hydrophobically cross-linked networks, where the dynamic electrostatic interactions in hydrophobic hydrogels tuned the size of hydrophobic domains well-orderly.[33] The hydrogel was feasible to adhere to various substrates and exhibited great potential in different fields. In addition, the ionic surfactants as cross-linking points can attract opposite charged species in the solution to form second cross-linking centers, thereby reinforcing the polymer structure with enhanced fracture toughness and stress. Demott *et al*. successfully combined triple network hydrogels as cartilage substitutes with synergistically intra-network effects of HA and electrostatic repulsive, as well as electrostatic attractive interactions within inter-network.[34] Despite the corresponding advantages, a flexible hydrogel strain sensor still demands to possess superior electrochemical performance, long-term stability, and transparency to function effectively.[35] Additionally, it is vital to prepare self-adhesive hydrophobic hydrogel without complicated process of solvent replacement.[36] Rational regulation of polymer network through a simple and universal soaking strategy will be of huge significance.[37, 38]

Phytic acid (primary form of phosphorus storage in seeds and grains) was used as the gelator and dopant to form polyaniline hydrogel with record-breaking conductivity.[39] As its derivative, sodium phytate (PANa) possesses high ionization degree and abundant acceptor sites of hydrogen bonds.[40, 41] Hence, it is potential that the PANa can prevent the water crystallization and evaporation within the gels by hydrogen bonding with water. Chitosan, the deacetylation

product of chitin, is a biopolymer extracted from shellfish such as crabs and shrimps.[42] Researchers discovered that chitosan underwent cross-linking through chain entanglement, which was initiated by shielded electrostatic repulsions between amino groups through the hydrogel soaked in a high-concentration salt solution.[43] Therefore, it is expected to stimulate the advancement of environmentally stable and multi-scenario capable electronic devices by immersing chitosan hydrogels into saturated PANa solution, thereby enhancing their moisture retention, mechanical robustness, and wet-adhesion behavior.[44]

Herein, the author developed a hydrogel for multi-scenario application, which was composed of chitosan and electrostatic hydrophobically associated network by an efficient and simple two-step strategy. First of all, the hydrophilic monomer acrylic acid (AA) and *N*-(2-hydroxyethyl) acrylamide (HEAA) and the hydrophobic monomers myristyl methacrylate (MMA) were random copolymerized with the help of the catanionic micelles of CTAB after ultrasonic dispersion. On the one hand, the weak acidic environment provided by the ionization of low concentrated AA would promote the dissolution of chitosan; and the neutral HEAA monomer contains amide (–CO–NH–) and hydroxyl (–OH) groups simultaneously, which not only mimic the cement proteins of barnacles after co-polymerization but also facilitate the adhesion behavior through hydrogen bonding. On the other hand, the hydrophobic segments endow the gel with certain ability to resist swelling and prevent water molecules from invading the adhesion interface. Then, the pre-synthesized hydrogel was soaked in statured PANa solution, resulting in (i) the chain entanglement of chitosan backbone under shielded electrostatic repulsions and (ii) dynamic electrostatic interactions between the phosphate groups and quaternary ammonium micelles. It is worth noting that the strong hydrogen-bonding interactions between PANa and water molecules endowed the gel with a certain dehydration resistance. Overall, the multifunctional hydrogel with comprehensive performance was assembled as a sensing module to detect human motion and transmits information using Morse code in both terrestrial and aquatic environment. This chapter provided a new approach to designing and preparing conductive hydrogels for health monitoring electrodes and intelligent information communicators.

2-2. Experimental Section

Materials

Chitosan 10 was offered by Fujifilm Wako Pure Chemical Corporation (Osaka, Japan). Myristyl methacrylate (MMA) was purchased from Nacalai Tesque Inc. (Kyoto, Japan). Acrylic acid (AA), sodium phytate (PANa), cetyltrimethylammonium bromide (CTAB), 2,2'-azobis(2-methylpropionamide) dihydrochloride (AIBA) and *N*-(2-hydroxyethyl)acrylamide) (HEAA) were purchased from Fujifilm Wako Pure Chemical Corporation (Osaka, Japan). Deionized water with a conductivity of 0.24 μS cm^{-1}, which was doubly distilled and purified using the Milli-Q system from Millipore Corp (Milford, MA, USA). All chemicals were used as received without further purification.

Synthesis of HA hydrogel

The HA hydrogel was prepared by in-situ free radical polymerization between hydrophilic monomers and hydrophobic micelles in the presence of chitosan. Typically, CTAB (3.0 g) and MMA (1.18 mL, 3 mol%) were dissolved in 20 mL of deionized water at 50 °C under magnetic stirring. After the bubbles disappeared and a transparent micelle dispersion formed, the AA (1 mL) and HEAA (10.69 mL) were added into the mixture when it cooled to room temperature. Subsequently, 0.3 g of chitosan encountered the microemulsion under ultrasonic radiation for 3 min. Afterward, 36 mg of AIBA as the thermal initiator was mixed and homogeneously stirred, followed by poured the precursor into a customized mold. Finally, the HA hydrogel was obtained after one-pot polymerization at 50 °C for 6 h.

Preparation of the electrostatic interacted HA hydrogel

The as-prepared HA hydrogel was immersed into a serious of PANa solution (mass concentrations of 18.11%, 36.22% and 54.34%) for different time to obtain the electrostatic interacted HA hydrogel. After a soaking process for 45 min, the chitosan formed efficacious chain entanglement in statured PANa solution.

General characterization

Attenuated total reflection Fourier transform infrared (ATR-FTIR) spectra over the wavenumbers ranging from 4000 to 500 cm^{-1} for the raw materials and hydrogels were recorded

at room temperature with a Nicolet iS5 spectrometer (Thermo Fisher Scientific). The X-ray diffraction (XRD) patterns were acquired using SmartLab (Rigaku Corporation) with a scanning speed of 5° min^{-1} over the 2θ range of 10–80°. The cross section of the fractured lyophilized hydrogels was captured by scanning electron microscopy (SEM, SU3500, Hitachi Ltd., Tokyo, Japan) and Energy Dispersive X-ray Spectroscopy (SEM-EDX), and Miniscope TM3000 equipped with a Swift ED 3000 (Hitachi Ltd., Tokyo, Japan). The chemical compositions and structures of the PANA and intermidiate and final hydrogels were counducted by X-ray photoelectron spectroscopy (XPS, JEOL JPS-9010MC, Japan). The precursor was dispersed by Violamo ultrasonic homogenizer (Sonicstar 85, Japan). The optical transparency measurement of the hydrogels with thickness of 1 mm and 2 mm was conducted in quartz cells through UV-vis spectrophotometer (J-820 AC, JASCO Corporation, Japan).

Mechanical tests and rheology analysis

The mechanical properties of the hydrogel samples were tested using a universal material testing machine (Shimadzu AGS-X, Shimadzu Corporation, Japan) with a 100 N load cell at room temperature. The samples were cut into rectangular samples with 2 mm thickness, 10 mm inner width, and 20 mm gauge length, and the distance of the clamps was set as 10 mm for all the tensile tests. The stretching rate was set at 100 mm min^{-1} for strectching test and loading-unloading cyclic tests. The tensile strain (ε) was defined as the change in the length (l) relative to the gauge length (l_0) of the each specimen. The tensile stress σ was determined by the ratio between the load force (F) and the cross-sectional area (S). The elastic modulus (E) was calculated from the slope in the initial linear region in the range 5–15% of the stress.[45] The thoughness (U)[46] was calucated by the equation as follow:

$$U = \int \sigma d\varepsilon \tag{2-1}$$

For the loading-unloading curves for various strains, the dissipation coefficient (DC)[47] and elastic recovery (ER)[48] was calculated with the following formulas:

$$\mathrm{DC} = 100\% \times \left[\left(\int_{loading} \sigma \, d\varepsilon - \int_{unloading} \sigma \, d\varepsilon \right) / \int_{loading} \sigma \, d\varepsilon \right] \tag{2-2}$$

$$\mathrm{ER} = 100\% \times \frac{\varepsilon_{max}-\varepsilon_b}{\varepsilon_{max}-\varepsilon_a} \quad (2\text{-}3)$$

where ε_{max} is the maximum strain (500%) of the loading cycle, ε_b is the strain under zero stress of the unloading cycle, and ε_a is the strain under zero stress of the loading cycle.

The hydrogels were placed at the bottom of the parallel plates to investigate their viscoelastic behaviors using HAAKE RheoStress 6000 (Thermo Fisher Scientific). The oscillation frequency sweep in the linear viscoelastic region was conducted from 0.1 to 100 Hz at 0.1% strain under 25 °C.[49] And the variations of the storage modulus (G') and loss modulus (G'') were measured under the oscillation strain of 0.1~1000%.[50]

Adhesion test in air and underwater

The Shimadzu EZ-Graph universal testing machine equipped with a 10 N load cell and at 50 mm min^{-1} stretching rate was used to measure the adhesion performance toward diverse substrates of metal, porcine skin, wood, glass, plastic and polytetrafluoroethylene (PTFE) until the hydrogel interfaces were completely separated. The specimen with a bonded area of 10 mm × 10 mm was sandwiched in the surfaces attached to the plates. The maximum load was the adhesion strength through the adhesion force-displacement curves.[51] The materials were immersed in a tank full of water to test the underwater adhesion strength.[52] The pictures of underwater adhesion were taken by a compression method. The compressing process was kept for 30 s, and then the hydrogel attached to the substrate was pulled out in the water.

Electrical performance

The electrostatic interacted HA hydrogel was attached to the human body to monitor the physiological signals. The signal was transmitted into the relative resistance change under different strains as well as varied frequencies, which was measured by an using an inductance, capacitance, and resistance (LCR) meter (TH2830, Changzhou Tonghui Electronic Co. Ltd., China) with a size of 20 mm × 10 mm × 2 mm. The relative resistance change was computed as the following formula[53]:

$$\frac{\Delta R}{R_0} = \frac{|R-R_0|}{R_0} \times 100\% \quad (2\text{-}4)$$

where R and R_0 represented the resistance caused by hydrogel deformation and the initial resistance of the hydrogel, respectively.

The electrical sensitivity was denoted as gauge factor (GF), which was calculated by the equation[54]:

$$\mathrm{GF} = \frac{\Delta R}{R_0 \varepsilon} \tag{2-5}$$

where ε was the corresponding strain change.

2-3. Results and discussion

Design and preparation of the HA hydrogels

In a typical experiment, the electrostatic HA hydrogel was fabricated via a two-step strategy of random copolymerization and post-soaking method (**Figure 2-1**). Considering the balance of optimal performance, the amount of the hydrophobic monomers was of 3 mol% to the total monomers, which would be discussed below, unless otherwise specified. Initially, the micelles with average size were formed through the alkyl chain interactions of C_{14} unit in MMA with cationic surfactant CTAB. After ultrasound dispersion of chitosan and precursors, the free radical polymerization including hydrophilic monomer AA, HEAA and hydrophobic monomer MMA was carried out in a one-pot method, with CTAB as crosslinking sites and 2,2'-azobis(2-methylpropionamide)dihydrochloride (AIBA) as the thermal initiator. Interestingly, the droplets aggregation could be avoided owing to the amphiphilic regions in chitosan.[55] The hydrophobic segments were stabilized to create a uniform hydrogel network through the chitosan, with the hydrophilic parts extending into the water, yet hydrophobic regions anchoring molecules on droplets surfaces.[56] Subsequently, the obtained HA hydrogel was soaked in PANa

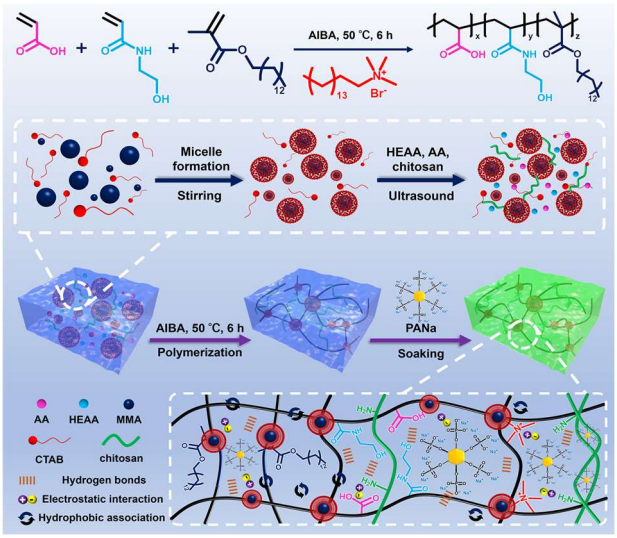

Figure 2-1. Mechanism illustration of constructing multiple physical interacted hydrophobic association hydrogel based on a "two-step" strategy.

solution for the second network formation.[41] In this process, the phosphate groups were permeated into the HA hydrogel because of the high osmotic gradient, then the *N*-glucosamine units within the chitosan backbone electrostatic attracted with the massive negatively charged phosphate; hence, the chain-entanglement network formed because of the spontaneous collapse of chitosan chains.[57] Besides, high density of hydrogen bonds formed between chitosan chains and PANa.[58] By harnessing the synergistic effects of multiple physical interactions, the hydrogel becomes a promising candidate for mechanical robust, water-resistant, and self-adhesive strain sensors.

Structure and Characterization of the HA Hydrogels

In **Figure 2-2a–c**, the morphology structure of the non-chitosan contained HA hydrogel, HA hydrogel and soaked HA hydrogel were shown, respectively. It was apparent that three dimensional (3D) interconnected micropores presented at the lyophilized cross section. The scanning electron microscope (SEM) image also revealed a great number of hydrophobic alkyl chains intertwined around the hydrophobic micelles. It evidently demonstrated the anti-swelling properties should be attributed to the massive hydrophobic crosslinking sites.[59] Different from the unevenly distributed porous network, the network of HA hydrogel with chitosan in the diagram exhibited an orderly distribution. This uniform distribution of polymer chain was due to the mutual repulsion between the positively charged amino groups on chitosan backbone and the similarly charged quaternary ammonium salts in CTAB.[60] Furthermore, the "honeycomb-like" network structure indicated that the as-prepared hydrogel had an ideal surface to transfer water molecules and ions,[61] which assisted the interaction between polymer chains and the ions of PANa in the following step. As shown in **Figure 2-2c, d**, the soaked HA hydrogel had an expected morphology as well as energy-dispersive X-ray spectroscopy (EDS) mapping visually proved the categories and distribution

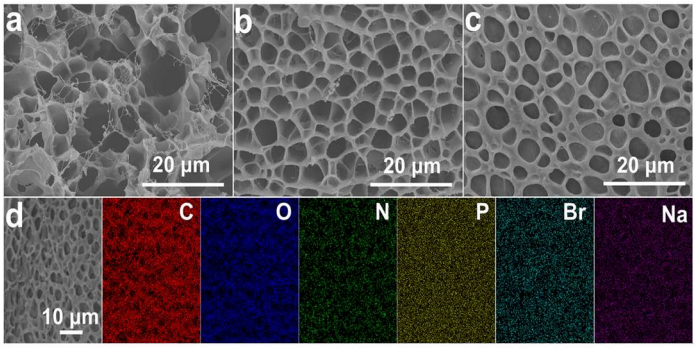

Figure 2-2. Cross-sectional SEM images of (a) HA hydrogel in absence of chitosan. (b) HA hydrogel, and (c) HA hydrogel after soaked in PANa solution. (d) The corresponding EDS images of soaked HA hydrogel.

of elements in the gel. It was obvious that the hydrophobic alkyl chains stacked on the surface of immersed HA hydrogel and demonstrated a wrinkled structure. The phenomenon could be attributed to the increased crosslink density caused by strong hydrogen bonding and chain entanglement.[62] As a result, the synergies of physical interactions and interconnected conductive path was potentially beneficial for the mechanical properties and electronic performance of the hydrogel.

To examine the key elements presence and hydrogen bonding interaction in the gel, X-ray photoelectron spectroscopy (XPS) was conducted. As illustrated in the **Figure 2-3a**, the elements of O, N, C, P were confirmed, which were consistent with the raw materials used. Next, more specific XPS analysis of high-resolution spectrum can determine the effect of soaking process on the hydrogel. The high-resolution spectrum of C 1s orbit for both HA hydrogels could be deconvoluted into three characteristic peaks: the C=C/C–C (284.8 eV), C–N (286.3 eV), and C=O/C–O bond (289 eV) (**Figure 2-3b** and **c**).[63] In **Figure 2-3d**, the comparison XPS spectra between PANa and soaked gel was evidence to confirm the hydrogen bonding interaction. The characteristic peaks at 132 and 131 eV were assigned to the P=O groups of PANa, and PANa soaked hydrogel, respectively.[41] The decreased binding energy indicated the formation of hydrogen bonds in hydrogel, where the PANa could serve as a salt to intensify the conversion of polymer aggregation.[64]

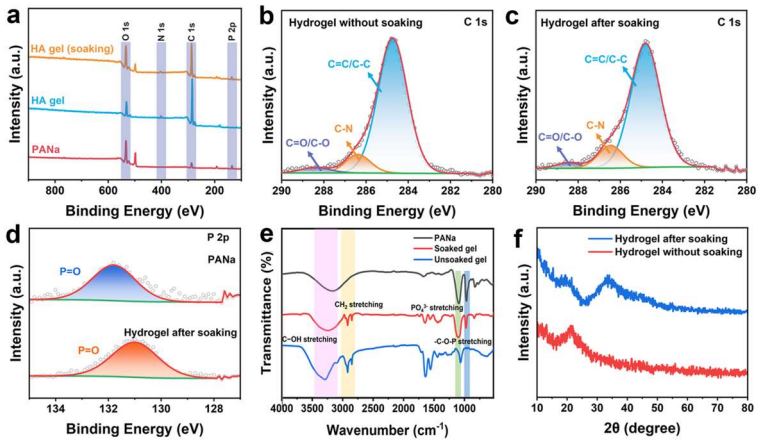

Figure 2-3. (a) XPS survey spectrums of HA hydrogel without and after soaking, and PANa. (b, c) high resolution spectra of the corresponding hydrogels. (d) The comparison XPS spectrum of PANa and soaked hydrogel. (e) FTIR spectra of PANa, soaked hydrogel and unsoaked hydrogel; (f) XRD patterns of the different HA hydrogels.

Attenuated total reflectance Fourier-transform infrared (ATR-FTIR) spectroscopy was employed to further analyze the chemical structure and interaction of the HA hydrogel related materials (**Figure 2-3e**). PANa exhibited typical stretching vibrations of the HPO_4^{2-}, PO_4^{3-} and C–O–P groups around 1656 cm^{-1}, 1090 cm^{-1} and 992 cm^{-1}, respectively.[41, 63] Although there

was a red shift in both PO_4^{3-} and C–O–P stretching vibration in the PANa immersed hydrogel, the broadened peak could be attributed to the influence of hydrogen bonds that impaired the original bond energy.[65] The same phenomenon occurred in the comparison spectrum of HA hydrogels. Specifically, the characteristic peaks at 3286 cm^{-1} and 2896 cm^{-1} corresponding to C–OH stretching and CH_2 stretching in hydrogel without soaking shifted to lower wavenumber of 3256 cm^{-1} and 2880 cm^{-1}. The weakened the chemical driving force leaded to declined vibration frequency of the chemical bonds.[66] Therefore, it further confirmed that the formed hydrogen bonding in chitosan network and gel polymer backbone. The XRD pattern of the HA hydrogel without soaking showed low intensity characteristic peaks at around 20°, which is superimposed crystallization diffraction of (220)/(200) crystal plane for chitosan crystal hydrates.[67] However, the salting out effect led to a decrease of crystal plane spacing and crystallinity as evidenced in **Figure 2-3f**, demonstrating the influence of PANa on the aggregated structure of chitosan in both pristine and dehydrated hydrogels.

Mechanical and Viscoelastic Properties

The presence of hydrophobic monomer and chitosan is crucial to affect the mechanical properties, which even determines the sensing reliability of the conductive hydrogel. Therefore, the mechanical properties reflecting the influence of MMA (from 1–5 mol%) were systematically investigated by universal tensile test (**Figure 2-4**). From the typical stress-strain curves, the HA hydrogels showed an improved tensile strength while the tensile strain decreased with the increase of MMA concentration from 3 to 5 mol%. When the MMA was increased to 3 mol%, the HA hydrogel formed enough cross-linked structure interacted between CTAB and MMA, thereby improving the tensile properties. Although the hydrogel with 4–5 mol% MMA

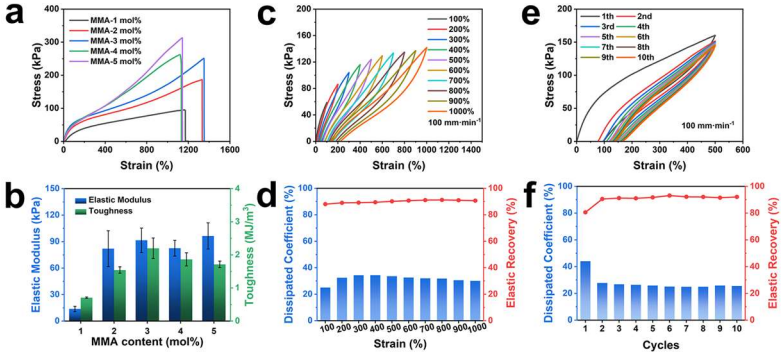

Figure 2-4. Mechanical properties of the HA hydrogels (a, b) Tensile stress-strain curves of hydrogels with different addition of hydrophobic monomer MMA and the corresponding calculated elastic modulus and toughness of the hydrogels. (c, d) The successive loading-unloading curves under the strain from 100 to 1000% and the corresponding energy dissipating coefficient and elastic recovery ratio. (e, f) Cyclic curves under 500% strain for 10 cycles and the calculated energy dissipation coefficient and elastic recovery.

exhibited high strength, both had impaired stretchability less than 1200% due to the inhomogeneous distribution of redundant MMA segments.[68] Based on the results, we believe that the HA hydrogel could obtain optimal mechanical performance with fracture stress of 255 kPa and stretchability of 1360%. Furthermore, the calculated elastic modulus and toughness in **Figure 2-4b** another piece of evidence to prove the superior elasticity and strength, and the MMA-3 mol% HA hydrogel reached the highest toughness of 2.28 MJ m^{-3} and Young's modulus exceeding 90 kPa.

To further prove the elasticity and restoration of the MMA-3 mol% HA hydrogel, loading-unloading test was conducted. The curves in **Figure 2-4c** and **d**, showed the typical cycling test under different strains ranging from 100% to 1000% and their corresponding results of dissipated coefficient and elastic recovery. It could be observed that the HA gels at different strains exhibited increasing hysteresis loops, indicating an effective energy dissipation.[48] As the strain increased, the hydrogel dissipated more energy, while achieving a stable energy dissipation ratio around 30% and elastic recovery of 90%. This phenomenon could be explained by the synergistic effects of various physical interactions.[69] For example, the hydrophobic segments detached at small strains, breaking into small clusters for effective energy dissipation, but reconstructed into a network accompanied by chitosan through the reversible nature of hydrogen bonds.[70] Moreover, the stress-strain curves of the hydrogel exhibited distinct hysteresis loops at fixed strain of 500% (**Figure 2-4e**). As far as known, the inner polymer network of hydrogel was easily to be weakened in a large extent thereby cannot be instantly restored after the first loading. However, after the following nine stretching cycles, there were no apparent shape and stress loss, so that the hydrogel could partly recover because of the reconstruction of multiple physical interactions.[71] The dissipated energy and resilience were analyzed in **Figure 2-4f**. The quantified energy dissipation was stabilized around 80–100 kJ m^{-3} except the first cycle and the value of elastic recovery maintained 90%, which demonstrated high elasticity and self-adaptability to successive stretching. This was mainly due to the multistage physical interactions and hydrophobic domains.[57]

However, the single effectual HA hydrogel was unable to form the secondary chitosan network structure and dynamic electrostatic interactions. Consequently, the mechanical strength,

swelling resistance, adhesive behavior and electronic performance failed in meeting the requirements of a flexible sensor. Soaking in PANa solution as a facile and effective strategy was adopted in the following research. As shown in **Figure 2-5**, the tensile behaviors of the hydrogels soaked in different time and different solution concentration were compared. The tensile strength and strain increased to 430 kPa and 1500%, respectively with the increasing PANa solution concentration, indicating that the hydrogels could absorb large amounts of ions under high osmotic pressure. Moreover, immersing the hydrogel in statured solution for 45 minutes was sufficient to endow it with optimal stiffness and toughness. The strong electrostatic interaction promoted chain entanglement of chitosan, that comprised the strong interpenetration with hydrophobic domains and enhanced the mechanical strength.[43]

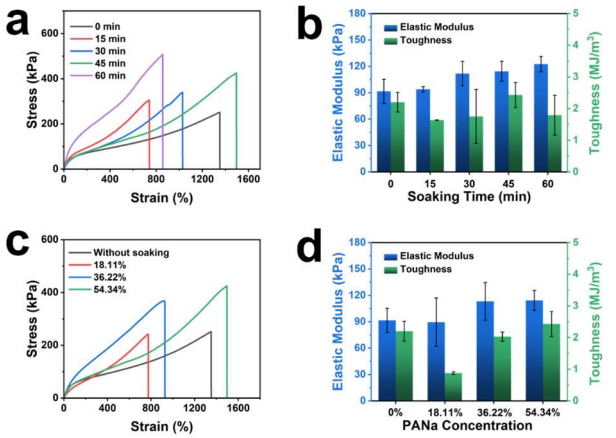

Figure 2-5. (a) Tensile strain curve of the HA hydrogels immersed in PANa statured solution for 15, 30, 45 and 60 min. (b) Their corresponding elastic modulus and toughness. (c) Tensile strain curve of the HA hydrogels immersed in PANa solution of different concentration for 45 min. (d) Their corresponding elastic modulus and toughness.

Correspondingly, the excellent hysteresis and shape recovery behavior induced by the multistage dynamic bonds were investigated in **Figure 2-6a–e**. The ten successive cyclic tensile loading-unloading curves displayed a noticeable hysteresis loop with residual strain, indicating a significant capacity for energy dissipation. The larger hysteresis area of the first cycle reflected the dissociation of entanglement and hydrogen bonds broken and the following nine cycles showed a significant recovery of dynamic bonds.[57, 71] In contrast, the elastic recover ratio and dissipated coefficient became 95% and 22% respectively in following cycles, which indicated that the post-immersing hydrogel was incorporated with massive electrostatic interactions to reverse the self-recovery ability rapidly. The hysteresis loop in cyclic loading-unloading tests at different strains from 100% to 1000% was positively correlated with the tensile strain in **Figure 2-6c**. More dynamical bonding after soaking played an important role in efficiently consuming the internal network energy when subjected to external stress. Therefore, the

electrostatic interacting HA hydrogel performed high elasticity and self-adaptability to cyclic stretching within a wide strain range of 400%–1000%. As intuitive evidence, the optical pictures in **Figure 2-6e** demonstrated the soaked HA hydrogel possessing significant robustness and toughness. It could be not only directly stretched to fourteen times of its original length, but also easily stretched in twisting and knotting states.

The viscoelastic behavior of the electrostatic HA hydrogels without and after soaking were performed by oscillatory rheology measurements at 25 °C. **Figure 2-6f** showed the frequency dependence of G' and the G''. Both values increased with the increase of the angular frequency, whereas G' was consistently greater than G'' indicating the typical elastic solid-like behavior of hydrogel. The value of G' after post-soaking was consistently higher than that without immersing, which demonstrated an enhanced elasticity and could be attributed to the abundant dynamic effects of HA interactions and hydrogen bonds. Besides, there was no significant change for G' and G'' when subjected to low range strain in **Figure 2-6g**. The G' value of unsoaked gel dramatically decreased at 8% strain and intersected G'' at 11% strain. However, in a soaked hydrogel, the G' sharply decreased at 30%, illustrating enormous dissipating energy made it more resistant to collapse.[72] And the significantly improved intersection strain of 150% also proved that electrostatic interactions enhanced

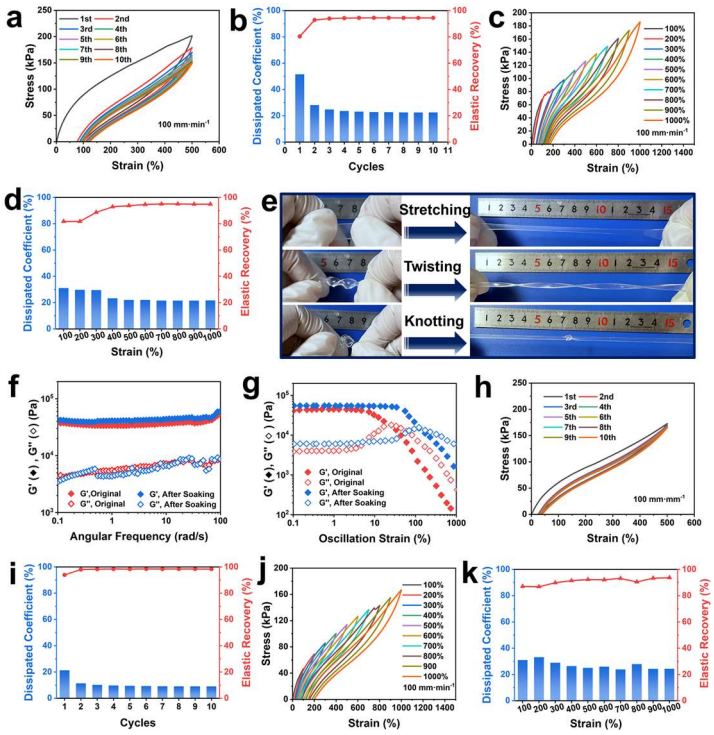

Figure 2-6. Mechanical properties of the hydrogels in air (a) Cyclic strain test under 500% stretching for 10 cycles. (b) The corresponding energy dissipation and elastic recovery. (c, d) Successive tensile loading-unloading curves of the electrostatic interacting HA hydrogel at different strain and their corresponding energy dissipation coefficient and elastic recovery. (e) The optical images of manual stretching of hydrogels in different deformation forms; rheology analysis of the gel. (f, g) The rheological behavior at varying angular frequencies and the dynamic shear scanning. Mechanical properties of the electrostatic interacted HA hydrogels underwater (h, i) Consecutive loading-unloading stress curve at a strain of 500% (10 cycles), and the calculated hysteresis ratio and elastic recovery; (j, k) Loading-unloading strain curves ranging from 100 to 1000% and the corresponding dissipating coefficient and elastic recovery.

hydrophobic domain could resist deformation effectively.

For underwater application, the hydrogel was necessary to show mechanical response to external strain in aquatic condition. The dissipating energy capability of the as-soaked HA hydrogel underwater was examined by cyclic loading-unloading tests (**Figure 2-6h–k**). The hydrogel exhibited a negligible hysteresis loop in deionized water after ten successive cycles stretches under 500% strain. The hysteresis ratio kept at 8% with an energy dissipation of 43 $kJ \cdot m^{-3}$ and showed an excellent resilience of 95% elastic recovery. As shown from **Figure 2-6j**, expanding hysteresis loops appeared when applied the hydrogel to different strain from 100% to 1000%. But the material showed a stable energy dissipating coefficient (30%) and elastic recovery (95%), indicating an excellent mechanical performance underwater application. Although the overall trend is consistent, the author speculated that the low hysteresis underwater could be attributed to inhibitory formation of extensive hydrophobic domains.[31] Since the hydrogen bonding with water enhanced polymer-water interaction force, the equilibrium with elastic retractive force induced by electrostatic interactions between PANa and HA segments was influenced, resulting in weakened mechanical performance underwater.[73] The results were consistent with interval rest cyclic tensile experiments, thereby the hydrogel displayed favorable endurance and compliance in multiple environments.

Adhesive Performance and Underwater Stability

In addition to excellent mechanical properties, hydrogels exploited as wearable sensor need to achieve functional characteristics. The hydrogel could adhere to diverse substrate materials including paper, stone, porcine skin, metal, rubber, and ceramics etc. without extra auxiliary binders (**Figure 2-7a**). Therefore, the lap shear test was employed to quantify the self-adhesion capability. In **Figure 2-7b** and **e**, the hydrogel showed the highest adhesion strength to metal surface due to the synergistic effect of van der Waals force and hydrogen bonding generated between hydrogel and the metallic surface.[74] Moreover, the electrostatic interactions and strong hydrogen bonds were two main effects responsible for the adhesion towards ceramics, plastic, polytetrafluoroethylene (PTFE), glass, rubber and porcine skin etc. Besides, the effective adhesion based on reversible physical interactions exhibits reproducibility and durability

(**Figure 2-7f**). After cyclic shear experiments, although the adhesion strength decreased slightly in cyclic shear experiments, it still maintained over 67% of the initial value after five peelings. Therefore, the reversible physical interaction endowed the gel good compatibility and reproducible adhesion, enabling the materials to chronically adhere to various substrates without external assistance. It showed great application potential without compromising the mechanical properties in wearable strain sensors.

The adhesive behavior of the soaked hydrogel underwater to diverse substrates were also investigated. The hydrophobic interface could disrupt the hydration layer formed on the hydrogel surface, facilitating the establishment of a robust connection between the target interfaces. Therefore, after 30 s compression, the hydrogel showed stable adhesion to various substrates in both air and underwater (**Figure 2-7d**). Although the wet adhesion forces were slightly reduced during five successive experiments (**Figure 2-7g**), the hydrogel still demonstrated effectively robust and long-term underwater adhesion for practical application. The hydrophobic micelles, electrostatic interactions and ultrasonic recombination not only offered several adhesive mechanisms but also prevented the water molecules invading the contacting interfaces.[75]

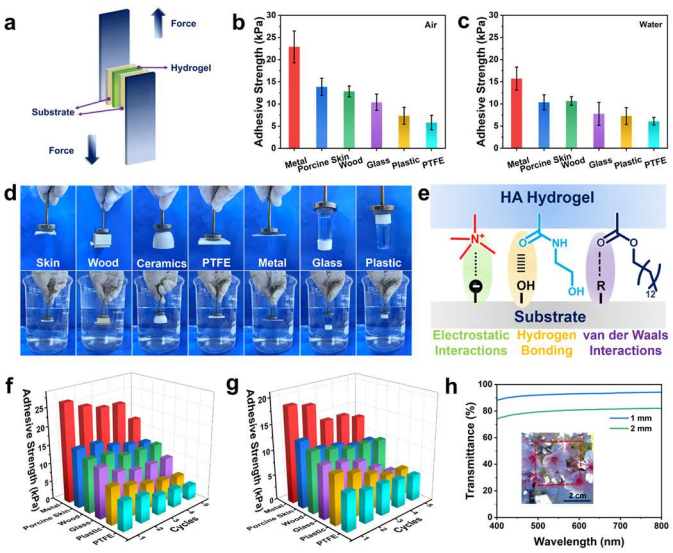

Figure 2-7. Adhesion behavior of the hydrogel (a) Schematic of the lap shear test. (b, c) Lap-shear adhesion strength of the hydrogels on diverse substrates in air and underwater, respectively. (d) Photographs of the hydrogel adhering to different substrates in the air and underwater. (e) Illustration of the adhesion mechanism. (f, g) The repeatable adhesive strength curves of the hydrogels to various substrates conducted by 5 successive attaching-detaching process (in air and underwater). (h) Optical transparency of the electrostatic interacted HA hydrogel.

Generally, the hydrophobic hydrogels were prone to become opaque due to the formation of heterogeneous hydrophobic domain in water. It was necessary to explore the transparency of hydrogels accompanied by underwater adhesion. As shown in **Figure 2-7h**, the hydrogel was highly transparent at room temperature because the inset pattern covered by a hydrogel could be clearly observed. The UV-vis transmittance for hydrogels with thickness of 1 mm and 2 mm

reached over 90% and 80% at a wavelength of 550 nm, which was enough for visualization wearable sensors.

Electromechanical Properties

The strain sensitivity in a wide range were investigated in air and water, respectively. Because of the reliable mechanical performance both in air and underwater, the varying resistance of hydrogel contributed to the LED luminance change. In air, the GF, calculated by the ratio of relative resistance change ($\Delta R/R_0$) to strain (ε), were divided into three regions (**Figure 2-8a**). Specifically, the GF values were 1.42, 2.33 and 3.54 in the strain range of 0–110%, 110%–300% and 300%–500%, respectively, and each complied with a high linearity with the applied strain. The trait of hydrogel acting like human epidermis was derived from the excellent strain sensitivity on the basis of ionic conductivity and mechanical properties. As shown in **Figure 2-8b**, the resistance changes ratio demonstrated the repeatability and strain dependency from 100% to 500% strains at the five stretching-releasing cycles Besides, at a fixed strain of 50%, the hydrogel could distinguish the varying frequencies and exhibited unanimous relative resistance peaks (**Figure 2-8c**). Therefore, it was obvious that the hydrogel system possessed superior signal stability and repeatability. Notably, a significantly fast response time (198 ms) and recovery time (300 ms) were detected to evaluate signal response speed (**Figure 2-8d**). The responding rates were sufficient to meet the requirements of real-time human motions monitoring. Most importantly, the hydrogel sensor suffered minor signal attenuation and drift upon consecutive cycles for 200 times at 50% strain, indicating the satisfying durability.

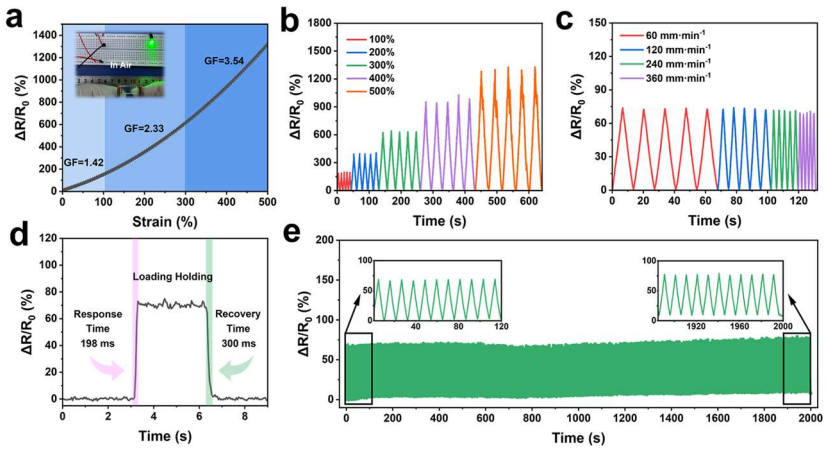

Figure 2-8. Electrical sensing performances of the hydrogel strain sensor in air (a) Relative resistance changes with strain in the range of 0-500%. (b, c) The relative resistance changes under representative strain and frequencies; (d) Response and recovery time curve of the hydrogel sensor. (e) The repetitive resistance changes upon cyclic stability test at a fixed strain of 50%.

Alternatively, corresponding electromechanical measurements underwater were carried out. As shown in **Figure 2-9a**, the GF reflecting underwater was calculated, where the relative resistance increased linearly upward with strain. The GF value reached 1.45 in the strain range of 0–500%, which was superior performance compared with reported parameters underwater.[17] The decreased GF in water was attributed to that conductive pathway in a homogeneously ordered hydrophobic structure facilitated ion transmission, yet fewer freely moving ions reduced the sensitivity. This phenomenon was also confirmed by the underwater sensing when applied with different strains and frequencies (**Figure 2-9b** and **c**). It was observed that the hydrogel showed good responsiveness to the stretching-relaxation process, proving that it had excellent underwater sensitivity to different strain amplitudes. Even if the stretching speed changes, the resistance change ratio remained basically unchanged, indicating that the hydrogel had favorable sensing stability. Moreover, in **Figure 2-9d**, the underwater strain sensor displayed faster response and recovery times of 190 and 140 ms, respectively, demonstrating a perception speed close to human skin.[23] To prove the long-term electromechanical stability, 200 cycles of continuous stretching at 50% strain were conducted. As shown in **Figure 2-9e**, the relative resistance change maintained almost the same in whole repeated period. Owing to the well-ordered hydrophobic structure, the ions could transfer freely in water environment. Overall, the high flexibility, strain-sensing stability and durability ensured the underwater sensor prominent reliability.

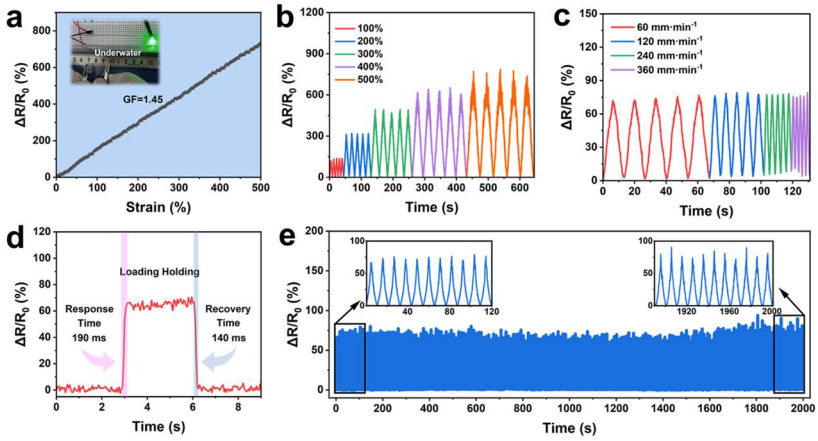

Figure 2-9. Sensing performances of the hydrogel strain sensor underwater (f) Relative resistance changes as a function of the applied strain. Resistance changes of hydrogels upon cyclic loading/unloading measurement within (g) various strains, (h) different tensile speed. (i) Response and recovery time of the sensor underwater. (j) The electromechanical stability of 200 cycles under 50% strain.

Real-Life Demonstration as Human Activity Monitoring Sensor

To take advantage of the excellent sensing performances and superior mechanical properties, the hydrogel was applied as a strain sensor to detect human physiological motions in real time. As shown in **Figure 2-10a**, the hydrogel was directly attached to different parts of a human body, and resistance signal was recorded synchronously. To evaluate the feasibility of the hydrogel sensor in human activities detection, the main joints including shoulder joint, elbow joint, hip joint, and knee joint of human body were taken as the monitoring points to verify the body postures while simulating walking and sitting. The output data in **Figure 2-10b** and **c** confirmed the possibility of distinguishing different body postures according to discrepant frequencies of the resistance change and waveforms of the signals. Furthermore, to prove the stability of the wearable device, electronic signals based on the bending movement of the wrist were recorded through multiple bending-releasing cycles of different angles (**Figure 2-10d**). The resistance signal changed and then restored to its original value when the wrist was bent and straightened, demonstrating high repeatability and stability at wrist bending angles of 30°, 60°, and 90°.

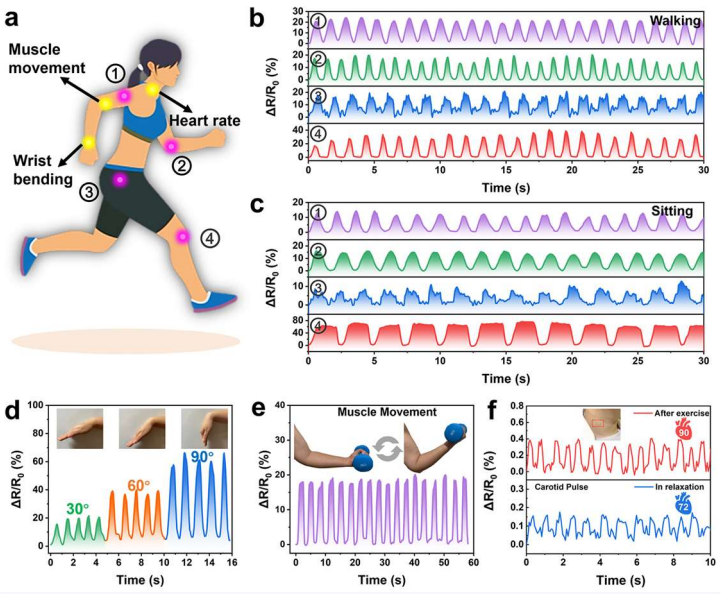

Figure 2-10. Human motion sensing in real-time by the hydrogel sensor. (a) Description of the detection locations in a body. Sensing signals of relative resistance variations on multiplex sites of shoulder, elbow, hip, and knee when (b) walking and (c) sitting. Real-time relative resistance of (d) wrist movements in different angles and (e) muscle movement. (f) Carotid pulse measured through time-dependent relative resistance change.

The stable and accurate signal detection of the hydrogel sensor ensure its suitability for applications in health management. In actual movement scenarios, it aided in life-quality improvement and disease prevention and by analyzing signals such as muscle movement and heart rate in real time. Thus, the resistance was examined in both large deformations and subtle movements, respectively (**Figure 2-10e** and **f**). Based on the adhesion behavior and stretchability, the sensor exhibited specific waveform of muscle movement by lifting dumbbells

even if the skin was sweaty. Moreover, the hydrogel device was attached to the neck to track carotid rates because of its sensitivity. The carotid pulse rate was 72 beats min^{-1} under relaxing circumstances but increased to 90 beats min^{-1} after exercise. This hydrogel sensor with adhesiveness and anti-swelling ability demonstrated reliable sensitivity and stability even when skin tended to become moist after exercise.

Underwater Physiological Signal Detection and Communication

As the continuous exploitation for marine resources, underwater communicator has garnered significant attention for its capacity to convey information in real-time and enhance the safety conditions of diving operators. Given the impressive combination of mechanical performances, anti-swelling abilities, adhesive behaviors, and electrical sensitivity of the hydrophobic hydrogel, it ensured the practical underwater sensing application. Morse codes were utilized to convey information for divers wearing the gel sensor. Here, the "dots" and "dashes" in coding principle were matched with the finger bending states (**Figure 2-11a**). Based on the step signals corresponding to finger bending angles in **Figure 2-11b**, it was determined that 30° (small) bending gesture and 60° (large) bending angle would represent "dots" and "dashes" in this information transmission mechanism underwater. As a validation, several

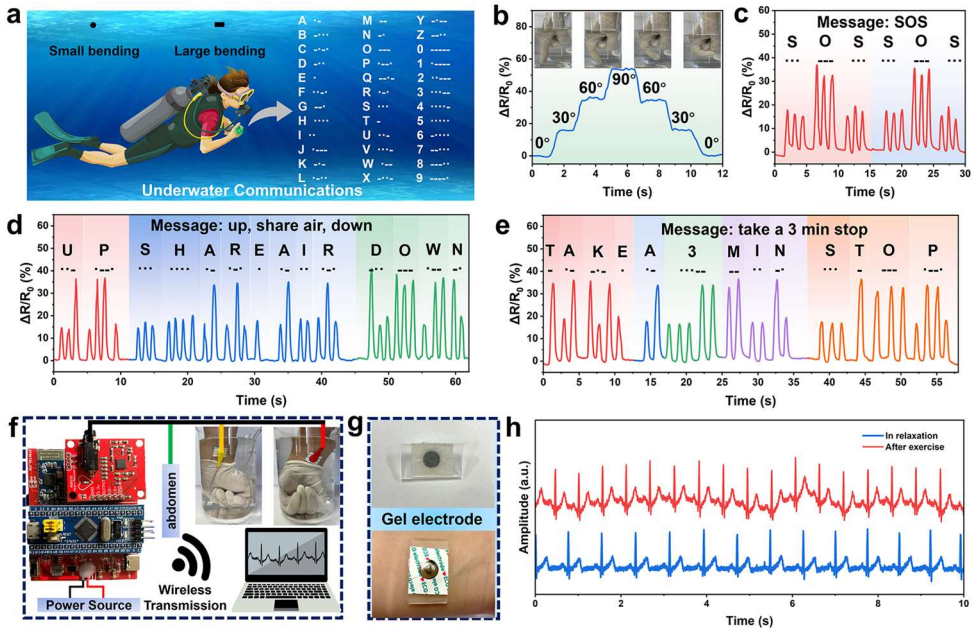

Figure 2-11. Applications on underwater physiological monitoring. (a) Schematic design of the underwater communicator based on Morse code. (b) Electrical response under different amplitudes through the finger bending in water. Practical underwater applications of recoding raw signals of (c) "SOS", (d) "up", "share air", and "down", (e) "take a 3 min stop". Wearable bioelectronic in aquatic environment (f) Diagrams of wireless ECG monitoring. (g) The assembled hydrogel electrode. (h) ECG signals captured by the hydrogel sensor.

demonstrations of relative resistance change in different underwater scenarios were carried out. In **Figure 2-11c**, the divers could send distress message of "SOS" by rhythmically bending fingers to request assistance when they encountered emergency situations. More meaningfully, during deep-water operations such as exploration, salvage and rescue, the underwater communicator enabled the subaquatic operators to request ascending, descending and oxygen supplement from the terrestrial personnel by sending a sequence of phrases (**Figure 2-11d**). The hydrogel sensor could also convey information in complex (sentences) form. As shown in **Figure 2-11e**, the diver could avoid "decompression sickness" symptom after operation via reminding their partners to follow slow ascent guidelines by sending a lengthy message of "take a 3 min stop". Therefore, the hydrogel sensor offered a viable means of underwater information transmission.

To further investigate the application of the hydrogel in aquatic environment, the wet-adhesive hydrogel was fabricated into a wireless electrocardiogram (ECG) device as a flexible electrode (**Figure 2-11f** and **g**). In heartbeats, the depolarization of myocardial cells caused minor electrical signal on the skin surface, which was received by the hydrogel electrode.[76] The analog signal was collected by the filtering and amplification processing in AD8232 module and then captured by the STM32 analog to digital converter. Due to the significant anti-swelling and self-adhesive properties, the hydrogel-based bioelectronic coating can exhibit stable ECG measurement. Hence, the hydrogel electrode demonstrated promising application in underwater ECG detection and wireless transmission in relaxing state and after exercise (**Figure 2-11h**). As demonstrated above, the hydrophobic hydrogel sensor showed great potential in constructing wearable bioelectronics in aquatic environment.

2-4. Conclusions

In summary, an electrostatic interacted hydrophobic association hydrogel with underwater adhesiveness was successfully developed by a facile "two-step" method. In this strategy, random polymerization between hydrophilic monomers HEAA and AA and hydrophobic monomers of MMA was crosslinked in the presence of cationic surfactant micelles CTAB, followed by the chain entanglement of chitosan in PANa soaking. Based on the synergistic

effect of dynamic chain entanglement and strong hydrogen bonding, the homogeneous network hydrophobic hydrogel exhibited excellent anti-swelling and water-retention capabilities and desirable mechanical properties, demonstrating promising prospect in both air and aquatic conditions. Furthermore, the well-ordered hydrophobic induced by electrostatic interactions, endowed the hydrogel with large stretchability (1500%), high toughness (2.4 MJ m^{-3}) and excellent elastic recovery behavior (elastic recovery ratio of 95%). Considering the superior functionalities mentioned above, as well as the excellent electromechanical performance, the hydrogel was appropriate for fabricating wearable sensors for human activity detection and health management. Additionally, thanks to the stable electrical sensitivity in aquatic environment (GF = 1.45), a transparency hydrogel-based device for underwater communication was assembled to transmit information through Morse codes. This optical transparency hydrogel sensor also showed significant application potential in wearable bioelectronics and bionic skins such as electrode in wireless ECG monitoring module. The research on multiple dynamic interacted hydrophobic association hydrogel paves the way for constructing intelligent soft materials applied in harsh environments.

2-5. References

1. H. C. Ates, P. Q. Nguyen, L. Gonzalez-Macia, E. Morales-Narváez, F. Güder, J. J. Collins and C. Dincer, *Nat. Rev. Mater.*, 2022, **7**, 887-907.

2. S. Kim, S. Baek, R. Sluyter, K. Konstantinov, J. H. Kim, S. Kim and Y. H. Kim, *EcoMat*, 2023, **5**, e12356.

3. Y. Song, J. Min, Y. Yu, H. Wang, Y. Yang, H. Zhang and W. Gao, *Sci. Adv.*, 2020, **6**, eaay9842.

4. S. Wang, Y. Gao, A. Wei, P. Xiao, Y. Liang, W. Lu, C. Chen, C. Zhang, G. Yang, H. Yao and T. Chen, *Nat. Commun.*, 2020, **11**, 4359.

5. J. Li, H. Jia, J. Zhou, X. Huang, L. Xu, S. Jia, Z. Gao, K. Yao, D. Li, B. Zhang, Y. Liu, Y. Huang, Y. Hu, G. Zhao, Z. Xu, J. Li, C. K. Yiu, Y. Gao, M. Wu, Y. Jiao, Q. Zhang, X. Tai, R. H. Chan, Y. Zhang, X. Ma and X. Yu, *Nat. Commun.*, 2023, **14**, 5009.

6. R. Tutika, A. B. M. T. Haque and M. D. Bartlett, *Commun. Mater.*, 2021, **2**, 64.

7. D. Yu, Y. Liao, Y. Song, S. Wang, H. Wan, Y. Zeng, T. Yin, W. Yang and Z. He, *Adv.*

Sci., 2020, **7**, 2000177.

8. T. Someya, T. Sekitani, S. Iba, Y. Kato, H. Kawaguchi and T. Sakurai, *Proc. Natl. Acad. Sci. U.S.A.*, 2004, **101**, 9966-9970.

9. F. Fu, J. Wang, H. Zeng and J. Yu, *ACS Mater. Lett.*, 2020, **2**, 1287-1301.

10. V. R. Feig, H. Tran, M. Lee and Z. Bao, *Nat. Commun.*, 2018, **9**, 2740.

11. T. Zhu, Y. Ni, G. M. Biesold, Y. Cheng, M. Ge, H. Li, J. Huang, Z. Lin and Y. Lai, *Chem. Soc. Rev.*, 2023, **52**, 473-509.

12. S. Wang, S. Li, H. Wang, H. Lu, M. Zhu, X.-E. Wu, H. Liang, X. Liang and Y. Zhang, *Adv. Funct. Mater.*, **33**, 2302687.

13. H. Fan, J. Wang and J. P. Gong, *Adv. Funct. Mater.*, 2021, **31**, 2009334.

14. J. Xu, R. Jin, X. Ren and G. Gao, *J. Mater. Chem. A*, 2019, **7**, 25441-25448.

15. Y. Luo, M. R. Abidian, J.-H. Ahn, D. Akinwande, A. M. Andrews, M. Antonietti, Z. Bao, M. Berggren, C. A. Berkey, C. J. Bettinger, J. Chen, P. Chen, W. Cheng, X. Cheng, S.-J. Choi, A. Chortos, C. Dagdeviren, R. H. Dauskardt, C.-a. Di, M. D. Dickey, X. Duan, A. Facchetti, Z. Fan, Y. Fang, J. Feng, X. Feng, H. Gao, W. Gao, X. Gong, C. F. Guo, X. Guo, M. C. Hartel, Z. He, J. S. Ho, Y. Hu, Q. Huang, Y. Huang, F. Huo, M. M. Hussain, A. Javey, U. Jeong, C. Jiang, X. Jiang, J. Kang, D. Karnaushenko, A. Khademhosseini, D.-H. Kim, I.-D. Kim, D. Kireev, L. Kong, C. Lee, N.-E. Lee, P. S. Lee, T.-W. Lee, F. Li, J. Li, C. Liang, C. T. Lim, Y. Lin, D. J. Lipomi, J. Liu, K. Liu, N. Liu, R. Liu, Y. Liu, Y. Liu, Z. Liu, Z. Liu, X. J. Loh, N. Lu, Z. Lv, S. Magdassi, G. G. Malliaras, N. Matsuhisa, A. Nathan, S. Niu, J. Pan, C. Pang, Q. Pei, H. Peng, D. Qi, H. Ren, J. A. Rogers, A. Rowe, O. G. Schmidt, T. Sekitani, D.-G. Seo, G. Shen, X. Sheng, Q. Shi, T. Someya, Y. Song, E. Stavrinidou, M. Su, X. Sun, K. Takei, X.-M. Tao, B. C. K. Tee, A. V.-Y. Thean, T. Q. Trung, C. Wan, H. Wang, J. Wang, M. Wang, S. Wang, T. Wang, Z. L. Wang, P. S. Weiss, H. Wen, S. Xu, T. Xu, H. Yan, X. Yan, H. Yang, L. Yang, S. Yang, L. Yin, C. Yu, G. Yu, J. Yu, S.-H. Yu, X. Yu, E. Zamburg, H. Zhang, X. Zhang, X. Zhang, X. Zhang, Y. Zhang, Y. Zhang, S. Zhao, X. Zhao, Y. Zheng, Y.-Q. Zheng, Z. Zheng, T. Zhou, B. Zhu, M. Zhu, R. Zhu, Y. Zhu, Y. Zhu, G. Zou and X. Chen, *ACS Nano*, 2023, **17**, 5211-5295.

16. J. Wei, P. Xiao and T. Chen, *Adv. Mater.*, 2023, **35**, 2211758.

17. J. Wei, Y. Zheng and T. Chen, *Mater. Horiz.*, 2021, **8**, 2761-2770.

18. H. Jiang, L. Duan, X. Ren and G. Gao, *Eur. Polym. J.*, 2019, **112**, 660-669.

19. H. Yang, H. Lu, Y. Miao, Y. Cong, Y. Ke, J. Wang, H. Yang and J. Fu, *Chem. Eng. J.*, 2022, **450**, 138346.

20. S. Wang, L. Wang, X. Qu, B. Lei, Y. Zhao, Q. Wang, W. Wang, J. Shao and X. Dong, *ACS Appl. Mater. Interfaces*, 2022, **14**, 50256-50265.

21. H. Guo, T. Nakajima, D. Hourdet, A. Marcellan, C. Creton, W. Hong, T. Kurokawa and J. P. Gong, *Adv. Mater.*, 2019, **31**, 1900702.

22. J. Wu, Z. Pan, Z.-Y. Zhao, M.-H. Wang, L. Dong, H.-L. Gao, C.-Y. Liu, P. Zhou, L. Chen, C.-J. Shi, Z.-Y. Zhang, C. Yang, S.-H. Yu and D.-H. Zou, *Adv. Mater.*, 2022, **34**, 2200115.

23. M. Khan, L. A. Shah, L. Ara, R. Ullah and H.-M. Yoo, *Chem. Mater.*, 2023, **35**, 5582-5592.

24. J. A. Long, B. M. Rankin and D. Ben-Amotz, *J. Am. Chem. Soc.*, 2015, **137**, 10809-10815.

25. M. Mihajlovic, H. M. Wyss and R. P. Sijbesma, *Macromolecules*, 2018, **51**, 4813-4820.

26. D. C. Tuncaboylu, M. Sahin, A. Argun, W. Oppermann and O. Okay, *Macromolecules*, 2012, **45**, 1991-2000.

27. C. Qi, Z. Dong, Y. Huang, J. Xu and C. Lei, *ACS Appl. Mater. Interfaces*, 2022, **14**, 30385-30397.

28. D. C. Tuncaboylu, M. Sari, W. Oppermann and O. Okay, *Macromolecules*, 2011, **44**, 4997-5005.

29. Y. Cai, K. Wan, Q. Chen, M. Hong, Z.-X. Zhou and H. Fu, *J. Mater. Chem. C*, 2023, DOI: 10.1039/D3TC01889J.

30. Y. Ni, X. Zang, J. Chen, T. Zhu, Y. Yang, J. Huang, W. Cai and Y. Lai, *Adv. Funct. Mater.*, 2023, **n/a**, 2301127.

31. G. Huang, Z. Tang, S. Peng, P. Zhang, T. Sun, W. Wei, L. Zeng, H. Guo, H. Guo and G. Meng, *Macromolecules*, 2022, **55**, 156-165.

32. Y. Zhao, S. Song, X. Ren, J. Zhang, Q. Lin and Y. Zhao, *Chem. Rev.*, 2022, **122**, 5604-5640.

33. G. Huang, H. Guo, Z. Tang, S. Peng, H. Liang, G. Meng and P. Zhang, *Chem. Mater.*,

2023, **35**, 5953-5962.

34. C. J. Demott, M. R. Jones, C. D. Chesney, D. J. Yeisley, R. A. Culibrk, M. S. Hahn and M. A. Grunlan, *Macromol. Biosci.*, 2022, **22**, 2200283.

35. H. Zhao, S. Hao, Q. Fu, X. Zhang, L. Meng, F. Xu and J. Yang, *Chem. Mater.*, 2022, **34**, 5258-5272.

36. X. Liu, Q. Zhang and G. Gao, *ACS Nano*, 2020, **14**, 13709-13717.

37. X. Dou, H. Wang, F. Yang, H. Shen, X. Wang and D. Wu, *Adv. Sci.*, 2023, **10**, 2206242.

38. P. Du, J. Wang, Y.-I. Hsu and H. Uyama, *ACS Appl. Mater. Interfaces*, 2023, **15**, 23711-23724.

39. L. Pan, G. Yu, D. Zhai, H. R. Lee, W. Zhao, N. Liu, H. Wang, B. C. K. Tee, Y. Shi, Y. Cui and Z. Bao, *Proc. Natl. Acad. Sci. U.S.A.*, 2012, **109**, 9287-9292.

40. Q. Zhang, X. Liu, J. Zhang, L. Duan and G. Gao, *J. Mater. Chem. A*, 2021, **9**, 22615-22625.

41. S. Zhang, Y. Li, H. Zhang, G. Wang, H. Wei, X. Zhang and N. Ma, *ACS Mater. Lett.*, 2021, **3**, 807-814.

42. M. N. V. R. Kumar, R. A. A. Muzzarelli, C. Muzzarelli, H. Sashiwa and A. J. Domb, *Chem. Rev.*, 2004, **104**, 6017-6084.

43. Y. Yang, X. Wang, F. Yang, L. Wang and D. Wu, *Adv. Mater.*, 2018, **30**, 1707071.

44. L. Xu, C. Wang, Y. Cui, A. Li, Y. Qiao and D. Qiu, *Sci. Adv.*, **5**, eaau3442.

45. D. Fu, G. Huang, Y. Xie, M. Zheng, J. Feng, K. Kan and J. Shen, *ACS Appl. Mater. Interfaces*, 2023, **15**, 11062-11075.

46. L. Zhou, Z. Wang, C. Wu, Y. Cong, R. Zhang and J. Fu, *ACS Appl. Mater. Interfaces*, 2020, **12**, 51969-51977.

47. C. Shao, M. Wang, L. Meng, H. Chang, B. Wang, F. Xu, J. Yang and P. Wan, *Chem. Mater.*, 2018, **30**, 3110-3121.

48. M. H. Lan, X. Guan, D. Y. Zhu, Z. P. Chen, T. Liu and Z. Tang, *ACS Appl. Mater. Interfaces*, 2023, **15**, 19447-19458.

49. Y. Gao, S. Gu, F. Jia, Q. Wang and G. Gao, *Chem. Eng. J.*, 2020, **398**, 125555.

50. C. Wang, J. Zhang, C. Niu, Q. Fu and L. Lu, *Chem. Mater.*, 2023, **35**, 1991-2005.

51. Z. Wang, J. Chen, L. Wang, G. Gao, Y. Zhou, R. Wang, T. Xu, J. Yin and J. Fu, *J. Mater. Chem. B*, 2019, **7**, 24-29.

52. S. Wang, J. Liu, L. Wang, H. Cai, Q. Wang, W. Wang, J. Shao and X. Dong, *Adv. Mater. Technol.*, 2023, **8**, 2201477.

53. M. Zhao, W. Zhang, D. Wang, P. Sun, Y. Tao, L. Xu and L. Shi, *Adv. Mater. Interfaces*, 2022, **9**, 2101786.

54. R. Zhang, A. Yang, Y. Yang, Y. Zhu, Y. Song, Y. Li and J. Li, *Int. J. Biol. Macromol.*, 2023, **245**, 125469.

55. S. He, B. Guo, X. Sun, M. Shi, H. Zhang, F. Yao, H. Sun and J. Li, *ACS Appl. Mater. Interfaces*, 2022, **14**, 45869-45879.

56. L. Xiang, L. Gong, J. Zhang, L. Zhang, W. Hu, W. Wang, Q. Lu and H. Zeng, *Phys. Chem. Chem. Phys.*, 2019, **21**, 20571-20581.

57. C. Cui, C. Shao, L. Meng and J. Yang, *ACS Appl. Mater. Interfaces*, 2019, **11**, 39228-39237.

58. J. Chen, Q. Peng, T. Thundat and H. Zeng, *Chem. Mater.*, 2019, **31**, 4553-4563.

59. M. Mihajlovic, M. Staropoli, M.-S. Appavou, H. M. Wyss, W. Pyckhout-Hintzen and R. P. Sijbesma, *Macromolecules*, 2017, **50**, 3333-3346.

60. T. D. A. Senra, A. Khoukh and J. Desbrières, *Carbohydr. Polym.*, 2017, **156**, 182-192.

61. W. Kong, C. Wang, C. Jia, Y. Kuang, G. Pastel, C. Chen, G. Chen, S. He, H. Huang, J. Zhang, S. Wang and L. Hu, *Adv. Mater.*, 2018, **30**, 1801934.

62. Z. Sun, C. Dong, B. Chen, W. Li, H. Hu, J. Zhou, C. Li and Z. Huang, *Small*, 2023, **19**, 2303612.

63. M. Cao, B.-W. Liu, L. Zhang, Z.-C. Peng, Y.-Y. Zhang, H. Wang, H.-B. Zhao and Y.-Z. Wang, *Compos. B Eng.*, 2021, **225**, 109309.

64. S. Aleid, M. Wu, R. Li, W. Wang, C. Zhang, L. Zhang and P. Wang, *ACS Mater. Lett.*, 2022, **4**, 511-520.

65. J. Li, J. Li, Y. Tang, Z. Liu, Z. Zhang, H. Wu, B. Shen, M. Su, M. Liu and F. Li, *ACS Nano*, 2023, **17**, 5129-5139.

66. Z. Wang, J. Chen, Y. Cong, H. Zhang, T. Xu, L. Nie and J. Fu, *Chem. Mater.*, 2018, **30**,

8062-8069.

67. K. Zhang, X. Zhang, Y.-j. Fang and J. Cai, *Acta Polym. Sin.*, 2023, **54**, 731-740.

68. K. Shen, K. Xu, M. Zhang, J. Yu, Y. Yang, X. Zhao, Q. Zhang, Y. Wu, Y. Zhang and Y. Cheng, *Chem. Eng. J.*, 2023, **451**, 138525.

69. Y. Gao, S. Gu, L. Duan, Y. Wang and G. Gao, *Soft Matter*, 2019, **15**, 3897-3905.

70. J. Chen, R. An, L. Han, X. Wang, Y. Zhang, L. Shi and R. Ran, *Mater. Sci. Eng. C*, 2019, **99**, 460-467.

71. Q. Ling, W. Liu, J. Liu, L. Zhao, Z. Ren and H. Gu, *ACS Appl. Mater. Interfaces*, 2022, **14**, 24741-24754.

72. M. Pan, T. Shui, Z. Zhao, M. Li, H. Fan, J. Wu and H. Zeng, *Chem. Mater.*, 2023, **35**, 4998-5008.

73. M. Pi, S. Qin, S. Wen, Z. Wang, X. Wang, M. Li, H. Lu, Q. Meng, W. Cui and R. Ran, *Adv. Funct. Mater.*, 2023, **33**, 2210188.

74. Y. Zhao, F. Wang, J. Liu, D. Gan, B. Lei, J. Shao, W. Wang, Q. Wang and X. Dong, *ACS Appl. Mater. Interfaces*, 2023, **15**, 28664-28674.

75. Z. Ma, C. Bourquard, Q. Gao, S. Jiang, T. De Iure-Grimmel, R. Huo, X. Li, Z. He, Z. Yang, G. Yang, Y. Wang, E. Lam, Z.-h. Gao, O. Supponen and J. Li, *Science*, 2022, **377**, 751-755.

76. F. Chen, Q. Zhuang, Y. Ding, C. Zhang, X. Song, Z. Chen, Y. Zhang, Q. Mei, X. Zhao, Q. Huang and Z. Zheng, *Adv. Mater.*, 2023, **35**, 2305630.

Chapter 3
Organohydrogel Incorporated with Quaternized Chitosan (QCS) and Ionic Liquid (IL)-Graphene Nanosheets for Flexible Sensing

3-1. Introduction

On account of the growing prevalence of wearable devices, interactive electronic epidermis capable of realizing multimodal sensing are gaining apparent attention in contemporary research.[1-3] In particular, conductive hydrogel-based materials have the potential to serve as mainstays in soft robotics,[4] touch panels,[5] implantable medical components,[6] portable energy storage devices,[7] *etc.*, due to their favorable responsiveness, epidermal compliance, and adjustable functionality.[8-10] Benefiting from the distinct three-dimensional (3D) hydrated architectures, the hydrogels are fascinating platforms for facile modification by incorporation of functional additives, thereby ensuring that the flexible sensor possesses significant electrical and mechanical properties alongside other functions, such as self-healing, self-adhesion, and photothermal conversion capability.[8, 11-14] The most introduced conductive components to date such as conductive polymers (*e.g.*, pyrrole, polyaniline),[15, 16] metal ions,[17] metallic nanowires,[18] and carbon nanomaterials,[8, 19, 20] particularly graphene hold great promise for formulating high-performance hydrogels, substantially improving their conductivity and mechanical properties.[20] Notably, the inferior dispersibility of graphene in common solvents results in its tendency to agglomerate within the 3D network matrices, which may fall short of meeting the practical needs.[21] Limited approach to assist in exfoliation and long-term stable dispersion of graphene nanosheets in different solvents has already been a major obstacle to prepare homogenous conductive hydrogels with excellent application stability.[22, 23]

Ionic liquids (ILs), a sustainable molten salt composed of conjugated anion-cation species, seem well positioned to address this challenge because of the inherent non-flammability and extensive solubility.[24] The IL can chemically tailor the graphene edges, resulting in a significant dispersion capability within diverse solvents such as H_2O, DMF and DMSO *etc.* Compared to the conventional dispersion methods, the ILs exfoliation is superior in maintaining graphene's structural integrity, ease of operation, environmental friendliness, and prevention of reaggregation, making it long-term stable and suitable for various applications.[25] For instance,

Xie et al. prepared a hydrophobic associated hydrogel with super toughness and excellent electrical conductivity, by the reinforcement of silica amino spheres and effectively dispersed graphene using ionic liquids.[26] Particularly, imidazolium ILs satisfactorily impede the aggregation of the nanofillers by cation–π interactions through shielding the charged layers on the colloidal surface.[27, 28] Although the "cation-π interactions" is one of the strongest noncovalent interactions, covalent attachment from ILs should be more efficient for exfoliation and stable dispersions of graphene derivatives.[21] On the one hand, the surfaces of graphene oxide (GO) contain numerous and reactive epoxy groups, which lead to high reactivity yet easy reagglomeration.[29] But the epoxy groups can be grafted by the amine groups in amine-terminated ionic liquids (ILs) via nucleophilic ring-opening reactions, thereby covalently dispersing the chemically-converted graphene sheets.[21] On the other hand, according to an oversimplified design, vinyl groups can present within the imidazole cation by a mild alkylation reaction.[30] In this regard, the electrostatically dispersed graphene is capable of being integrated into the hydrogel network as multifunctional monomers to facilitate bonding and crosslinking. Therefore, designing polymerizable IL-GO hybrid materials along with proposing their versatile roles in hydrogels remains scarce yet promising for cutting-edge flexible electronic applications.[31-33] Although previous literature has reported the addition of graphene derivatives as reinforcement or conductive fillers for hydrogels, it was overlooked their function as a two-dimensional surfactant.[34] The author believe that the imidazolium cation at the edge of IL-GO sheets contributes to their hydrophilicity, while the graphene domain ensures the hydrophobicity, which further self-assembles into micelles to stabilize the hydrophobic fragment. In addition, wearable hydrogel devices are inevitably deteriorated in extreme environmental conditions.[35-39] Although the IL is a candidate solvent in achieving low-temperature tolerant hydrogels, it depresses the transfer of carriers when totally replacing water.[40] Similarly, adding inorganic salts into hydrogel are feasible to decrease its freezing point, but it disrupts mechanical properties.[41, 42] Another strategy to construct organohydrogels with superior anti-freezing and moisturizing properties is addition of organic solvents.[33, 38, 43-45] Dimethyl sulfoxide (DMSO) possesses intrinsically high polarity and forms abundant hydrogen bonding with water

molecules.[46] Accordingly, it meets the practicability of freezing and dehydration resistance for flexible electronics by lowering the freezing point and vapor pressure.[47]

Herein, the author proposes the utilization of IL-GO hybrids as polymerizable monomers instead of individual dispersions to develop a versatile electron-conducting organohydrogel in DMSO/H_2O binary solvent system, with the aim of achieving multiple objectives in one endeavor: (i) the covalently-converted graphene nanosheets can be homogenously dispersed in various solvent without assistance of surfactant stabilizers; ii) the vinyl groups near imidazolium rings achieving the copolymerization within hydrogel networks; and iii) the amphiphilic structure of the IL-GO as two-dimensional surfactants enabling the stabilization the hydrophobic fragments. As a proof of concept, an all-climate transducer is constructed by integrating interpenetrating structures of quaternized chitosan (QCS), alongside homopolymeric 2-(dimethylamino)ethyl methacrylate (DMAEMA), 2-acrylamido-2-methyl-1-propanesulfonic acid (AMPS) and 2-phenoxyethyl acrylate (PEA). The electrostatic and hydrophobic interactions ensure the favorable mechanical performance, and protect the universal adhesive interface from water inflow.[48] The electronic skin can not only accurately detect physiological activities and recognize handwriting but also reliably track temperature change, attributed to the extreme environmental tolerance and differentiated carrier mobility at fluctuating temperatures.

3-2. Experimental Section

Materials

The chitosan quaternary ammonium salt (QCS) was purchased from by Shanghai Macklin Chemistry Co., Ltd. (Shanghai, China). The ammonium persulfate (APS) and 2-acrylamido-2-methylpropanesulfonic acid (AMPS) were obtained from Sigma-Aldrich (St. Louis, USA). The dimethyl sulfoxide (DMSO), dimethylformamide (DMF), ethanol, ammonia solution, methylene blue, ammonium persulfate (APS), 2-(dimethylamino)ethyl methacrylate (DMAEMA), and acrylamide (AM) were provided by Fujifilm Wako Pure Chemical Corporation (Osaka, Japan). The *N*, *N*'-methylenebis(acrylamide) (BIS), graphene oxide (GO), hydrazine, 3-bromopropylamine hydrobromide, 2-phenoxyethyl acrylate (PEA), and 1-

vinylimidazole were purchased from Tokyo Chemical Industry Co., Ltd. (Tokyo, Japan). The solvent of deuterium oxide (D_2O) for ^1H nuclear magnetic resonance (NMR) spectroscopy was offered by Fujifilm Wako Pure Chemical Corporation (Osaka, Japan).

Synthesis of the 1-vinyl-3-(3-aminopropyl)-imidazolium bromide ionic liquid

The procedure was according to a modified method based on previous works.[21, 49] Specifically, a mixture of 1-vinylimidazole (5 mmol) and 3-bromopropylamine hydrobromide (5 mmol) were added into 12.5 mL ethanol, forming a homogeneously colorless solution which was refluxed under nitrogen for 24 h at 90℃. The crude product was purified by precipitation with a mixture solution of ethyl acetate and ethanol. Finally, the amino-terminated ionic liquid was obtained after evaporating the solvents in vacuo. The amino-terminated ionic liquid was denoted as IL. The synthesis schematic and corresponding characterization are shown in **Figure 3-1**. The summarized ^1H NMR (δ, D_2O) data are listed as following: 9.00 (s, 1H), 7.68 (s, 1H), 7.51 (s, 1H), 7.01 (m, 1H), 5.68 (d, 1H), 5.31 (d, 1H), 4.25 (t, 2H), 2.96 (t, 2H), 2.19 (m, 2H).

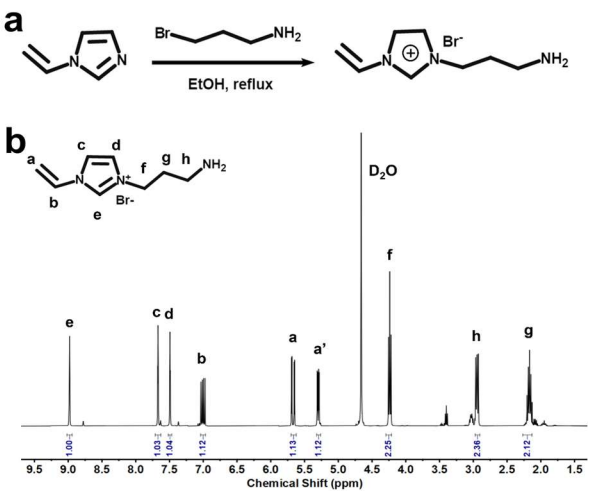

Figure 3-1. (a) Synthetic procedure of IL. (b) ^1H NMR spectra of IL in D_2O.

Synthesis of the covalently converted IL-GO

The IL-GO hybrid nanosheet was prepared by an epoxide ring-opening reaction between the amino-terminated IL and GO.[21] In a typical procedure, IL (10 mg) was added into the mixture containing 10mL of GO homogeneous and transparent dispersion in water (0.5mg mL^{-1}). After that process, the salt effect of the GO sheets occurred within the presence of IL. Notably, to ensure the grafting efficiency, excess amount of IL was used to functionalize the GO nanosheets. Then, KOH (10 mg) was added into the above turbid mixture and then the mixture was subjected to ultrsonication for 30 minutes to obtain a homogeneous dispersing system. The suspension was vigorously stirred at 80 °C for 24 h by reflux. Finally, the IL-GO hybrid

nanomaterial was obtained by centrifugation, washed several times with deionized water, and then dried.

Fabrication of the organohydrogel

The interpenetrating organhydrogels were fabricated via a one-pot free radical polymerization. Typically, 0.3 g of QCS, 2.0 g of DMAEMA, 1.5 g of AMPS, 1.25 g of PEA, 0.75 of IL-GO, and 20 mg of BIS were mixed in 10 mL of aqueous solution containing 50 wt% DMSO and homogeneously stirred, followed by degassing with ultrasonic cleaning for 10 min and storing in a refrigerator for 30 min. After ultrasonic radiation by Violamo ultrasonic homogenizer (Sonicstar 85, Japan) for 3 min, the 36 mg of APS was mixed in the above mentioned precursor solution for rapid dispersion, and sequentially the mixture was fast poured into home-made polytetrafluoroethylene (PTFE) molds.[50] After polymerization at room temperature for about 10 min to achieve $PA_{1.5}DG_{0.75}P_{1.25}/Q$ orgnaohydrogels. The collected composite organohydrogels were flushed using deionized water. Besides, a sample precursor without any ultrasonic radiation process was also prepared for comparision. To obtain the optimal concentration of AMPS and IL-GO in the organohydrogels, a similar method was utilized for control. The organohydrogels can be generally dentoed as $PA_xDG_yP_z/Q$ (the values of x = 0, 0.5, 1, 1.5 and 2.0; y = 0.25, 0.50, 0.75 and 1.0; z = 0 and 1.25 were investigated). The author also prepared the mixture sample using AM to replace DMAEMA to prove the quick free radical production from the reaction between the tertiary amine group in DMAEMA and the persulfate group in APS, and which was denoted as $PA_{1.5}AG_{0.75}P_{1.25}/Q$.

Characterization

Raman spectroscope (Raman, Horiba Scientific LabRAM HR evolution, laser wavelength = 514 nm) was used to analyze the material composition. X-ray photoelectron spectroscopy (XPS, ThermoFischer ESCALAB Xi+, E = 1486.6 eV, USA) were used to confirm the chemical compositions and structures of the GO and IL-GO. The Talos F200S G2 transmission electron microscopy (TEM) equipped with energy dispersive X-ray spectroscopy showed the EDS high-angle annular dark field (HAADF) scanning TEM images and corresponding EDS elemental mapping images of the prepared IL-GO. The heights and morphologies of the IL-GO was

characterized using SPI3800N/SPA-400 atomic force microscope (AFM). The X-ray diffraction (XRD) results for GO and IL-GO were acquired using SmartLab (Rigaku Corporation) with a scanning speed of 5° min^{-1} over the 2θ range of 5–70°. Attenuated total reflection Fourier transform infrared (ATR-FTIR) spectra over the wavenumbers ranging from 4000 to 500 cm^{-1} for the raw materials and organohydrogels were recorded at room temperature with a Nicolet iS5 spectrometer (Thermo Fisher Scientific).

Tensile tests and rheology analysis

The mechanical properties of the organohydrogel samples were tested using a universal material testing machine (Shimadzu AGS-X, Shimadzu Corporation, Japan) with a 100 N load cell at room temperature. The samples were cut into rectangular samples with 2 mm thickness, 10 mm inner width, and 20 mm gauge length, and the distance of the clamps was set as 10 mm for all the tensile tests. The stretching rate was set at 100 mm/min for strectching test and loading-unloading cyclic tests. The tensile strain (ε) was defined as the change in the length (l) relative to the gauge length(l_0) of the each specimen. The tensile stress σ was determined by the ratio between the load force (F) and the cross-sectional area (S). The elastic modulus (E) was calculated from the slope in the initial linear region in the range 5–15% of the stress. The toughness (U_T) was calucated by the equation as follow:[51]

$$U_T = \int \sigma d\varepsilon \tag{3-1}$$

For the loading-unloading curves for various strains, the dissipation energy (DE) and dissipation coefficient (DC) were calculated with the following formulas:[52]

$$\mathrm{DE} = \int_{loading} \sigma \, d\varepsilon - \int_{unloading} \sigma \, d\varepsilon \tag{3-2}$$

$$\mathrm{DC} = 100\% \times \left[\left(\int_{loading} \sigma \, d\varepsilon - \int_{unloading} \sigma \, d\varepsilon \right) / \int_{loading} \sigma \, d\varepsilon \right] \tag{3-3}$$

The organohydrogels were placed at the bottom of the parallel plates to investigate their viscoelastic behaviors using HAAKE RheoStress 6000 (Thermo Fisher Scientific). The oscillation frequency sweep in the linear viscoelastic region was conducted from 0.1 to 100 Hz at 0.1% strain under 25 °C. And the variations of the storage modulus and loss modulus were

measured under the oscillation strain of 0.1 to 1000%. The step-strain measurement of the organohydrogel was conducted by switching between 1% and 500% strain.

Adhesion test

The Shimadzu AGS-X universal test machine equipped with a 10 N load cell and at 50 mm min^{-1} stretching rate was used to measure the adhesion performance toward diverse substrates of metal, porcine skin (excess superficial fat), wood, glass, rubber and PTFE until the organohydrogel interfaces were completely separated. The specimen with a bonded area of 10 mm × 10 mm was sandwiched in the surfaces attached to the plates. Subsequently, the bonded substrate was pressed with a weight of 250 g for 10 min. The maximum load was the adhesion strength through the adhesion force-displacement curves. Wet adhesive strength was collected by sprinkling water at the contact interface between the substrate and the organohydrogel adhesive.

Anti-freezing and anti-drying properties of the organohydrogel

The adhesive behavior, mechanical, electrical, and sensing properties of the organohydrogels were measured after being stored in a certain environment to evaluate their freezing and drying resistance properties. First of all, the organohydrogel sheet and the comparising hydrogel sheet were placed in a refrigerator at –20 °C and in an oven at 50 °C for 24 h. Subsequently, the samples were tested for adhesive behavior, and mechanical properties immediately. In order to keep the consistent test conditions, and avoid the influence of temperature on conductivity, the electrical conductivity and strain sensitivity of the samples after freezing and hotting treatment can be tested when they reached to room temperature. In addition, the antifreezing properties were particularly analyzed by differential scanning calorimetry (DSC, NEXTA DSC200). The temperature decreased from 80 to –80 °C at a cooling speed of 10 °C min^{-1}.

Electrical conductivity measurement

The electrical conductivity of the organohydrogel with 2 mm thickness, 10 mm width, and 20 mm length was obtained by recording the resistance signals in the frequency range of 0.1–10^6 Hz and voltage of 1 V using an inductance, capacitance, and resistance (LCR) meter

(TH2830, Changzhou Tonghui Electronic Co. Ltd.). The conductivity calculation formula is as expressed[53]:

$$\sigma = \frac{L}{RS} \tag{3-4}$$

where L is the length between adjacent electrodes, and R and S represent the resistance and cross-section area of the organohydrogels, respectively.

Sensing performance

Copper wires were connected to both sides of the strain sensors with a size of 2mm × 10 mm × 20 mm. The signal was transmitted into the relative resistance change under different strains as well as varied frequencies, which was measured by an using an inductance, capacitance, and resistance (LCR) meter (TH2830, Changzhou Tonghui Electronic Co. Ltd., China) in real time. Moreover, the oganohydrogel strain sensor was attached to the human body to monitor the physiological signals. The relative resistance change was computed as the following formula[54]:

$$\frac{\Delta R}{R_0} = \frac{|R - R_0|}{R_0} \times 100\% \tag{3-5}$$

where R and R_0 represented the resistance caused by organohydrogel deformation and the initial resistance of the organohydrogel, respectively.

The electrical sensitivity was denoted as gauge factor (GF), which was calculated by the equation:[30]

$$\mathrm{GF} = \frac{\Delta R}{R_0 \varepsilon} \tag{3-6}$$

where ε was the corresponding strain change.

The wireless electrocardiography (ECG) monitoring was realized by assembling the organohydrogel to an electrode into the AD8232 module.

Assessment of the thermal-sensitive performance of the sensor

The organohydrogel (2 mm × 10 mm × 20 mm) were connected to LCR meter by copper

wires and placed in a heating-cooling plate (SCP, AS ONE). The temperature sensitivity test was performed by changing the temperature of heating-cooling plate, and the experimental data were recorded through LCR meter.[55, 56] The resistance temperature coefficient (TCR) was used to evaluate the sensitivity of thermal response by recording the resistance variations of the organohydrogel. which is defined as the ratio of relative resistance change ($\Delta R/R_0$) to temperature change (ΔT).[36, 57] And the value of TCR was calculated by the following equation:

$$\mathrm{TCR} = \frac{\left(\frac{\Delta R}{R_0}\right)}{\Delta T} = \frac{\left(\frac{R_T - R_0}{R_0}\right)}{\Delta T} \tag{3-7}$$

where R_T, R_0 and ΔT are the resistance of the organohydrogel after heating/cooling to a certain temperature, the initial resistance, and temperature change, respectively.

3-3. Results and discussion

Preparation of IL-GO

The preparation process of functionalized IL-covalently-converted graphene nanosheets and IL-GO assisted organohydrogels are schematically illustrated in **Figure 3-2a**. The synthesized IL as auxiliary reagents were applied to exfoliate GO according to an epoxide ring-opening reaction, thus forming the covalently-converted graphene.[21] The IL-GO hybrids showed stable dispersibility in representative water, dimethylformamide (DMF) and DMSO solvent for 24 h.

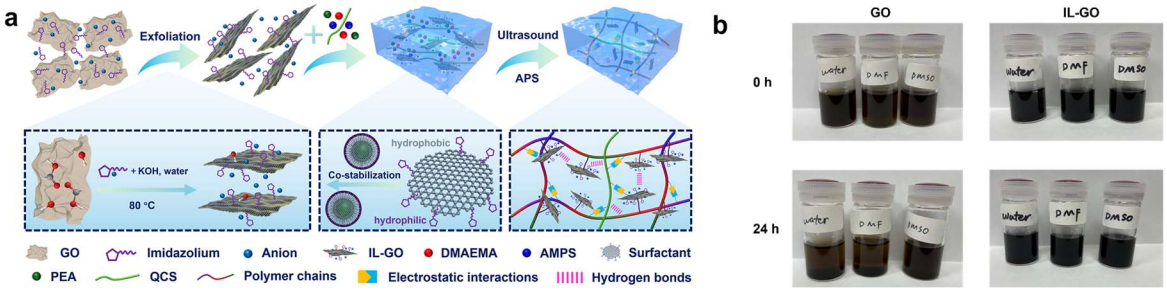

Figure 3-2. (a) Schematic preparation process and the corresponding interactions of the IL-GO and $PA_xDG_yP_z$/Q organohydrogel; Comparison disperse stability for GO (left) and IL-GO (right) in solution of water, DMF, and DMSO for 0 and 24 h.

The morphology of IL-GO nanohybrids was characterized by atomic force microscopy (AFM) and transmission electron microscopy (TEM). As illustrated in **Figure 3-3a**, the IL-GO hybrid exhibited an intact sheet-like structure without obvious aggregation and its average

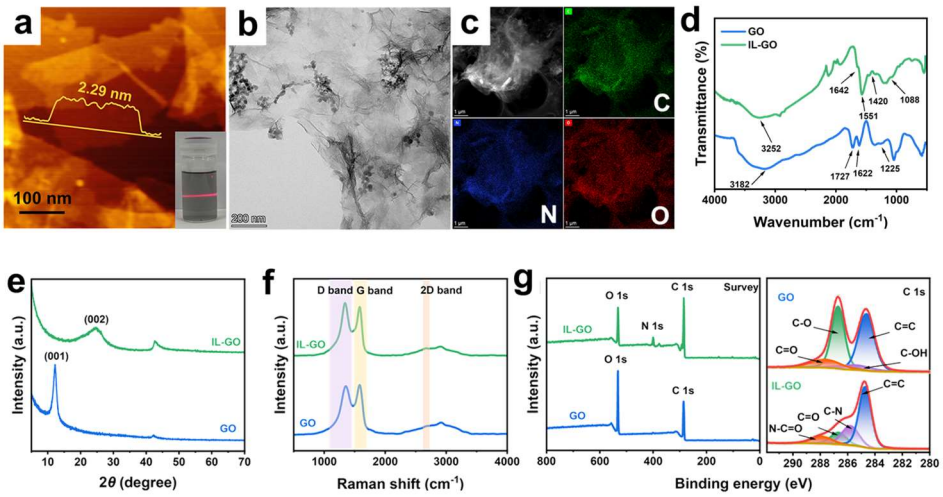

Figure 3-3. (a, b, and c) AFM (inset is the Tyndall effect of the IL-GO dispersion), and TEM images with corresponding elemental mapping by energy dispersive X-ray spectroscopy (EDS) of the IL-GO. (d, e, f) Comparison ATR-FTIR, XRD and Raman spectrum of the pristine GO and IL-GO. (g) Survey XPS spectra of the GO and IL-GO and inset is the high-resolution data of the C 1s spectrum of GO and IL-GO.

thickness was 2.29 nm according to the height profile, indicating exfoliated by grafting IL. The TEM images in **Figure 3-3b** showed transparent structures of the well-dispersed nanoflakes, and its corresponding elemental distribution (**Figure 3-3c**) demonstrated the existence of abundant nitrogen elements in the surface, confirming the presence of IL. These results were verified by the attenuated total reflection-Fourier transform infrared (ATR-FTIR) spectroscopy (**Figure 3-3d**), where the ν(N–C=O) at 1642 cm^{-1} indicating the successful amide-carboxyl reaction.[58] Notably, the distance between IL-GO nanoflakes were a bit wider as estimated. So, X-ray diffraction (XRD) was further employed to compare the exfoliating condition of pristine GO and IL-GO. In **Figure 3-3e**, a characteristic diffraction peak at 10.5° corresponding to the (001) plane with interlayer spacing of 0.84 nm can be observed in GO because of the oxygen-containing groups.[59] However, a broad diffraction peak (002) at 24.0° presented in IL-GO, which represented the disordered structure caused by IL exfoliation.[25] Meanwhile, the GO was grafting attached by the IL, effectively prohibiting reagglomeration and irregular stacking of graphene layers. The Raman spectra in **Figure 3-3f** demonstrated the typical graphene structure via characteristic G, D, and 2D peaks at approximately 1582, 1354, and 2700 cm^{-1}, respectively. The weak intensity of 2D band may be attributed to introduction of crystal defects and surface adsorbates from IL coupling.[60] Notably, the I_D/I_G (the intensity ratio of D peak to G peak) of IL-GO increased compared to pristine GO due to the structural distortions during reaction.[25]

The author further evaluated the valence states using X-ray photoelectron spectroscopy (XPS). **Figure 3-3g** illustrated a nitrogen peak at 401.7 eV, indicating the introduction of amino groups and aromatic rings.[61] The elemental ratio of C to O intensely decreased. Moreover, the C 1s spectrum of IL-GO displayed decreased C=O (286.4 eV) groups but newly generated C–N (285.5 eV) and N–C=O (288.1 eV) bonds, representing the existence of imidazolium ring alongside covalent bound of amino groups to epoxy groups and carboxyl groups via epoxide ring-opening reaction and acylation reaction, respectively.[21]

Preparation of $PA_xDG_yP_z$/Q organohydrogel

The feedstock containing QCS, monomers including DMAEMA, AMPS, PEA and IL-GO, as well as cross-linker and initiator was poured into a home-made mold to obtain the interpenetrating network $PA_xDG_yP_z$/Q organohydrogel via ultrasonic induced gelation. The ultrasonic operation supplied sufficient energy and increased system temperature, correspondingly triggered the rapid polymerization of the organohydrogel in the presence of DMAEMA.[50, 62] The tertiary amine groups in DMAEMA reacted with persulfate to accelerate the free radical production (**Figure 3-4**).[50] The ultrasonic operation supplied sufficient energy and increased system temperature, correspondingly triggered the rapid polymerization (10 min) of the organohydrogel in the presence of DMAEMA.

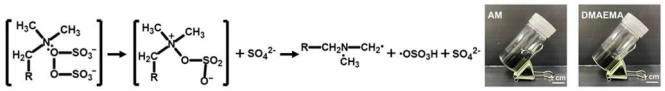

Figure 3-4. Formula of the quick free radical production and images comparing the rapid polymerized organohydrogels.

The chemical composition of the gels was conducted by ATR-FTIR (**Figure 3-5**). The characteristic peaks at around 3285 cm^{-1}, also 2960 and 2870 cm^{-1} were attributed to the $\nu(-CH_3)$ and $\nu(-CO-NH_2)$, respectively, confirming the copolymerization of different networks.[13] For the gels of $PA_{1.5}DG_{0.75}$/Q and $PA_{1.5}DG_{0.75}P_{1.25}$/Q, emerging peaks at 1450, 1550 and 1600 cm^{-1} indicated the ν(aromatic C=C) originated from imidazolium rings or PEA segments.[25] Besides, the absence of characteristic peak at 952 cm^{-1} identified the S=O groups in DMSO.[13]

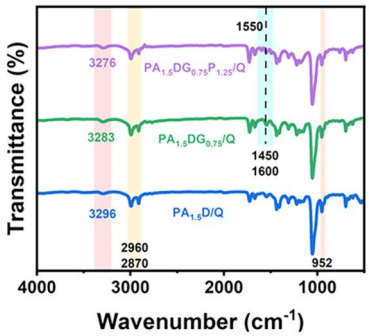

Figure 3-5. The ATR-FTIR spectra of the $PA_{1.5}$D/Q, $PA_{1.5}DG_{0.75}$/Q and $PA_{1.5}DG_{0.75}P_{1.25}$/Q organohydrogels, respectively.

Mechanical properties of the organohydrogels

Organohydrogels with outstanding mechanical properties are preferable in fabricating flexible sensors. Here, the mechanical performance of the prepared organohydrogels with different addition of AMPS and IL-GO were conducted by universal stress-strain tests. With the increase of AMPS, the fracture stress of the organohydrogels increased while the elongation tensile first increased then decreased after AMPS exceeding 1.5 g (**Figure 3-6a**). Therefore,

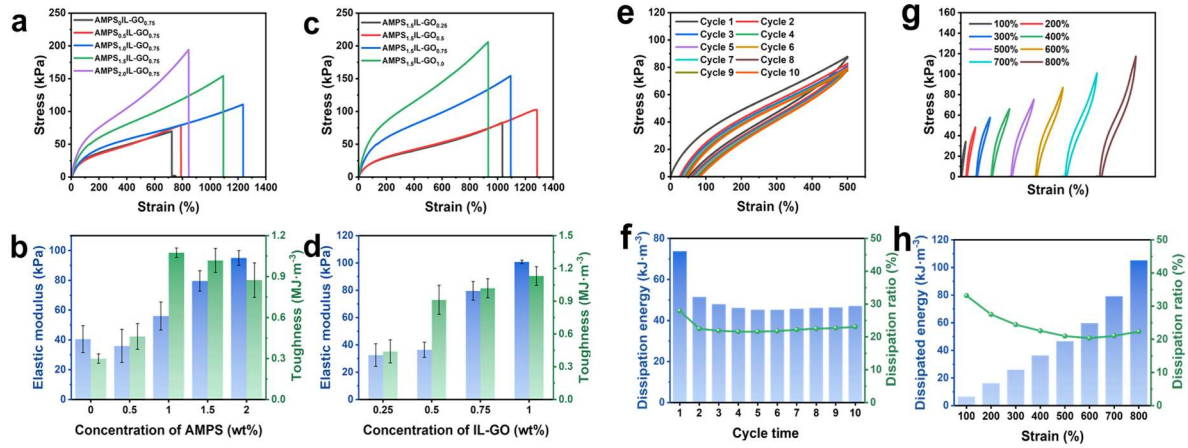

Figure 3-6. (a, b) Typical strain-stress curves of organohydrogels incorporated with different contents of AMPS and the corresponding calculated elastic modulus and toughness. (c, d) Typical strain-stress curves of organohydrogels incorporated with different contents of IL-GO and the corresponding Young's modulus and toughness. (e, f) Successive loading-unloading stress-strain curves at a fixed strain of 500% for 10 cycles and the dissipated energy and dissipation ratio of the $PA_{1.5}DG_{0.75}P_{1.25}$/Q organohydrogel under 500% strain for 10 cycles. (g, h) Successive loading-unloading stress-strain curves of strain from 100% to 800% and the dissipated energy and dissipation ratio of the $PA_{1.5}DG_{0.75}P_{1.25}$/Q organohydrogel under the strain from 100 to 800%.

considering the stretchability and robustness, the specimen with 1.5 g of AMPS was choose, because of its skin-like elastic modulus of 79.6 kPa and high toughness of 1.02 MJ m^{-3}. Similarly, the variation of fracture stress and tensile strength with increasing concentration of IL-GO exhibited a consistent trend when the content of AMPS was controlled (**Figure 3-6c** and **d**). The enhanced mechanical property was possibly attributed to the massive hydrogen bonding and IL-GO sliding effects.[63, 64] By allowing relative sliding between nanolayers, external stresses can be dispersed, thereby enhancing the strength and toughness of the organohydrogel. In addition, the sliding effect can also prevent crack propagation during deformation to improve the fracture resistance.[65] However, excessive AMPS and IL-GO may increase the crosslinking density, thus limiting the chain movement.[39] Furthermore, tensile loading-unloading tests were performed to explore their self-recovery ability (**Figure 3-6e–h**). The organohydrogel was

stretched to a fixed strain of 500% and released without any residence for 10 cycles. Except the first cycle, the hysteresis loop almost overlapped in the subsequent successive cycles, revealing fast recoverability and resilience. The consecutive cycling curves under different strains displayed small residual deformation and low energy dissipation, which can be attributed to the incomplete chain fracture and reconstruction of dynamic bonds.[41] Ensuring proper dispersion, 0.75g of IL-GO exerted the optimal effect on mechanical performance.

Besides, oscillatory rheological testing was further employed to investigate the viscoelastic behavior (**Figure 3-7a–c**). The storage modulus (G') and loss modulus (G'') both increased as the angular frequency, implying typical elastic solid-like behavior when incorporating IL-GO into the matrix.[20] The G' and G'' showed little change in low-range strain, but intersected when subjected strain above 300%, which signified that the abundant dynamic physical interactions can effectively resist deformation.[11] Furthermore, the organohydrogel emerged in periodic transmission between gel and sol-gel states since it was alternately applied with 1% and 500% amplitudes for 100 s, demonstrating significant reversible recovery and fatigue resistance.[66]

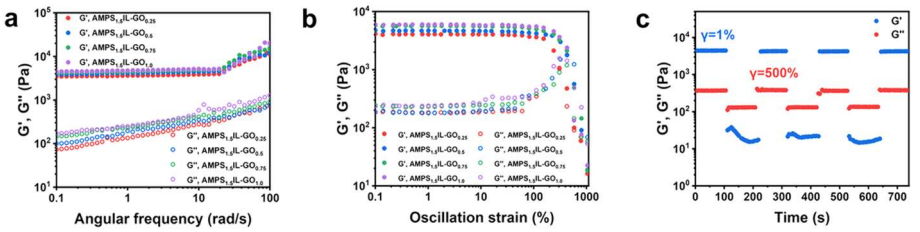

Figure 3-7. (a, b) Angular frequency sweeping and dynamic shear scanning measurements of the organohydrogels with different addition of IL-GO. (c) Cyclic step strain measurement of the $PA_{1.5}DG_{0.75}P_{1.25}$/Q organohydrogel switching between 1% and 500% strains.

Adhesive performance

Reliable adhesiveness is critical to establishing stable conformal contact for wearing comfort and sensing efficiency. The $PA_{1.5}DG_{0.75}P_{1.25}$/Q organohydrogel showed compact adhesion to various adherends (**Figure 3-8a**). As depicted in the adhesion mechanism (**Figure 3-8c**), plentiful imidazole, quaternary ammonium and sulfonic acid groups enabled the adhesion to diverse substrates through hydrogen bonds, electrostatic interactions and coordination effects. Furthermore, the adhesion strength under ambient and wet conditions was quantitatively recorded by lap-shear test (**Figure 3-8b** and **d**). The organohydrogel exhibited the highest

adhesion strength of 17.3 kPa to skin since the balance of adhesion force and cohesion force.[13] Although the adhesive strength decreased in wet environments, they were still sufficient for attachment. It should be attributed to the hydrophobic PEA fragments that penetrate the hydration film, thereby ensuring the maintenance of hydrogen bonding and electrostatic interactions induced adhesion.[67] The author also measured the adhesive behavior of the organohydrogel under 24 h treatment in harsh environment (**Figure 3-8e**). Compared to the room temperature, the adhesiveness slightly weakened after frozen yet enhanced at high temperature.

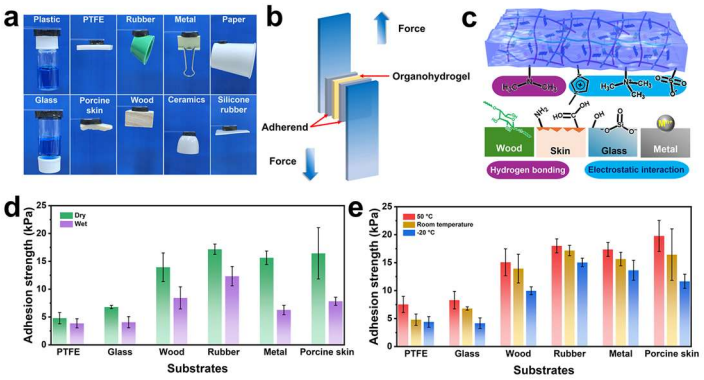

Figure 3-8. (a) Photos of the adhesion performance of the $PA_{1.5}DG_{0.75}P_{1.25}$/Q organohydrogel to different substrates, including plastic, polytetrafluoroethylene (PTFE), rubber, metal, paper, glass, porcine skin, wood, ceramics and silicone rubber.(b, c)Schematic diagrams of the lap shear test and adhesive mechanisms.(d, e) The adherence strengths of the $PA_{1.5}DG_{0.75}P_{1.25}$/Q organohydrogel toward different substrates of PTFE, glass, wood, rubber, metal and porcine skin under dry and wet condition and under room temperature, 50 °C and –20 °C treatment.

Environmental tolerance properties of the organohydrogel

To prove the environmental tolerance, differential scanning calorimetry (DSC) test was further conducted. Notably, a sharp peak in controlled hydrogel appeared at –0.46 °C, indicating the formation of ice crystals, while no crystallization peak of the organohydrogel can be observed in Figure **3-9a**. Moreover, the organohydrogel remained flexible after being bended at –20 °C and 50 °C (**Figure 3-9b**), because the crystallization and evaporation of water was suppressed via introducing DMSO. The organohydrogel

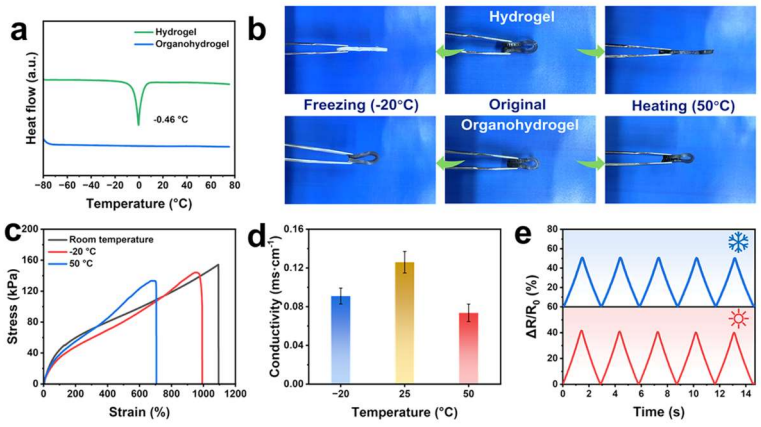

Figure 3-9. (f, g) Heat flow curves and photos and during heating process illustrating the comparison of hydrogel and organohydrogel after 24 h of treatment under extreme conditions. (h, i, j) Tensile strength, conductivity and relative resistance change of the organohydrogel strain sensor to 50% at −20 and 50 °C.

stored at high temperature exhibited a relatively lower mechanical strength compared to room temperature (**Figure 3-9c**). It can be attributed to the small amount evaporation of water and damage of some hydrogen bonding.[44] To enlarge their application scope, the electronic conductivity and sensing capability at room temperature were investigated in **Figure 3-9d** and **e**. The migration of conductor was hindered due to water loss, resulting in a declined conductivity at 50 °C.[44] The reduced conductivity at –20 °C can be attributed to the restricted mobility rate of electrons and ions.[40] However, the electrochemical signals were reproducible and steady for practical sensing applications.

Strain sensing properties

Based on the above features, the organohydrogel was expected to be exploited as an all-climate epidermal sensor (**Figure 3-10a–g**). The GF, an important index in electromechanical

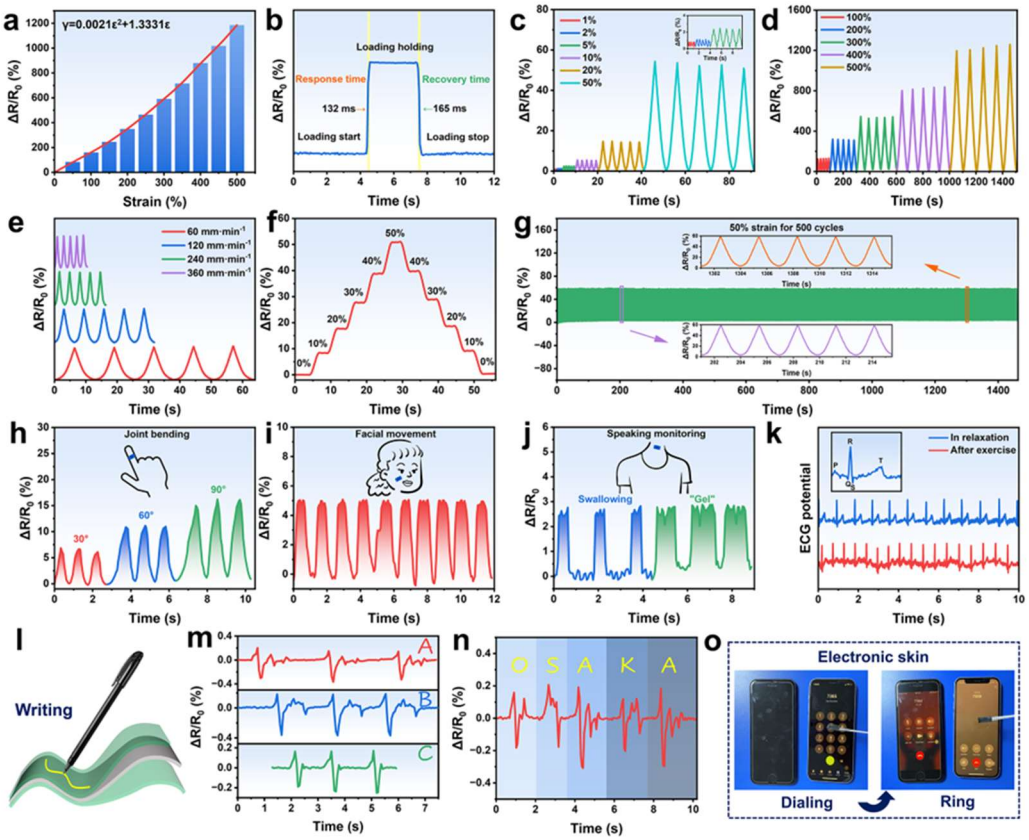

Figure 3-10. (a) Relative resistance variation with strain range of 0–500%. (b) Response and recovery time tested by loading and unloading. (c, d) Sensitivity under small strain (1%-50%) and large strain (100%–500%). (e) Sensitivity under representative stretching rates. (f) Relative resistance changes under stepwise strain. (g) Durability test (50% strain for consecutive 500 cycles) reflecting the relative resistance change. (h, i, j) Recorded relative resistance of the strain for finger bending, facial motion alongside swallowing and speaking. (k) ECG signals collected by the organohydrogel electrode. (l) Schematic diagram of the writing panel. (m, n) Resistance changes of the fabricated handwriting panel through writing representative alphabets: A, B, and C for 3 times and consecutive letters. (o) Photos showing the dialing process of the organohydrogel as an electronic skin.

sensing, was calculated to evaluate the relative change in resistance with respect to applied strain.[68] From the fitted parabolic curve, the value of GF was 1.75, 2.59 and 3.43 at strain range of 0–100%, 100–300 % and 300–500 %, respectively, revealing its favorable sensitivity. Next, the sensor performed fast response and recovery time of 132 and 165 ms, suggesting the reliable signal detection efficiency. The relative resistance changes at small strains (1~50%) and large strains (50–500%) were focused, and they both output reversible and accurate signals. Additionally, the repetitive signal changes at different stretching frequencies (50% strain) demonstrated excellent dependence towards deformation rates. The gel-based sensor showed no obvious resistance drift and maintained flexibility when subjected to different strain for a period, reflecting its good stability and repeatability. Last but not least, the author also explored its durable sensing properties under 50% strain for consecutive 500 cycles. The excellent signal stability confirmed that the sensor can meet the cyclic loadings in wearable devices. Therefore, the sensor was attached to finger, face and throat to detect representative human activity (**Figure 3-10h–j**). The relative resistance increased when the joint bending angle increased from 30° to 90°, and the values remained basically stable under same bending angle. The sensor monitored the blowing behavior precisely and showed broad prospect in conveying information via expression. The subtle physiological motion such as speaking and swallowing also be captured, benefiting from its ideal sensitivity and stability. To detect electrophysiological pressure, the gel was adhered to an electrode, and further applied in electrocardiogram (ECG) collection. **Figure 3-10k** exhibited the ECG signals before and after vigorous exercise, which provided valuable guidance for health management. In **Figure 3-10l–n**, the sensor was employed to identify signature as handwriting panel and showed significant recognition function in terms of distinctiveness, coherence and repeatability. Interestingly, the organohydrogel can be assembled into a stylus pen (**Figure 3-10o**) for dialing and drawing because of the coupling capacitor between the organohydrogel and touch screen.[30] Overall, the sensor created a fresh horizon as electronic skin in implantable devices and wearable bioelectronics.

Temperature sensing properties

The prepared organohydrogel processed excellent thermosensation owing to the thermal effect of IL-GO nanosheets. Thermal perturbations induced by temperature elevation provide

electrons with sufficient energy to undergo transitions and increase carrier concentration owing to the narrow-bandgap semiconductor characteristics of IL-GO.[25, 57] Consequently, the IL-GO based organohydrogels demonstrate excellent temperature sensing capability due to the temperature-dependent resistance changes.[57] These characteristics were investigated in the following experiment (**Figure 3-11a–f**). The temperature coefficient of resistance (TCR) is

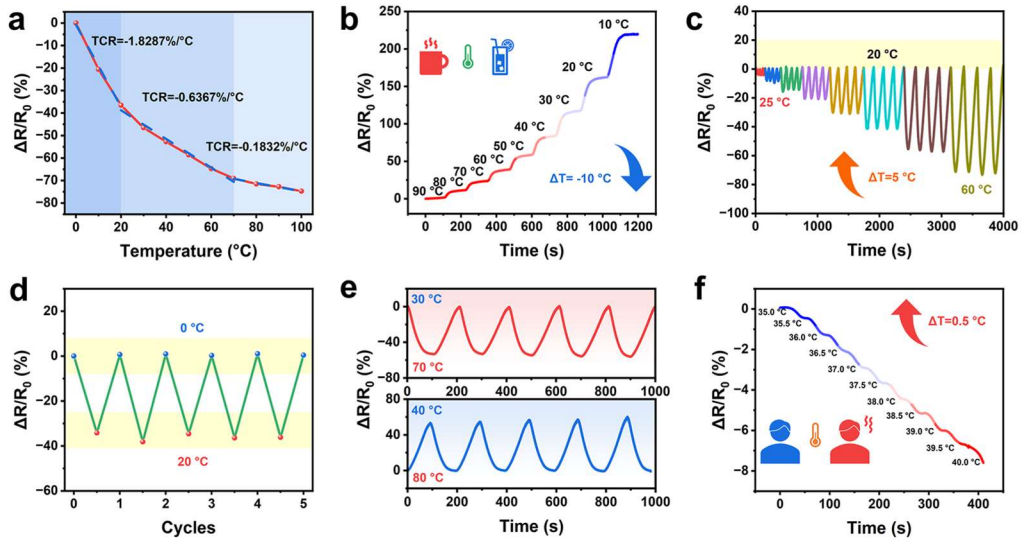

Figure 3-11. (a) Relative resistance variation of the hydrogel sensor with respect to temperature. (b) Relative resistance changes upon decreasing the temperature from 90 to 10 °C. (c) Time-relative resistance change upon cyclic heating and cooling process. (d) Reproducible temperature responsiveness from a 0 ℃ source to 20 ℃ for 5 cycles. (e) Real-time relative resistance changes recorded within consecutive heating-cooling cycles and cooling–heating cycles. (f) Real-time relative resistance variation simulating body temperature from 35 to 40 °C at a gradient of 0.5 °C.

generally used to evaluate the sensitivity of thermal response in a wide range.[36] Relative resistance decreased with the increase in temperature, thereby causing negative TCR of –1.8287% $℃^{-1}$, –0.6367% $℃^{-1}$ and –0.1832% $℃^{-1}$ in different temperature range. Specifically, the sensor not only demonstrated stable electrical signals at every 10 °C interval in the temperature range of 90~10 °C, but also displayed reproducible and wider signals during the cyclic heating-cooling process in different temperature ranges. Also, the relative resistance changes displayed stable and reproducible signal under low temperature caused dilute carrier concentration caused when repeatedly subjected to cold and hot sources. As illustrated in **Figure 3-11d**, the relative resistance exhibited distinct discrimination and negligible deviation under each temperature. It was obviously that the sensor can identify thermal signals and output real-time resistance during reversible heating-cooling processes. The organohydrogel can achieve an instantaneous electrical response to temperature changes (30–70℃ and 80–40℃),

reflecting its thermosensitive capacity and rapid recoverability (**Figure 3-11e**). Importantly, the electronic skin possessed the capability of detecting fever, as evidenced by the decreasing electrical signal with respect to the temperature from 35 to 40 °C at a gradient of 0.5 °C.

3-4. Conclusions

In conclusion, the author has designed an alkylation IL, achieved polydisperse covalent-converted graphene through nucleophilic ring-opening reaction, and innovatively expanded their function as a two-dimensional surfactant. The polymerizable IL-GO was integrated into the ultrasonic-induced organohydrogel network rather than incorporated separately. Moreover, the rapidly prepared organohydrogel exhibited favorable mechanical properties (strength of 160 kPa, elongation at break of 1090%), amphibious adhesion, moisture retention, environmental tolerance (from –20℃ to 50℃) and electrical conductivity, which enabled it applied as multimodal all-weather sensor in different scenarios. The electronic skin (GF = 3.43 at 300–500% strain) displayed reliable sensing capability for real-time monitoring human movements, recording physiological signals, handwriting recognition and applying as touch screen pen. Meanwhile, its excellent temperature perception (TCR= –1.8287% $℃^{-1}$, –0.6367% $℃^{-1}$ and –0.1832% $℃^{-1}$) enabled the detection of instantaneous temperature changes because of the superior photothermal conversion efficiency of IL-GO. This chapter provides new perspectives for developing multifunctional soft materials, inspiring the future design and fabrication for versatile electronic skin.

3-5. References

1. A. Chortos, J. Liu and Z. Bao, *Nat. Mater.*, 2016, **15**, 937-950.
2. Y. Liu, M. Pharr and G. A. Salvatore, *ACS Nano*, 2017, **11**, 9614-9635.
3. W. Wang, Y. Jiang, D. Zhong, Z. Zhang, S. Choudhury, J.-C. Lai, H. Gong, S. Niu, X. Yan, Y. Zheng, C.-C. Shih, R. Ning, Q. Lin, D. Li, Y.-H. Kim, J. Kim, Y.-X. Wang, C. Zhao, C. Xu, X. Ji, Y. Nishio, H. Lyu, J. B. H. Tok and Z. Bao, *Science*, 2023, **380**, 735-742.
4. C. Ni, D. Chen, X. Wen, B. Jin, Y. He, T. Xie and Q. Zhao, *Nat. Commun.*, 2023, **14**, 7672.
5. C.-C. Kim, H.-H. Lee, K. H. Oh and J.-Y. Sun, *Science*, 2016, **353**, 682-687.

6. F. Wang, Y. Xue, X. Chen, P. Zhang, L. Shan, Q. Duan, J. Xing, Y. Lan, B. Lu and J. Liu, *Adv. Funct. Mater.*, 2023, **34**, 2314471.

7. P. Li, Z. Jin, L. Peng, F. Zhao, D. Xiao, Y. Jin and G. Yu, *Adv. Mater.*, 2018, **30**, 1800124.

8. G. Ge, Y.-Z. Zhang, W. Zhang, W. Yuan, J. K. El-Demellawi, P. Zhang, E. Di Fabrizio, X. Dong and H. N. Alshareef, *ACS Nano*, 2021, **15**, 2698-2706.

9. J. Chong, C. Sung, K. S. Nam, T. Kang, H. Kim, H. Lee, H. Park, S. Park and J. Kang, *Nat. Commun.*, 2023, **14**, 2206.

10. F. Fu, J. Wang, H. Zeng and J. Yu, *ACS Mater. Lett.*, 2020, **2**, 1287-1301.

11. J. Chen, Q. Peng, T. Thundat and H. Zeng, *Chem. Mater.*, 2019, **31**, 4553-4563.

12. L. Han, L. Yan, K. Wang, L. Fang, H. Zhang, Y. Tang, Y. Ding, L.-T. Weng, J. Xu, J. Weng, Y. Liu, F. Ren and X. Lu, *NPG Asia Mater.*, 2017, **9**, e372-e372.

13. M. Li, H. Lu, M. Pi, H. Zhou, Y. Wang, B. Yan, W. Cui and R. Ran, *Adv. Sci.*, 2023, **10**, 2304780.

14. Y. Zhao, C.-Y. Lo, L. Ruan, C.-H. Pi, C. Kim, Y. Alsaid, I. Frenkel, R. Rico, T.-C. Tsao and X. He, *Sci. Rob.*, 2021, **6**, eabd5483.

15. L. Pan, G. Yu, D. Zhai, H. R. Lee, W. Zhao, N. Liu, H. Wang, B. C. K. Tee, Y. Shi, Y. Cui and Z. Bao, *Proc. Natl. Acad. Sci. U.S.A.*, 2012, **109**, 9287-9292.

16. H. Sun, Y. Zhao, S. Jiao, C. Wang, Y. Jia, K. Dai, G. Zheng, C. Liu, P. Wan and C. Shen, *Adv. Funct. Mater.*, 2021, **31**, 2101696.

17. T. Zhu, Y. Ni, G. M. Biesold, Y. Cheng, M. Ge, H. Li, J. Huang, Z. Lin and Y. Lai, *Chem. Soc. Rev.*, 2023, **52**, 473-509.

18. P. Song, H. Qin, H.-L. Gao, H.-P. Cong and S.-H. Yu, *Nat. Commun.*, 2018, **9**, 2786.

19. M. Pi, S. Qin, S. Wen, Z. Wang, X. Wang, M. Li, H. Lu, Q. Meng, W. Cui and R. Ran, *Adv. Funct. Mater.*, 2023, **33**, 2210188.

20. X. Liu, Q. Zhang and G. Gao, *ACS Nano*, 2020, **14**, 13709-13717.

21. H. Yang, C. Shan, F. Li, D. Han, Q. Zhang and L. Niu, *Chem. Commun.*, 2009, 3880-3882.

22. D. Li, M. B. Müller, S. Gilje, R. B. Kaner and G. G. Wallace, *Nat. Nanotechnol.*, 2008, **3**, 101-105.

23. Q. Zheng, J.-h. Lee, X. Shen, X. Chen and J.-K. Kim, *Mater. Today*, 2020, **36**, 158-179.

24. Z. Lei, B. Chen, Y.-M. Koo, D. R. MacFarlane, *Chem. Rev.*, 2017, **117**, 6633-6635.

25. M. Lan, X. Jia, R. Tian, L. Feng, D. Shao and H. Song, *Carbon*, 2024, **219**, 118850.

26. T. Xie, X. Lv, S. Tian, Y. Xie, A. Lv, Z. Lv, L. a. Jiang, Y. Zhao and S. Sun, *Macromolecules*, 2023, **56**, 6256-6266.

27. Q. Li, W. Li, Z. Liu, S. Zheng, X. Wang, J. Xiong and F. Yan, *Adv. Mater.*, 2024, **36**, 2311214.

28. I. K. Han, K.-I. Song, S.-M. Jung, Y. Jo, J. Kwon, T. Chung, S. Yoo, J. Jang, Y.-T. Kim, D. S. Hwang and Y. S. Kim, *Adv. Mater.*, 2023, **35**, 2203431.

29. T. Lalire, C. Longuet and A. Taguet, *Carbon*, 2024, **225**, 119055.

30. X. Yao, S. Zhang, L. Qian, N. Wei, V. Nica, S. Coseri and F. Han, *Adv. Funct. Mater.*, 2022, **32**, 2204565.

31. S. Gong, Y. Lu, J. Yin, A. Levin and W. Cheng, *Chem. Rev.*, 2024, **124**, 455-553.

32. X. Wang and P. Wu, *ACS Appl. Mater. Interfaces*, 2019, **11**, 21946-21954.

33. H. Liao, X. Guo, P. Wan and G. Yu, *Adv. Funct. Mater.*, 2019, **29**, 1904507.

34. Z. Li, J. Li, J. Cui, H. Qiu, G. Yang, S. Zheng and J. Yang, *J. Mater. Chem. A*, 2019, **7**, 17937-17946.

35. H. Zhang, K. Xue, C. Shao, S. Hao and J. Yang, *Chem. Mater.*, 2023, **35**, 10316-10347.

36. Y. Liu, G. Tian, Y. Du, P. Shi, N. Li, Y. Li, Z. Qin, T. Jiao and X. He, *Adv. Funct. Mater.*, 2024, 2315813, DOI: 10.1002/adfm.202315813.

37. S. Wu, T.-W. Wang, Y. Du, B. Yao, S. Duan, Y. Yan, M. Hua, Y. Alsaid, X. Zhu and X. He, *NPG Asia Mater.*, 2022, **14**, 65.

38. X. Huang, Z. Zheng, H. Wang, W. Xu, M. Wu, M. Wang, C. Chen, L. Wan, R. Du, T. Zhu, Z. Huang, X. Wang, X. Wang, Q. Zhang and X. Jia, *Adv. Funct. Mater.*, 2024, **34**, 2312149.

39. P. Du, J. Wang, Y.-I. Hsu and H. Uyama, *Chem. Mater.*, 2024, **36**, 1318-1332.

40. J. Liu, X. Zhang, Y. Cui, Y. Liu, W. Wang, Y. Guo, Q. Wang and X. Dong, *ACS Appl. Mater. Interfaces*, 2024, **16**, 5208-5216.

41. C. Wang, B. Yang, R. Xiang, J. Ji, Y. Wu and S. Tan, *ACS Nano*, 2023, **17**, 23194-23206.

42. R. Liu, Y. Liu, S. Fu, Y. Cheng, K. Jin, J. Ma, Y. Wan and Y. Tian, *Small*, 2024, **20**,

2308092.

43. B. Song, X. Dai, X. Fan and H. Gu, *J. Mater. Sci. Technol.*, 2024, **181**, 91-103.

44. Z. Shang, G. Liu, Y. Sun, C. Li, N. Zhao, Z. Chen, R. Guo, Z. Zheng, F. Zhou and W. Liu, *ACS Appl. Mater. Interfaces*, 2023, **15**, 44342-44353.

45. J. Wu, W. Huang, Z. Wu, X. Yang, A. G. P. Kottapalli, X. Xie, Y. Zhou and K. Tao, *ACS Mater. Lett.*, 2022, **4**, 1616-1629.

46. S. Chen, C. Peng, D. Xue, L. Ma and C. Zhi, *Angew. Chem. Int. Ed.*, 2022, **61**, e202212767.

47. M. A. Kuzina, D. D. Kartsev, A. V. Stratonovich and P. A. Levkin, *Adv. Funct. Mater.*, 2023, **33**, 2301421.

48. H. Fan, J. Wang and J. P. Gong, *Adv. Funct. Mater.*, 2021, **31**, 2009334.

49. Y. Wang, J. Ma, X. Ye, W. Wong, C. Li and K. Wu, *Electrochim. Acta*, 2018, **271**, 551-559.

50. S. Wang, L. Wang, X. Qu, B. Lei, Y. Zhao, Q. Wang, W. Wang, J. Shao and X. Dong, *ACS Appl. Mater. Interfaces*, 2022, **14**, 50256-50265.

51. Z. Wang, J. Chen, Y. Cong, H. Zhang, T. Xu, L. Nie and J. Fu, *Chem. Mater.*, 2018, **30**, 8062-8069.

52. T. L. Sun, F. Luo, W. Hong, K. Cui, Y. Huang, H. J. Zhang, D. R. King, T. Kurokawa, T. Nakajima and J. P. Gong, *Macromolecules*, 2017, **50**, 2923-2931.

53. S. Tian, Y. Xing, Y. Long, H. Guo, S. Xu, Y. Ma, C. Wen, Q. Li, X. Liu, L. Zhang and J. Yang, *ACS Appl. Mater. Interfaces*, 2022, **14**, 5122-5133.

54. Y. Ma, Y. Gao, L. Liu, X. Ren and G. Gao, *Chem. Mater.*, 2020, **32**, 8938-8946.

55. R. Zhao, Z. Zhao, S. Song and Y. Wang, *ACS Appl. Mater. Interfaces*, 2023, **15**, 59854-59865.

56. Y. Wu, L. Yang, J. Wang, S. Li, X. Zhang, D. Chen, Y. Ma and W. Yang, *ACS Appl. Mater. Interfaces*, 2023, **15**, 36759-36770.

57. G. Ge, Y. Lu, X. Qu, W. Zhao, Y. Ren, W. Wang, Q. Wang, W. Huang and X. Dong, *ACS Nano*, 2020, **14**, 218-228.

58. X. Yu, G. Bakan, H. Guo, M. S. Ergoktas, P. Steiner and C. Kocabas, *ACS Nano*, 2023,

17, 11583-11592.

59. H. Sun, B. Tang and P. Wu, *ACS Appl. Mater. Interfaces*, 2017, **9**, 26077-26087.

60. A. C. Ferrari, F. Bonaccorso, V. Fal'ko, K. S. Novoselov, S. Roche, P. Bøggild, S. Borini, F. H. L. Koppens, V. Palermo, N. Pugno, J. A. Garrido, R. Sordan, A. Bianco, L. Ballerini, M. Prato, E. Lidorikis, J. Kivioja, C. Marinelli, T. Ryhänen, A. Morpurgo, J. N. Coleman, V. Nicolosi, L. Colombo, A. Fert, M. Garcia-Hernandez, A. Bachtold, G. F. Schneider, F. Guinea, C. Dekker, M. Barbone, Z. Sun, C. Galiotis, A. N. Grigorenko, G. Konstantatos, A. Kis, M. Katsnelson, L. Vandersypen, A. Loiseau, V. Morandi, D. Neumaier, E. Treossi, V. Pellegrini, M. Polini, A. Tredicucci, G. M. Williams, B. Hee Hong, J.-H. Ahn, J. Min Kim, H. Zirath, B. J. van Wees, H. van der Zant, L. Occhipinti, A. Di Matteo, I. A. Kinloch, T. Seyller, E. Quesnel, X. Feng, K. Teo, N. Rupesinghe, P. Hakonen, S. R. T. Neil, Q. Tannock, T. Löfwander and J. Kinaret, *Nanoscale*, 2015, **7**, 4598-4810.

61. J. Wang, P. Du, Y.-I. Hsu and H. Uyama, *ACS Sustainable Chem. Eng.*, 2023, **11**, 10061-10073.

62. Z. Ma, C. Bourquard, Q. Gao, S. Jiang, T. De Iure-Grimmel, R. Huo, X. Li, Z. He, Z. Yang, G. Yang, Y. Wang, E. Lam, Z.-h. Gao, O. Supponen and J. Li, *Science*, 2022, **377**, 751-755.

63. P. Du, J. Wang, Y.-I. Hsu and H. Uyama, *ACS Appl. Mater. Interfaces*, 2023, **15**, 23711-23724.

64. H. Li, P. Tan, Y. Rao, S. Bhattacharya, Z. Wang, S. Kim, S. Gangopadhyay, H. Shi, M. Jankovic, H. Huh, Z. Li, P. Maharjan, J. Wells, H. Jeong, Y. Jia and N. Lu, *Chem. Rev.*, 2024, **124**, 3220-3283.

65. P. Ying, A. Natan, O. Hod and M. Urbakh, *ACS Nano*, 2024, **18**, 10133-10141.

66. J. Wang, P. Du, Y.-I. Hsu and H. Uyama, *Chem. Eng. J.*, 2024, **480**, 148324.

67. S. He, B. Guo, X. Sun, M. Shi, H. Zhang, F. Yao, H. Sun and J. Li, *ACS Appl. Mater. Interfaces*, 2022, **14**, 45869-45879.

68. J. Xiong, X. Wang, L. Li, Q. Li, S. Zheng, Z. Liu, W. Li and F. Yan, *Angew. Chem. Int. Ed.*, 2024, **63**, e202316375.

Concluding remarks

In this doctoral thesis, a series of conductive hydrogel materials based on chitosan and synthetic polymer structures were designed and prepared. Here, chitosan as the reinforcing phase effectively enhanced the mechanical strength and toughness of the multifunctional hydrogels, while different conductive mechanisms endowed the hydrogels with favorable electromechanical response. Therefore, its application as flexible sensors were investigated in detail, which provided new prospects for the development of hydrogel-based wearable electronic devices.

In chapter 1, a hydrogel composed of a rigid matrix and flexible polyacrylamide network was fabricated. The hydrophobic and aggregated polyaniline was homogeneously embedded on chitosan backbone, thereby improving their processability and matrix matching. Simultaneously, the quaternate-functionalized nucleobase moieties endowed the hydrogel with self-adhesiveness, which ensured significant interface interactions and avoided the deterioration of mechanical and electrochemical performance. Therefore, the resulting hydrogel exhibited a promising conductivity attributed to the uniformly dispersed polyaniline components and a high strain strength because of the chain entanglement of chitosan after soaking in Na_3Cit solution. In addition, the modified adenine molecules not only realized synchronization in improving the toughness and exhibiting a skin-like elastic modulus, but also provided a durable interfacial contact with various materials. Lastly, the hydrogel can be further fabricated into a strain-monitoring sensor for information encryption and sign language transmission based on its sensing stability and strain sensitivity and fast responsibility.

In chapter 2, considering the limitations of underwater application in the first chapter, the author proposed a multiple dynamic-bond-driven hydrophobic association hydrogel with reliable water resistance, mechanical robustness, and stable electrical property via a “two-step” method including micellar copolymerization and postsoaking strategy. Benefiting from the electrostatic interacted hydrophobic segments formed by MMA in the presence of CTAB micelles, the hydrogel exhibited desirable low-swelling feature, excellent stretchability, and

toughness. The synergistic mechanisms of hydrophobic association and ultrasound dispersion endow the hydrogel with repeatable wet-adhesion capability. Moreover, the hydrogel possesses significant conductivity and storage durability owing to the chitosan chain entanglements, electrostatic interactions, and strong hydrogen bonding established by PANa. As a demonstration, a flexible sensor is fabricated to transmit various human movement signals and monitor electrocardiography in amphibious environments based on its wide sensing range and linear sensitivity.

In chapter 3, to further expand the application scenarios of hydrogels sensors, an all-weather organohydrogel based on carbon nanomaterials conducting mechanism was fabricated, which exhibited superior structural compatibility, enhanced signal accuracy, and favorable resilience under harsh environments. To address the issues of additive agglomeration and phase separation within the polymer matrix, assembly of amphiphilic nanosheets at oil/water interfaces for co-stabilization is innovatively proposed. The critically dispersed graphene nanosheets, assisted by IL graft-exfoliation, can be chemically integrated into swelling-resistant polymeric networks through ultrasonic-induced gelation. Additionally, the synergistic effect between DMSO/H_2O binary solvent and charged polar terminal groups weakened the hydrogen bonding within water molecules, enabling the organohydrogel with reliable environmental tolerance and long-lasting moisture retention. Owing to its high mechanical stretchability, satisfactory sensitivity, and exceptional photothermal conversion behavior, the rapidly prepared organohydrogel was fabricated as flexible sensor for daily activities detection and temperature sensing.

In summary, the author attempted different conductive strategies to functionalize chitosan containing hydrogels through the synergistic effect of chemical crosslinking and physical crosslinking. The mechanical performance and recovery properties of the gel systems were significantly improved through the stabilizing effect between chitosan and the flexible polymer molecular chains. In addition, the intrinsic mechanisms behind the enhanced toughness and conductivity of the self-adhesive hydrogels were clarified in relation to the compatibility and balance between conductive components and the polymer network. Lastly, the high-strength and environmentally tolerant hydrogel materials achieved application in flexible sensors. The

author believes that the material design and development will inspire the construction of functional soft materials for wearable electronic systems in complex scenarios.

List of Publications

1. Bio-Inspired Homogeneous Conductive Hydrogel with Flexibility and Adhesiveness for Information Transmission and Sign Language Recognition

Peng Du, Juan Wang, Yu-I Hsu* and Hiroshi Uyama*

ACS Applied Materials & Interfaces, 2023, 15, 23711-23724.

DOI: 10.1021/acsami.3c02105.

2. Hydrophobic Association Hydrogel Enabled by Multiple Noncovalent Interactions for Wearable Bioelectronics in Amphibious Environments

Peng Du, Juan Wang, Yu-I Hsu*, and Hiroshi Uyama*

Chemistry of Materials, 2024, 36, 1318-1332.

DOI: 10.1021/acs.chemmater.3c02454.

3. Homogenous Organohydrogel Mediated by Covalently-Converted Graphene Nanosheets as an Electronic Epidermis for Multimodal Perception and Soft Actuation

Peng Du, Juan Wang, Yu-I Hsu*, and Hiroshi Uyama*

ACS Materials Letters, 2024, 6, 2974-2984.

DOI: 10.1021/acsmaterialslett.4c00809.

Acknowledgments

The work described in this thesis was carried out at Polymer Materials Chemistry Area, Division of Applied Chemistry, Graduate School of Engineering, Osaka University, from 2022 to 2024. Finishing this dissertation marks a major milestone in my academic career, one that I could not have reached without the support and guidance of many individuals.

At the outset, I would like to extend my sincere thanks to my parents for their endless support and love. The warmest encouragement from my family motivates me to persist in my studies. Then, I would like to extend my sincere thanks to the members of my dissertation committee, Prof. Akinori Saeki and Prof. Takashi Hayashi, for their valuable suggestions and constructive comments, as well as the time they dedicated to reviewing this dissertation, which have greatly enhanced the quality of this work. Additionally, I sincerely thank the professors of the Materials Chemistry Course, Department of Applied Chemistry, Osaka University for their valuable time in attending my doctoral dissertation defense and for providing many useful suggestions. I will also express my thanks to Prof. Susumu, Kuwabata and Assoc. Prof. Taro Uematsu for their guidance in the “Research Proposal Seminar” class. During this study abroad, I would like to convey my profound gratitude to Prof. Hiroshi Uyama. I am also very grateful to Assoc. Prof. Yu-I Hsu for her support and assistance of my research experiments. Besides, I will express my greatest thanks to all of the past and present fellow members in Uyama Lab: Prof. Dr. Jinjun Yang, Mr. Motoi Oda, Mr. Koki Tsujita, Mr. Sota Nakagawa, Mr. Atsuki Takagi, Mr. Hiroshi Hasegawa, Mr. Shunya Kubo, Mr. Yi-Ho Chen, Mr. Ruiqi Zhang, Mr. Yihan Gao, Mr. Xinyu Lou, Ms. Yoko Uenishi, Ms. Tomoko Shimizu, Ms. Chikako Abe, Ms. Akane Odagaki, Ms. Erina Katsuragawa, Ms. Juan Wang, Ms. Izzah Durrati Binti Haji Abdul Hamid, Ms. Sooyeon Noh and Ms. Shafinee Yarnina *etc.* for their kind-hearted help, both in my research and daily life.

Lastly, I am also grateful for the scholarship grant of the Ministry of Education, Culture, Sports, Science and Technology (MEXT), Japan.

June 2024

Peng Du